Technische Universität München

TUM School of Computation, Information and Technology

Analysis of Neural Devices for Small-Nerve Interfacing

Francisco Luis Zurita

Vollständiger Abdruck der von der TUM School of Computation, Information and Technology der Technischen Universität München zur Erlangung des akademischen Grades eines **Doktors der Ingenieurwissenschaften** genehmigten Dissertation.

Vorsitz: Prof. Dr. Alessio Gagliardi

Prüfer der Dissertation:

1. Prof. Dr. Bernhard Wolfrum
2. Prof. Dr. Eric Daniel Głowacki

Die Dissertation wurde am 24.07.2023 bei der Technischen Universität München eingereicht und durch die TUM School of Computation, Information and Technology am 18.01.2024 angenommen.

Kurzfassung

Die Verbindung von peripheren Nerven mit externen Elektroden ist eine wichtige Technik (PNI nach ihrer Abkürzung in Englisch), um diese Nerven zu stimulieren oder ihre neuronale Aktivität aufzuzeichnen. Die PNI-Technik kann zur Diagnose und Behandlung von Krankheiten eingesetzt werden, wenn andere Methoden unzureichend oder nicht vorhanden sind. Außerdem bietet die PNI Potenzial für die Entwicklung von Neuroprothesen, d.h. Prothesen, die direkt mit dem Nervensystem verbunden sind und idealerweise vom Gehirn gesteuert werden oder auch verlorene Empfindungen wiederherstellen können.

Im Allgemeinen ist die PNI-Technik mit einem Zielkonflikt zwischen der Selektivität der Ansteuerung und der daraus resultierenden Invasivität konfrontiert. So ermöglicht beispielsweise die Implantation einer Elektrode in die Nähe des Nervs die gezieltere Ansteuerung eines Axons innerhalb des Nervenbündels, gleichzeitig erhöht sich jedoch auch die Schwere des Eingriffs. Extraneurale Elektroden werden zu den am wenigsten invasiven Nervenelektroden gezählt, da sie den Nerv von außen ansprechen, ohne seine Schichten zu durchdringen. Diese Eigenschaft macht sie jedoch weniger selektiv als intraneurale Elektroden. Die Selektivität von extraneuralen Elektroden kann erhöht werden, indem kleinere Nerven angesteuert werden, da diese weniger Axone umfassen.

In der vorliegenden Arbeit werden neuartige extraneurale Schnittstellen für kleine Nerven charakterisiert und anschließend miteinander verglichen. Zunächst wurde ein

Protokoll für in vivo Experimente entwickelt. Hierfür wurde das Insekt *Locusta migratoria* aufgrund seiner einfachen neuronalen Anatomie als Tiermodell ausgewählt. Insbesondere weist dieses Tier ein Axon auf, das bei Stimulation eine plötzliche tibiofemorale Streckbewegung hervorruft, welche im Folgenden als Biomarker für die Stimulationsprotokolle verwendet wurde. Messaufbaus wurde ein geschlossener Regelkreis mit einer selbst entwickelten Manschettenelektrode implementiert, der es erlaubt, den tibiofemoralen Durschnittswinkel des Insekts durch externe Stimulation zu steuern.

Des Weiteren wurden moderne additive Fertigungsmethoden verwendet, um eine neuartige, vollständig in 3D gedruckte Manschettenelektrode herzustellen, die Zwei-Photonen-Stereolithographie und 3D-Tintenstrahldruck kombiniert. Das entwickelte Implantat hat ein kleines Aspektverhältnis und sein praktisches Design erleichtert die Kopplung mit dem Nerv. Es verfügt außerdem über vier Elektroden, die nicht nur zur selektiven Stimulation des Nervs, sondern auch zur Aufzeichnung von Signalen und zur Bestimmung ihrer Ausbreitungsrichtung entlang des Nervs verwendet werden können.

Schließlich werden weitere Materialen und Ansätze zur Herstellung von Manschettenelektroden vorgestellt. Diese Implantat-Prototypen verbessern wichtige Eigenschaften extraneuraler Manschettenelektroden, wie z. B. Elektrodenanzahl und einfachere Nervenbefestigungsmechanismen.

Abstract

Peripheral nerve interfacing (PNI) is an important technique in which nerves are interfaced externally with an electrode to stimulate the nerve or record its neural activity. PNI can be used to diagnose and treat diseases where other methods are insufficient or do not exist. Furthermore, it has potential in the development of neuroprostheses, that is, prostheses that interface directly with the nervous system and could, ideally, be commanded by brain signals and used to restore lost sensations.

PNI poses an inherent tradeoff between the selectivity of communication with a specific axon within a nerve and the invasiveness of bringing an electrode in proximity to that axon. Extraneural electrodes are counted within the least invasive nerve electrodes because they interface the nerve from the outside without piercing through its layers. However, this characteristic makes them less selective than intraneural electrodes. Interfacing small nerves that comprise fewer axons can be used to increase the selectivity of extraneural electrodes. In this work, I characterize and compare novel extraneural interfaces for small nerves.

First, I develop an in vivo framework to work with small nerves. I select the insect *Locusta migratoria* as the animal model because of its simple neural anatomy. In particular, this animal presents an axon that elicits a sudden tibiofemoral extension movement when stimulated. I use this movement as a biomarker for stimulation protocols. To validate this framework, I implement a closed-loop system

featuring a self-developed cuff electrode that controls the mean tibiofemoral angle of the subject.

Next, I combine modern additive manufacturing techniques to fabricate a novel, fully 3D-printed cuff electrode, combining two-photon stereolithography and 3D inkjet printing. The developed device has a small aspect ratio and its convenient design facilitates the interfacing procedure. This device also features four electrodes which were not only used to selectively stimulate the nerve, but also to record signals and determine their direction of propagation along the nerve.

Finally, I characterize other cuff electrodes showcasing novel materials and fabrication methods. These devices improve important characteristics of extraneural cuff electrodes, such as electrode count and more straightforward nerve attachment mechanisms.

Contents

1 Introduction **1**

2 Fundamentals **7**

2.1 Nervous system and peripheral nerve interfacing (PNI) 7

2.1.1 Nerve anatomy and physiology 7

Extraneural interfacing 13

2.1.2 Peripheral nerve interfaces 16

Intraneural PNI 17

Extraneural PNI 19

2.2 Electrochemical characterization 20

2.2.1 The electrode-electrolyte interface 20

2.2.2 Electrochemical methods 24

Cyclic voltammetry 26

Voltage transients 29

Electrochemical impedance spectroscopy 31

2.3 Animal model: *Locusta migratoria* 33

2.3.1 Anatomy 34

2.3.2 Nervous system 36

3 Initial steps: rapid prototyping of a small nerve cuff 41

3.1 Preamble 41

3.2 Introduction 42

3.3 Materials and methods 45

3.3.1 Control loop design 45

3.3.2 Electrode fabrication 46

3.3.3 Electrochemical characterization of the electrodes 49

3.3.4 Surgery and nerve interfacing 49

3.4 Results and discussion 51

3.4.1 Electrode characterization 51

3.4.2 Control strategy 52

3.5 Conclusions 56

4 3D-printed nerve cuffs 57

4.1 Preamble 57

4.2 Introduction 58

4.3 Materials and methods 62

4.3.1 Inkjet-printed 3D microelectrode arrays 62

4.3.2 Printing the passivation 63

4.3.3 Two-photon stereolithographic cuff printing and laser cutting 63

4.3.4 Electrochemical characterization of cuff sensors 64

4.3.5 Nerve interfacing 65

4.4 Results and discussion 67
4.4.1 Electrochemical characterization of the electrodes 68
4.4.2 Stimulation results 70
4.4.3 Simulation of activating function 72
4.4.4 Recording of neural activity 74
4.5 Conclusions 79

5 Further approaches to improve small nerve interfacing 81

5.1 Preamble 82
5.2 Introduction 82
5.3 Materials and methods 84
5.3.1 Self-folding cuff electrodes 85
Electrochemical characterization 85
In vivo experiments 85
5.3.2 Pre-folded cuff electrodes 87
Mechanical characterization 87
Electrochemical characterization 87
In vivo experiments 88
5.4 Results and discussion 89
5.4.1 Self-folding cuff electrodes 89
Electrochemical characterization 89
In vivo validation 92
5.4.2 Pre-folded cuff electrodes 96
Electrode fabrication 96

Mechanical characterization 96

Electrochemical characterization 98

Implantation procedure and interfacing 100

Post-implantation analysis 101

5.5 Conclusions 104

6 Conclusions and outlook 105

6.1 Recording and stimulation 106

6.2 Selectivity and invasiveness 107

6.3 Robustness and ease of implantation 109

6.4 Comparison of the different devices 110

Bibliography 113

Appendix 163

A *Locusta migratoria* surgical procedure 163

A.1 Procedure 163

B Control circuit 165

C Schematic of the cuff molds 167

C.1 Top mold 168

C.2 Bottom mold 169

D Evolution of the final design of the 3D-printed cuff electrodes 171

E Locust leg movement **173**

F Finite element method simulations **177**

G Comparative recordings with Ag hook electrodes **179**

Publications **181**

CHAPTER 1

Introduction

Figure 1.1: Concept art of neural tissue interfacing an electronic circuit. This image was created with the assistance of `craiyon.com`.

Interfacing with the nervous system to restore lost functions or surpass the limits of the human body is a concept that has been influencing our culture for many years. The seamless replacement of a severed hand, for example, with an equally functional robotic prosthesis is perhaps best portrayed in the impactful scene featuring Luke

Skywalker in Star Wars. Subsequent art productions proposed even more ambitious scenarios in which neural interfacing plays a central role, such as Neuromancer (1984), Ghost in the Shell (1989), and the iconic The Matrix (1999). Whereas the current state of the art is still far from these scenarios, it is a fact that the last years have not only seen a significant increase in the number of scientific articles dealing with neurotechnologies [1], but also in the financial investment in the neurotechnology industry [2]. The renewed interest in neural interfacing has also been accompanied by an exponential increase in the number of companies and start-ups aiming to bridge the gap between brain and machine. Some of them, like Elon Musk's Neuralink, have even drawn significant media attention. Despite the variety of research and industrial approaches, their overarching goals remain the same: increasing the fundamental knowledge about the nervous system to treat its disorders and expanding its reach beyond the natural limits.

Neural interfacing can target the central (CNS) and the peripheral nervous system (PNS). The PNS is composed of the nerves and ganglia outside the brain and spinal cord and acts as the messaging system of our body. It connects the brain to the sensory organs and the muscles, allowing us to perceive and interact with the physical world. Furthermore, the PNS also regulates autonomous body functions that are indispensable for life, such as heart beating and breathing. Since the nerves that make up the PNS carry high-density information pertaining to our body, there is an increasing interest to interface them for therapeutic purposes, such as diagnosing diseases in earlier stages or restoring lost sensations.

The use of electricity to treat ailments such as chronic pain has been known for a long time and can be traced back to ancient times [3]. However, the concept of externally interfacing with the PNS as we know it dates to the famous experiment of Luigi Galvani in 1787. In his work, he contracted the legs of a frog by applying electricity to their innervating nerves. However, it was not until the 1960s that peripheral nerve interfaces were first clinically implemented [4, 5]. The promising results of the first experiences paved the way for further research and development of neuromodulation strategies. In particular, the importance of the vagus nerve was well known since the 1800s and represented an attractive target for therapeutic interfacing [6]. In 1985, vagus nerve stimulation (VNS) was shown to successfully reduce seizures in epileptic patients [7]. Today, VNS is an approved clinical treatment for epilepsy [8] and depression [9]. Moreover, its potential to treat other conditions, such as cardiovascular disease [10], obesity [11], rheumatoid arthritis [12], and even respiratory symptoms associated with COVID-19 [13] is being investigated.

The development of peripheral nerve interfaces is an active field of research, today more than ever [14]. The two major challenges for nerve interfacing are achieving high selectivity and stable long-term performance [15]. Since nerves comprise multiple axons, selective stimulation is an important requirement to mainly elicit the desired response while minimizing side effects. Higher selectivity has traditionally been achieved by placing the electrode closer to the desired nerve fibers. However, this method requires electrodes that penetrate the tissues surrounding these fibers, generating trauma. Placing the electrodes on the outside of the nerve generates less trauma but the selectivity is reduced. Therefore, a compromise between selectivity and invasiveness is always made in the design of nerve interfaces. Irrespective of the level of invasiveness, an implant is always regarded as an alien body by the organism and will trigger a foreign body response [16]. The immune system will attack the electrode, consequently degrading its performance. It has been shown that the long-term performance of devices that interface the nerve from its surface (extraneural) is better than that of those that pierce the nerve (intraneural) [17, 18]. There have been attempts to increase the selectivity of extraneural interfaces, such as nerve-reshaping devices [19, 20], increasing the number of electrodes [21–24], and using modern signal processing techniques to improve recording selectivity [25].

Commonly targeted nerves for research and clinical applications tend to be large, usually around 1 mm in diameter [26]. Stimulating large nerves carries the risk of undesired neuromodulatory responses because they comprise multiple nerve fibers. Furthermore, recording from a nerve with multiple fibers presents challenges to the task of determining the sources of the signals. One way to increase selectivity is to interface with smaller nerves, as they comprise fewer axons. In recent years, researchers have leveraged advances in fabrication techniques and materials science to develop small and flexible interfaces to overcome challenges associated with small peripheral nerve interfaces [27–31]. Whereas intense research is being carried out to improve nerve interfacing from many fields, a gold standard for long-term small nerve interfacing is yet to be achieved.

The present work investigates different approaches of interfacing small nerves extraneurally. I will focus on the comparison of different electrodes in terms of the materials used, fabrication and stimulation and recording performance. I will further investigate their long-term behavior in insects. Finally, I will assess the possibilities of closing the interfacing loop in real time. The rest of the thesis is organized as follows. **Chapter 2** introduces the fundamentals of neuroanatomy, electrophysiology, electrochemistry, and state-of-the-art peripheral neural interfaces. **Chapter 3** presents a silicone cuff electrode for small nerve interfacing used in a closed-loop circuit in vivo and in real time. **Chapter 4** describes the design and implementation of a cuff electrode for small nerves fabricated using a combination of 3D printing techniques. Its selectivity in terms of both stimulation and recording is further characterized. **Chapter 5** shows the implementation and comparison of smart electrodes. Finally, **Chapter 6** compares and discusses the used electrodes.

CHAPTER 2

Fundamentals

In this chapter, I present the theoretical background of the topics discussed in this thesis, along with a brief review of nerve interfaces and a description of the animal model employed. It is worth noting that the fundamental information provided here can also be found in standard textbooks.

2.1 Nervous system and peripheral nerve interfacing (PNI)

2.1.1 Nerve anatomy and physiology

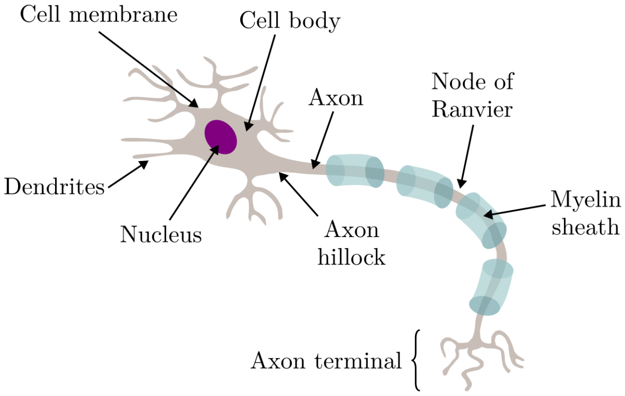
Cell membrane
Cell body
Axon
Node of Ranvier
Dendrites
Myelin sheath
Nucleus
Axon hillock
Axon terminal

Figure 2.1: A schematic of a typical mammalian neuron depicting its constituent parts.

The neuron is the basic unit of the nervous system. It is an excitable cell with a negative voltage difference across its membrane at rest with respect to the extracellular space. The neuron has three main parts: the soma, the dendrites and the axon (Figure 2.1). The soma hosts the nucleus and all the organelles required for the correct functioning of the cell. The dendrites are projections of the cell that receive input from other neurons and relay it to the soma. The axon is the only output projection of the neuron and it carries the signals to the dendrites of other neurons or to the end organ. Myelin is a fatty substance that surrounds and insulates the axon, preventing electrical signals from dissipating and increasing the speed at which they can travel. The myelin sheath is made up of specialized glial cells, oligodendrocytes in the central nervous system and Schwann cells in the peripheral nervous system. The myelin sheaths are separated by nodes of Ranvier, which are small gaps that allow the electrical signal to be regenerated. In this way, it is ensured that the signals remain strong as they travel along the axon [32].

The nerves of the peripheral nervous system can be thought of as a bundle of axons organized as a series of nested layers. The outermost layer is the *epineurium*, which is a layer of connective tissue that surrounds the entire nerve. Within the epineurium, individual axons are organized into smaller groups called *fascicles*. These fascicles are separated by loose connective tissue and are held together by another layer of connective tissue called the *perineurium*. The perineurium helps to protect and maintain the structure of the nerve fibers within each fascicle. Individual axons are surrounded by their own layer of supportive cells called *endoneurium*. The arrangement of these layers helps to protect and maintain the structural and functional integrity of the nerve. Nerves also carry blood vessels to supply their ample energy demand [33, 34].

Neurons keep a potential difference of around $-70\,\mathrm{mV}$ with respect to the extracellular medium at rest (the extracellular potential is conventionally set to $0\,\mathrm{V}$). The cell membrane is a lipid bilayer with some proteins embedded into it. Some of these proteins maintain a concentration difference for the ions between the extra- and intracellular media and are called *ion pumps*. It is the different concentration of ions on each side of the membrane that gives origin to the membrane (or transmembrane) voltage V_m. Other proteins called *ion channels* permit the selective diffusion of certain ion species across the membrane, Na^+ and K^+ amongst the most important.

The unit of signaling of the neurons is the *action potential*, usually also called *spike* because of its shape, and it is an essential component of the mechanism by which neurons communicate with one another and with other cells. It is a rapid and brief (~$1\,\mathrm{ms}$) change in V_m, as shown in Figure 2.2. Normally, it is generated in the axon hillock and travels down the axon until the axon terminals. The action potential is initiated when the membrane potential of a neuron becomes depolarized beyond a threshold potential, meaning that the voltage difference between the inside and outside of the cell becomes less negative. This event triggers the opening of Na^+ and K^+ voltage-gated ion channels. Initially, an influx of Na^+ enters the cell driven by both its concentration and electrical gradients, which causes a sharp increase in the intracellular voltage. This influx further depolarizes the membrane and triggers

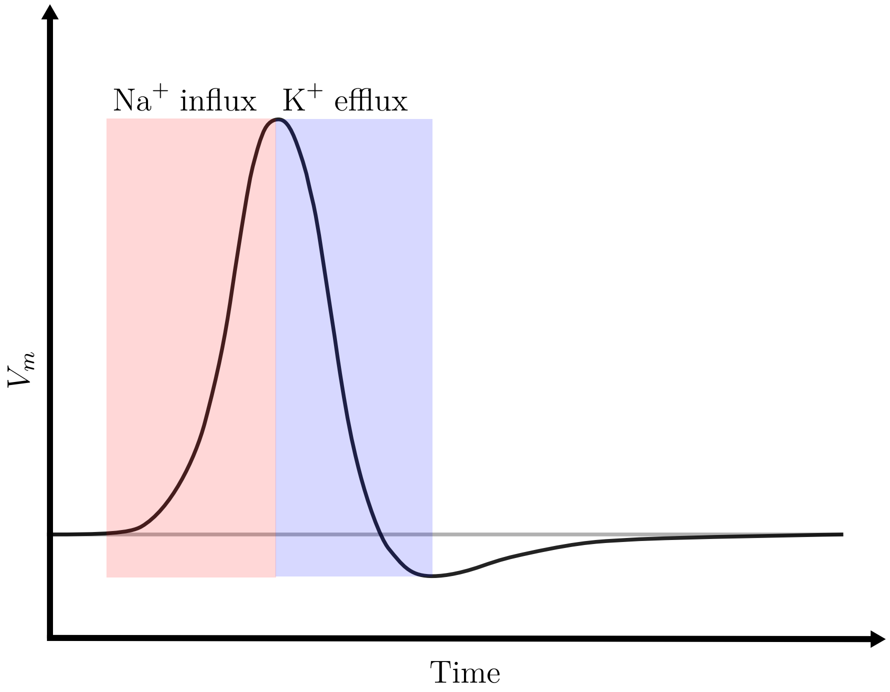

Figure 2.2: Typical shape of an action potential. The rising edge is due to the sudden influx of Na^+ into the cell. The repolarization is due to the inactivation of the Na^+ ion channels and the efflux of K^+.

the opening of more ion channels, creating a chain reaction that results in a rapid, all-or-nothing increase in the membrane potential. After the initial influx, the Na^+ channels inactivate and the K^+ channels continue to open slowly. With no more Na^+ influx and an efflux of K^+ driven by its concentration and electrical gradients, V_m decreases until a value below the resting membrane voltage. This low value of V_m causes the closing of the K^+ ion channels and the de-inactivation of the Na^+ channels, resetting the membrane potential to its value at rest. The period immediately after the action potential is characterized by the difficulty or impossibility of generation of another action potential due to the inactivation of the Na^+ channels and it is known as the refractory period. Once the action potential reaches the axon terminal, it triggers the release of neurotransmitters, which bind to receptors on the next neuron and initiate a new action potential. This process continues along the chain of neurons until the message reaches its final destination [32, 35].

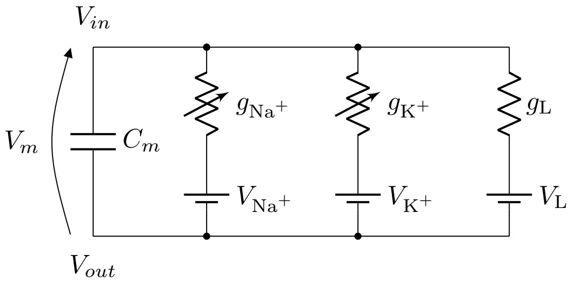

Figure 2.3: Hodgkin-Huxley electrical model of the cell membrane.

Hodgkin and Huxley were awarded in 1963 the Nobel prize in Medicine for the study of the ion channels of the giant axon of the squid, subsequently discovering the action potential [36]. Their empirical values were then used to describe the membrane behavior using passive electronic components, as shown in Figure 2.3. The voltage sources represent the resting potential of each ion species, as calculated per the Nernst equation. The variable resistances connected to them represent their transmembrane conductance, which are voltage- and time-dependent for the case of Na^+ and K^+. The leakage branch represents the rest of the ionic currents that are constant or approximately constant during an action potential event, including the currents generated by the ion pumps that maintain the concentration gradients across the membrane [37]. Finally, the capacitor represents the charge separation achieved by the cell membrane. Applying Kirchhoff's law of currents to this equivalent circuit, the following general equation is obtained:

$$C_m \frac{dV_m}{dt} + g_{\mathrm{Na}^+} \cdot (V_m - V_{\mathrm{Na}^+}) + g_{\mathrm{K}^+} \cdot (V_m - V_{\mathrm{K}^+}) + g_L \cdot (V_m - V_L) = 0 \tag{2.1}$$

Hodgkin and Huxley found that the Na^+ ion channels are formed by three activation particles m and one inactivation particle h, whereas the K^+ ion channels are formed by four activation particles n. The values of the conductances of Equation (2.1) depend on the probability of these gating particles of being open at a given time. They modeled the dynamics of the gating particles as a two-state Markov chain that can be described by a first-order differential equation. The transition rates between the states are voltage-dependent. For a very large number of ion channels, the proportion of open ion channels at a given time can be approximated to the probability of one of them being open at that time. Therefore, the overall membrane conductance for a given ion species can be described as the maximum conductance $\bar{g}$ of that species times the probability of that channel being open.

$$\begin{aligned} g_{\mathrm{Na}^+} &= \bar{g}_{\mathrm{Na}^+} \cdot m^3 \cdot h \\ g_{\mathrm{K}^+} &= \bar{g}_{\mathrm{K}^+} \cdot n^4 \end{aligned} \tag{2.2}$$

Thus, Equation (2.1) can be reexpressed as

$$C_m \frac{dV_m}{dt} + \bar{g}_{\mathrm{Na}^+} \cdot m^3 \cdot h \cdot (V_m - V_{\mathrm{Na}^+}) + \bar{g}_{\mathrm{K}^+} \cdot n^4 \cdot (V_m - V_{\mathrm{K}^+}) + g_L \cdot (V_m - V_L) = 0 \tag{2.3}$$

Equation (2.3) models current per unit of area, that is, a limited patch of cell membrane. This segmentation allows the building of an axon model as a spatially distributed version of the Hodgkin-Huxley model, where depolarization occurs locally. In this model, the action potential propagates along the nerve by depolarizing contiguous regions of the membrane. At the region of the action potential, there is an initial strong influx of Na^+ into the cell (Figure 2.4). On the one hand, the higher concentration of Na^+ in the intracellular space causes Na^+ to diffuse to the neighboring regions of the axon, where its concentration is lower. On the other hand, the lower concentration of Na^+ in the extracellular space at the region of the action potential causes Na^+ to diffuse to this region. These diffusion currents depolarize the contiguous patch of cell membrane and trigger another action potential event if the threshold potential is reached. This propagation model works for both myelinated and unmyelinated axons. In the case of myelinated axons, the next depolarizable region is the next node of Ranvier, whereas for unmyelinated axons it is the next predefined unit of area. The Hodgkin-Huxley axon model is then a succession of single Hodgkin-Huxley models with resistors interconnecting them that symbolize the intra- and extracellular resistances [32, 34].

Extraneural interfacing

The action potential has an amplitude span of around 100 mV. To record this signal, intracellular recording techniques, such as the patch clamp technique, have been developed [38]. This technique requires accessing the interior of a neuron with an electrode to measure its electric activity during an action potential event with respect to the extracellular medium. Whereas this recording technique allows for highly sensitive and accurate recordings of the electrical activity of individual neurons, it is also technically challenging and usually restricted to isolated neurons

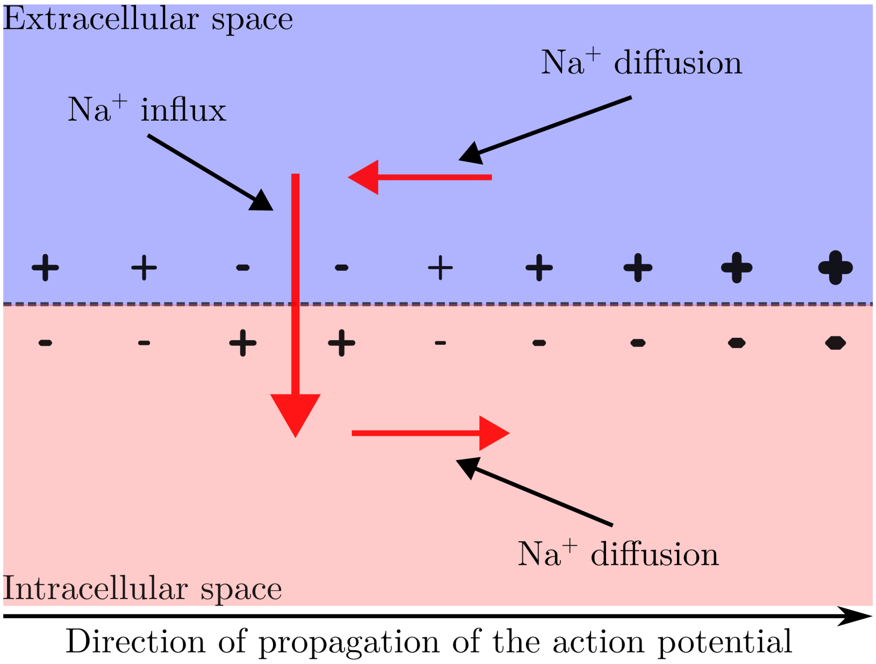
Extracellular space
Na$^+$ diffusion
Na$^+$ influx
+ + - - + + + + +
- - + + - - - - -
Na$^+$ diffusion
Intracellular space
Direction of propagation of the action potential

Figure 2.4: Ion distribution during the propagation of an action potential along an axon.

or in vitro preparations. Furthermore, this technique can cause damage to the cell membrane and requires precise positioning of the electrode and control of its insertion depth, so it is mainly used for research purposes.

On the other hand, in extracellular recordings, an electrode is placed outside of the cell membrane, typically in the extracellular fluid surrounding the cells. During an action potential, the neuron sees an inflow of Na$^+$ followed by an efflux of K$^+$. An electrode placed on the extracellular medium will perceive these ion fluxes as a sink and a source of current, respectively. Therefore, an extraneural electrode detects the voltage changes generated by these currents during an action potential event. These voltage changes are recorded and analyzed to study the electrical properties of neurons and the functioning of the nervous system [39, 40]. The main advantages of extraneural interfacing are that the neuron tissue is unaffected and electrode positioning is less critical than in intraneural interfacing. However, the amplitude of the recorded signals is several orders of magnitude lower, making them more difficult to detect. Another drawback of extraneural interfacing is the lack of selectivity when multiple sources are present, such as in the case of nerves. Nerves comprise multiple axons and many of them can be active at the same time. In this case, extraneural electrodes will have difficulty in determining the sources of the signals because the recorded signal will normally be a superposition of single-unit action potentials, also called a *compound action potential (CAP)*. Normally, several electrodes can be used to attempt to triangulate the source of the signal to increase recording selectivity [41].

Electrical signals are transmitted between the electrons of the electrode and the ions of the solution as capacitive (without charge transfer) and faradic (with charge transfer) currents. Capacitive currents are generated by a redistribution of charges on both sides of the interface and are, in principle, reversible. On the other hand, faradic currents originate from redox reactions and normally generate new species in the solution. In reversible (or pseudocapacitive) faradic reactions, new species are created but stay adsorbed to the interface or in its close vicinity and the reaction can be reversed if the current switches directions [14]. If the newly generated species diffuse away from the electrode and the reaction cannot be reversed by switching the polarity, it is termed irreversible. Normally, nerve stimulation requires the delivery of charge to the extracellular space. Therefore, delivering enough charge to stimulate a fiber while minimizing potentially harmful redox reactions is crucial for nerve stimulation.

Nerve stimulation is triggered by the local depolarization of the cell membrane. Typically, negative charges are injected into the extracellular space to decrease the extracellular potential, which increases V_m. If the cell is depolarized beyond threshold, an action potential is triggered. Thus, the proximity of the electrode to the cell membrane is a key factor in determining the amount of required charge. The further away it is, the more current will be leaked through the gap between the electrode and the nerve tissue and the less efficient the stimulation will be. This leakage can be compensated by increasing the stimulation amplitude but at the cost of triggering stronger redox reactions. One of the most often used techniques to hinder redox reactions is to increase the active area of the stimulation electrodes, thus generating less overpotential for a certain current value.

2.1.2 Peripheral nerve interfaces

Nerves transport a great deal of information between the CNS and the periphery of the body. Ideally, a peripheral nerve interface should be able to address every single axon inside a nerve without interfering with its natural behavior. However, electrodes need to be in close proximity of their target axons to be able to selectively interface with them, which usually involves a highly invasive procedure that damages the biological membranes of the nerve. The interfacing selectivity is a degree of how accurate an electrode is in triggering a response or acquiring the signals from a particular target fiber, without affecting or being affected by the fibers around it.

The invasiveness of the procedure refers to how much the electrode or its implantation procedure damage the neural tissue. In this compromise between the selectivity of the interfacing and the invasiveness of the procedure, several PNI strategies have been developed, as shown in Figure 2.5. Generally, PNI can be classified into intraneural and extraneural, depending on whether the electrodes penetrate the nerve. In the following, a brief review of the state-of-the-art regarding PNI is provided [17].

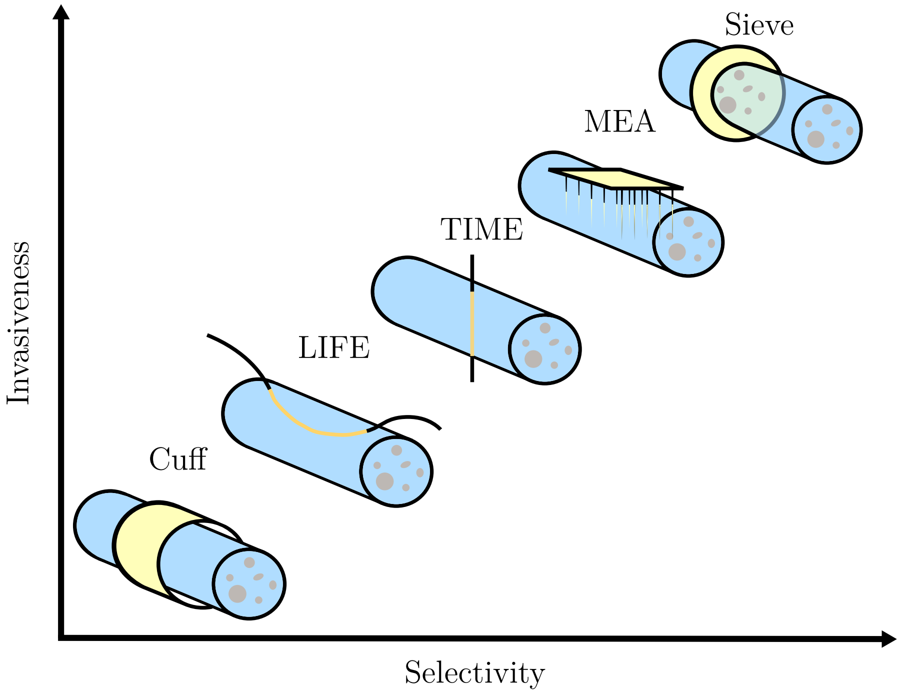

Figure 2.5: Conceptual chart relating invasiveness and selectivity of peripheral nerve interfaces.

Intraneural PNI

Intraneural electrodes are characterized by a higher selectivity of the target axons or fascicles but at the cost of damaging the natural structure of the nerve. If they penetrate the epineurium and lie in between the fascicles without breaching the blood-nerve barrier, they are termed *interfascicular* [42–44]. If they also penetrate the fascicles, thus achieving higher axon selectivity, they are called *intrafascicular*. This kind of electrodes offers the most efficient stimulation and most selective recording of all [45]. However, damaging the nerve tissue generates nerve trauma and triggers a strong foreign body response (FBR) [46]. Due to this fact, intraneural nerve interfaces present, in general, a shorter useful duration than extraneural nerve interfaces [47, 48].

The longitudinal intrafascicular electrode (LIFE) was one of the first developed intraneural interfaces [49, 50]. It consists of a thin wire carrier with the electrodes distributed along its length inserted longitudinally along the nerve with the aid of a needle. Newer versions are smaller to reduce the trauma, fabricated with polyimide (PI) and called thin-film LIFE (tfLIFE) [51].

The transversal intraneural multichannel electrode (TIME) presents a similar structure to the LIFE, but it is inserted transversely across the nerve [52, 53]. A known issue of the TIME is the relative displacement of its electrodes with respect to the nerve fibers over time. To account for this issue, an improved version of the TIME is the self-opening intraneural peripheral interface (SELINE) [54]. This device is made from PI and features flaps to its sides that spread when the electrode is pulled back, fixing it to a position.

The microelectrode array (MEA) originally developed for brain interfacing was translated to nerves in 2000 and has also been used for high-resolution PNI [55]. It consists of a needle bed that is pushed into the nerve and permits parallel recordings of multiple channels. However, both its implantation is challenging when piercing the perineurium due to the high electrode density and its FBR is very strong, hindering long-term interfacing.

Finally, sieve electrodes are one of the most selective but invasive designs. They consist of a flat circular structure with orifices on its surface where the electrodes are located [56]. Their interfacing requires cutting the nerve, positioning the electrode between the nerve ends and letting the nerve regrow through the device. However selective, the success rate of regrowth keeps being a limiting factor, and its invasiveness rarely justifies its use beyond research purposes [57].

Extraneural PNI

Extraneural electrodes are fixed on and around the epineurium of the nerve and are, therefore, the least invasive kind of neural interfaces. However, since they can only interface the nerve through its surface, targeting the inner fibers becomes a difficult task, thus decreasing their selectivity. The most traditional structures for extraneural nerve interfacing are the nerve cuffs [17]. The cuff has a tubular geometry with the electrodes placed on the inner face of the tube. They present the advantage of confining the ionic currents inside the structure and reducing the leakage currents, which increases the signal-to-noise ratio (SNR) for recording and decreases the current needed to stimulate the nerve. Generally, their interfacing procedure is also straightforward, as it consists of wrapping the structure around the nerve and suturing or gluing it to fix it closed. Since they are the least invasive, they can be used over longer periods of time [39, 58]. A particular type of cuff electrode is the *flat interface nerve electrode* (FINE) [19]. This device flattens the nerve by compressing it and causes the fascicles to move toward the surface of the nerve, where they can be targeted more easily and specifically.

Further extraneural devices include the helicoidal electrodes, designed to self-close and conformally wrap around the nerve. While they are easy to implant and explant, their open geometry causes leakage currents and decreases recording efficiency [31, 59]. Finally, the book electrode is made of a block of silicone with deep trenches carved into it on one side that resemble the back and pages of a book [60]. It has been designed for bladder control by interfacing the sacral nerve roots in patients with spinal cord injury.

2.2 Electrochemical characterization

Nerve interfacing is often based on the principles of electrochemical charge transfer between the electrode and the electrolyte and/or nerve tissue. Analyzing the electrochemical properties of the used electrodes is important to understand their behavior and limitations. In this section, I introduce the fundamentals of the electrode-electrolyte interface and standard electrochemical methods to characterize it.

2.2.1 The electrode-electrolyte interface

When an electrode is immersed into an electrolyte solution, a potential difference originates naturally between them. A model to explain this electrode-electrolyte interface phenomenon was presented by Herman von Helmholtz in 1879 [61]. In his model, the potential difference creates an electric field at the interface that attracts counterions to it and pushes the coions back into the electrolyte solution. The attracted counterions form a layer adsorbed to the surface of the electrode, balancing the excess charge and canceling the electric field around the interface (Figure 2.6).

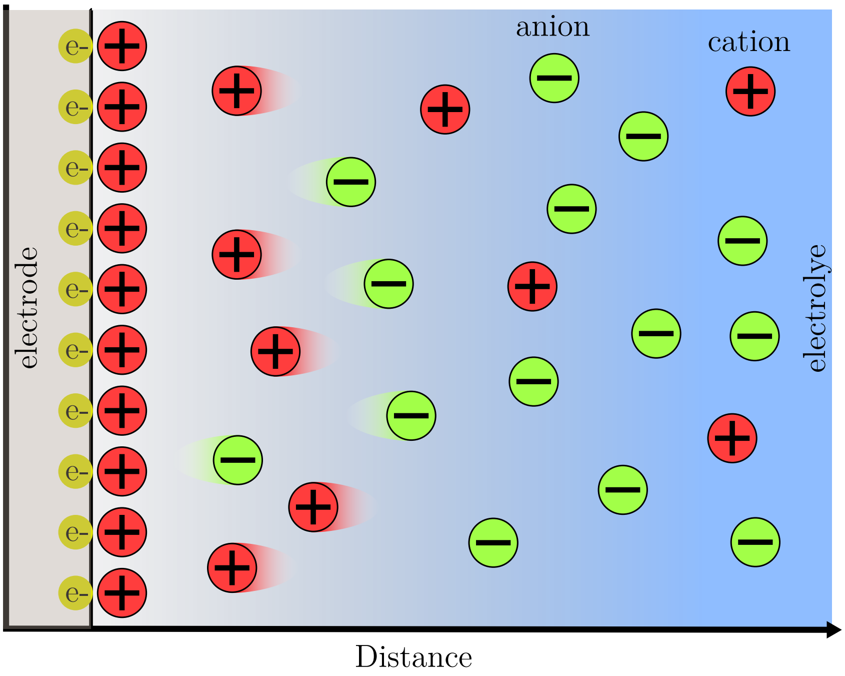

Figure 2.6: Electrode-electrolyte interface. A negatively charged electrode is submerged into an electrolyte solution with positive and negative charges. Cations are driven by the electric field towards the interface and adsorb to it, shielding the electric field from the bulk of the solution. Anions are also electrically driven into the bulk of the electrolyte solution. Since the electric field is shielded, the ions in the bulk of the solution do not feel electrostatic force.

Since the interface separates charges without charge transfer, this phenomenon can be modeled as a parallel plate capacitor, in which the specific capacitance, that is, the capacitance per unit area, is described as

$$C''_H = \frac{\varepsilon}{r} \tag{2.4}$$

where ε is the permittivity of the electrolyte and r is the spatial separation between charges. The original model approximated r as the radius of the ion, whereas later models considered the radius of a solvated ion, i.e., surrounded by water molecules.

Gouy (1910) and Chapman (1913) introduced another electrode-electrolyte model considering the thermal diffusion of the ions. In this model, the ion distribution is not a perfect plane adsorbed to the electrode but a concentration distribution c_i in the vicinity of the surface governed by the Maxwell-Boltzmann statistics [62]. This concentration distribution is expressed as

$$c_i = c_{i,\infty} \exp\left(-\frac{z_i F \phi}{RT}\right) \tag{2.5}$$

where $c_{i,\infty}$ is the ion concentration in the bulk of the electrolyte far away from the electrode, z_i is the ion's valence, F is the Faraday constant, ϕ is the electric potential, R is the gas constant and T is the absolute temperature of the electrolyte. The charge density near the electrode is, therefore, the sum of the ions for all the species i, times their valence z_i times the Faraday constant.

$$\rho_E = \sum_i z_i F c_i = \sum_i z_i F c_{i,\infty} \exp\left(-\frac{z_i F \phi}{RT}\right) \tag{2.6}$$

The Poisson equation for electrostatics relates the electric potential to the local net charge density as

$$\nabla^2\phi = -\frac{\rho_E}{\varepsilon} \tag{2.7}$$

Substituting Equation (2.6) in Equation (2.7) yields the Poisson-Boltzmann equation (Equation (2.8)), which explains the double layer approximating the ions to point charges.

$$\nabla^2\phi = -\frac{F}{\varepsilon}\sum_i z_i c_{i,\infty} \exp\left(-\frac{z_i F\phi}{RT}\right) \tag{2.8}$$

The Poisson-Boltzmann equation does not have a solution for the general case. However, under certain considerations, an analytic solution can be obtained. One such consideration is the Debye-Hückel approximation, which states that for small potentials $\left(\phi \ll \frac{RT}{z_i F}\right)$, the equation can be approximated to its first-order Taylor expansion. In this case, the solution is given by

$$\phi = \phi_0 \exp\left(\frac{-d}{\lambda_D}\right) \tag{2.9}$$

where ϕ_0 is the potential at the electrode, d is the distance from the electrode and λ_D is the Debye length, expressed as

$$\lambda_D = \sqrt{\frac{\varepsilon RT}{F^2 \sum_i z_i^2 c_{i,\infty}}} \tag{2.10}$$

The Debye length gives a measure of the characteristic length of the decay of the potential into the bulk. Under the Debye-Hückel approximation, the double-layer capacitance can be expressed as

$$C''_{GC,DH} = \frac{\varepsilon}{\lambda_D} \tag{2.11}$$

Whereas the Gouy-Chapman model is more accurate than the Helmholtz model at explaining the charge distribution next to the walls, it approximates the ions to point charges, with no constraints regarding how many charges can be adsorbed to the walls. A solution to this issue was proposed in 1924 by Otto Stern, proposing a combination of both models: the Helmholtz capacitor explains the charge concentration next to the walls and the Gouy-Chapman capacitor further away from the walls [62]. The resulting double-layer model is called the Gouy-Chapman-Stern model and features both capacitors in series.

$$\frac{1}{C''_{GCS}} = \frac{1}{C''_{H}} + \frac{1}{C''_{GC}} \tag{2.12}$$

2.2.2 Electrochemical methods

According to the interface models presented so far, it is assumed that shifting the electrode potential from its equilibrium value, i.e., polarizing the electrode, will result in a redistribution of the dissolved ions within the electrolyte solution. Electrodes with this behavior are termed *ideally polarizable* and normally do not exist in nature [63]. In reality, polarizing an electrode changes the electron energy at its interface. If this energy level becomes higher than the lowest unoccupied molecular orbit (LUMO) of an ion species in the solution, an electron from the electrode is transferred to the LUMO of the ion. An electrode that donates electrons is termed *cathode*. Correspondingly, if the highest occupied molecular orbit (HOMO) of an ion species is higher than the energy of the electrons at the electrode, an electron is transferred from the HOMO to the electrode [64]. In this case, the electrode is termed *anode*.

Electrodes are characterized in *electrochemical cells*, consisting of the electrodes submerged in an electrolyte solution. The electrode under study is conventionally referred to as the *working electrode*. To measure the working electrode, another electrode, called the *reference electrode*, is required. These reference electrodes are designed so that their voltage drop remains as constant as possible during measurement to provide a stable reference voltage. This setup is called a *two-electrode setup* and is normally used to measure the equilibrium or open circuit potential E_{oc} of the electrode. Conventionally, the standard hydrogen electrode (SHE) is used as a universal reference, with an equilibrium reaction described as $2\,\mathrm{H}^+ + 2\,\mathrm{e}^- \rightleftharpoons \mathrm{H}_2$. Another popular reference electrode is the Ag/AgCl electrode. Its equilibrium reaction is $\mathrm{AgCl} + \mathrm{e}^- \rightleftharpoons \mathrm{Ag} + \mathrm{Cl}^-$ and shows an equilibrium potential of 0.197 V vs. SHE in a saturated KCl solution at room temperature [63].

Most electrochemical techniques require polarizing the working electrode and measuring the generated current. In these cases, a third electrode, called the *counter electrode* or *auxiliary electrode*, is used to close the circuit with the working electrode. Setups comprising a counter electrode are called *three-electrode setups*. Noble metals, like Pt, or graphite are typical materials for counter electrodes since they are non-corrosive materials. Furthermore, these electrodes usually have a larger surface area than the working electrode, usually in the form of a mesh, to prevent the influence of kinetic reactions at the counter electrode from affecting the measurement. The counter electrode is better positioned far away from the working electrode to prevent its reactions from changing the electrolyte characteristics close to the working electrode. On the other hand, the reference electrode is often placed close to the working electrode to minimize the influence of ohmic voltage drop on the electrolyte over the distance that separates them.

A potentiostat is a device that can modulate the energy level of the electrons at the electrode and measure the transmitted current. In this way, an electrode-electrolyte interface can be characterized through electrochemical measurements. In this work, I characterized the electrodes using three techniques, namely *cyclic voltammetry* (CV), *voltage transients measurements* (VT) and *electrochemical impedance spectroscopy* (EIS).

Cyclic voltammetry

Cyclic voltammetry (CV) is an electrochemical technique used to investigate redox reactions of a molecular species [64]. A typical CV measurement consists of sweeping an electrical potential E between two vertex potentials E_a (anodic vertex potential) and E_c (cathodic vertex potential) and measuring the resulting current i through the electrode. The rate at which this potential is swept is called the *scan rate* (ν) and it is important because faster scan rates result in a reduction in the thickness of the diffusion layer, which results in higher measured currents. The $i - E$ curve obtained from a CV experiment is called a *voltammogram*. An exemplary voltammogram is presented in Figure 2.7. For large electrodes, in which mass transport plays a role, the voltammogram presents a duck shape, which can be explained as follows. As the voltage changes between the vertex values, the electrode gets polarized and redox reactions cause current to flow. The current (either anodic or cathodic) keeps on increasing with the voltage according to the reaction kinetics up to its peak value i_P at the voltage level E_P, where the amount of reactant in the vicinity of the electrode decreases. At this point, the supply of reactant to the electrode is limited by mass transport from the bulk, which causes the current to decrease. The shape of the voltammogram is further affected by other electrochemical effects on the surface of the electrode, such as adsorption and desorption during the sweeps.

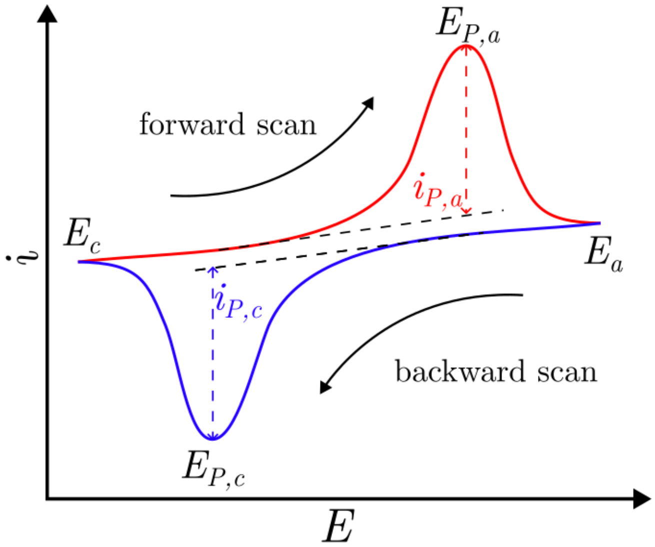

Figure 2.7: Exemplary voltammogram of a redox reaction. E represents the applied potential to the electrode and i the measured current. E_c and E_a are the cathodic and anodic vertex potentials, respectively. i_P is the peak current measured and the potential at which this happens is the E_P.

From the voltammogram, information on the reaction process can be obtained. For example, one can assess the reversibility of the process if E_P keeps the same value for all the sweeps. The Randles-Sevcik equation relates the measured peak current i_P to the scan rate ν for electrochemically reversible electron transfer processes in which the species involved diffuse freely as

$$i_P = 0.446 nFAc_\infty \sqrt{\frac{nF\nu D}{RT}} \tag{2.13}$$

where n is the number of electrons transferred in the redox reaction, F is the Faraday constant, A is the electrode area, D is the diffusion coefficient, c_∞ is the bulk concentration of the redox species, R is the gas constant and T the absolute temperature.

A popular parameter that can be estimated from the voltammogram is the *charge storage capacity* (CSC). This parameter represents the amount of charge per unit area that an electrode can store in reversible processes, e.g., charging of the double layer or charge adsorption. The definition of this parameter varies across the scientific literature and it is often calculated differently [65–68]. One way to define the CSC is as the area enclosed by a voltammogram obtained with a slow scan rate (e.g., $50\,\mathrm{mV\,s^{-1}}$) in the potential range of reversible reactions. Usually, the limits of this range correspond to the oxidation and reduction potentials of water, also called the *water window*. The CSC can be further separated into its cathodal ($\mathrm{CSC_c}$) and anodal ($\mathrm{CSC_a}$) parts, defined by the areas enclosed by the cathodic and anodic currents, respectively, as shown in Figure 2.8.

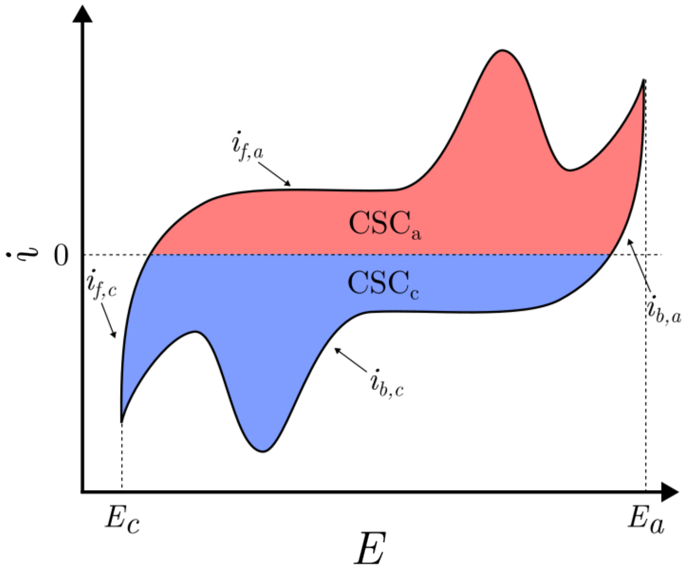

Figure 2.8: A sample voltammogram highlighting the CSC$_\mathrm{c}$ and the CSC$_\mathrm{a}$ as the areas enclosed by the cathodic and anodic currents, respectively. The cathodic and anodic currents are further separated into the portions obtained during the forward ($i_{f,c}$, $i_{f,a}$) and backward ($i_{b,c}$, $i_{b,a}$) scans.

In this work, the CSC$_\mathrm{c}$ is used for electrode characterization and is calculated as

$$CSC_c = \frac{1}{\nu A} \int_{E_c}^{E_a} |i_{b,c} - i_{f,c}| \, dE \tag{2.14}$$

where ν is the scan rate, A is the area of the electrode, E_c and E_a are the cathodic and anodic vertex potentials, respectively, $i_{b,c}$ is the cathodic part of the current recorded during the backward scan and $i_{f,c}$ is the cathodic part of the current recorded during the forward scan.

Voltage transients

One important characteristic of stimulation electrodes is their ability to deliver enough current to trigger a physiological response while minimizing or avoiding irreversible electrochemical reactions. The *charge injection capacity (CIC)* of an electrode estimates the amount of charge per unit area that can be delivered without causing these reactions and is calculated by using the *voltage transients technique (VT)*. The VT consists of applying a current pulse to an electrode immersed in an electrolyte solution and determining its maximum polarization potentials, both cathodic (E_{mc}) and anodic (E_{ma}). Then, these potentials are compared to the safe polarization limits that do not cause irreversible reactions, which are often defined as the potential limits of the water window. Usually, voltage transients are recorded in a three-electrode setup.

Figure 2.9 shows a typical voltage transient obtained by applying a cathodic-leading biphasic current signal. The potential before the stimulation pulse is applied is called the *interpulse potential* (E_{ipp}). The voltage response to the applied signal can be separated into the voltage drop generated mainly by the ohmic resistance of the electrolyte, also called *access voltage* (V_a), and the electrode *polarization voltage* (V_p) [65]. Only V_p contributes to the calculation of the maximum polarization potentials E_{mc} and E_{ma}. For instance, for a cathodal current pulse, E_{mc} is calculated as

$$E_{mc} = E_{ipp} + V_p \tag{2.15}$$

It is worth noting that V_p has a negative value in this case. Nevertheless, determining V_p is more challenging than determining V_a. Therefore, it is useful to define $\mathit{\Delta} V = V_a + V_p$ and calculate E_{mc} as

$$E_{mc} = E_{ipp} + (\mathit{\Delta} V - V_a) \tag{2.16}$$

The CIC is finally estimated by finding the charge density whose maximum polarization voltage (E_{mc} or E_{ma}) is equal to the safe polarization limit.

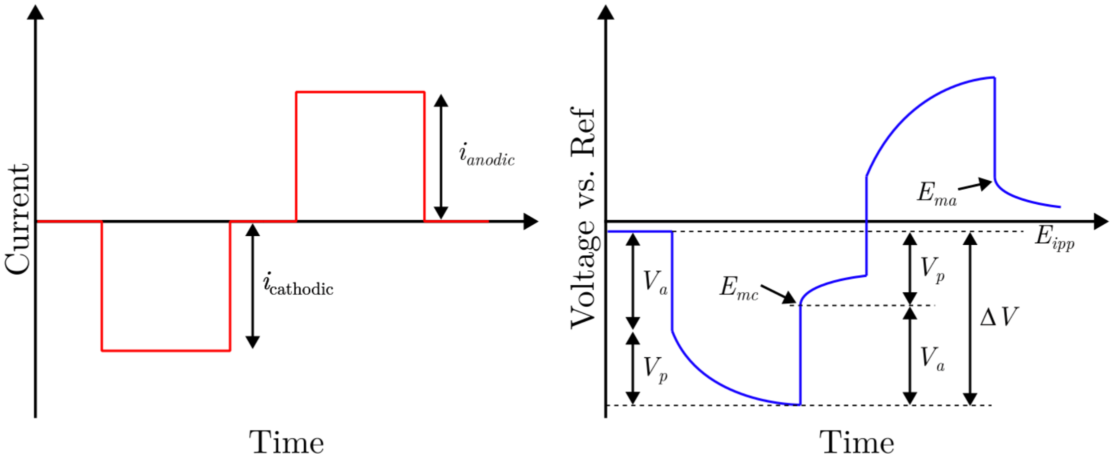

Figure 2.9: An exemplary voltage transient response to a biphasic current pulse.

CSC and CIC are closely related parameters. While CSC represents the charge an electrode can store, the CIC represents what portion of this charge can be used for stimulation purposes. Therefore, materials with high CIC are desired for stimulation electrodes.

Electrochemical impedance spectroscopy

The current response of an electrode in an electrolyte solution to an applied voltage is highly non-linear due to the processes at the surface of the electrode, as seen in Figure 2.7. However, if the voltage excursion is small enough, one can linearly approximate the current response of the system and compute its impedance. *Electrochemical impedance spectroscopy (EIS)* is a powerful method that characterizes the impedance of an electrode over a range of frequencies.

The process consists of applying a small-signal voltage perturbation, usually a sinusoidal waveform of around 10 mV, and recording the current. If a sinusoidal wave $v(t)$ of frequency ω in phasor form is applied to the system as

$$v(t) = |V| \tag{2.17}$$

the obtained current $i(t)$ for the general case is

$$i(t) = |I|e^{-j\phi} \tag{2.18}$$

Then, the system impedance for that frequency results

$$Z = \frac{|V|}{|I|}e^{j(0-(-\phi))} = |Z|e^{j\phi} \tag{2.19}$$

The impedance Z is normally a complex number, with its real part representing the energy dissipation and the imaginary part the energy storage. A characteristic impedance permits the description of the electrode surface with electrical components to model electrochemical properties. The simplest model represents the interface as a capacitor C_{dl}, modeling the double-layer capacitance. An extended model also considers the charge transfer processes, modeling it as a resistor R_{ct} in parallel with C_{dl}. Ohmic drops along the electrolyte are further characterized with another resistor

R_e. A model with these three components is called a *simplified Randles circuit* and it is shown in Figure 2.10. Alternatively, the C_{dl} can be replaced with a constant phase element to better fit experimental data. A fourth component, the Warburg impedance, can be incorporated in series with R_{ct} to model diffusion processes.

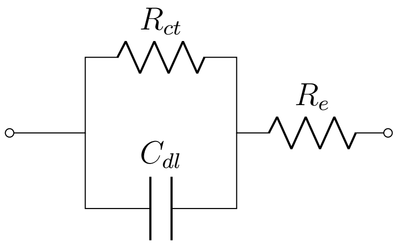

Figure 2.10: Simplified Randles circuit.

In this section, I have presented the electrochemical background of the electrode-electrolyte interface and some common techniques to characterize the interfacing electrodes. In the next section, I introduce the animal model used for the in vivo nerve interfacing experiments.

2.3 Animal model: *Locusta migratoria*

The nervous systems of insects retain the basic characteristics of that of higher-order organisms, making insects suitable for neural research. The animal model used in this work is a locust, a type of short-horned grasshopper. The locust species used is *Locusta migratoria*, which belongs to the Acrididae family, in the order Orthoptera (Figure 2.11) [69]. Locusts are able to jump long distances by a rapid extension of their hind legs. Triggering the jumping of the locust through nerve stimulation could lead to the development of insect-machine hybrid robots, which could be employed, for instance, in search-and-rescue missions in disaster areas. Furthermore, this model could be enhanced by incorporating neural recordings as a feedback pathway to control the jumping in a closed-loop fashion. Figure 2.12 presents a sequence of pictures showing a locust jumping taken with a high-speed camera at 10000 fps.

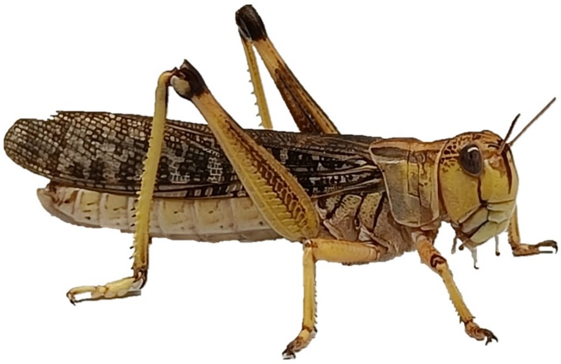

Figure 2.11: The locust of the species *Locusta migratoria* was the main experimental subject for this work.

In the following, I describe the anatomy and the nervous system of this animal model.

2.3.1 Anatomy

Locusts present an articulated exoskeleton made of cuticle, which forms either hard plates (sclerites) or soft membranes. Their body consists of three main parts: the head, the thorax and the abdomen [71]. The head presents the mouthparts, and various sense organs, such as the antennae and the compound eyes. The thorax is, in turn, composed of three connected segments: the prothorax, the mesothorax and the metathorax. Each segment presents a pair of legs on each side that enable the locomotion of the animal. In particular, the metathoracic legs, or hind legs,

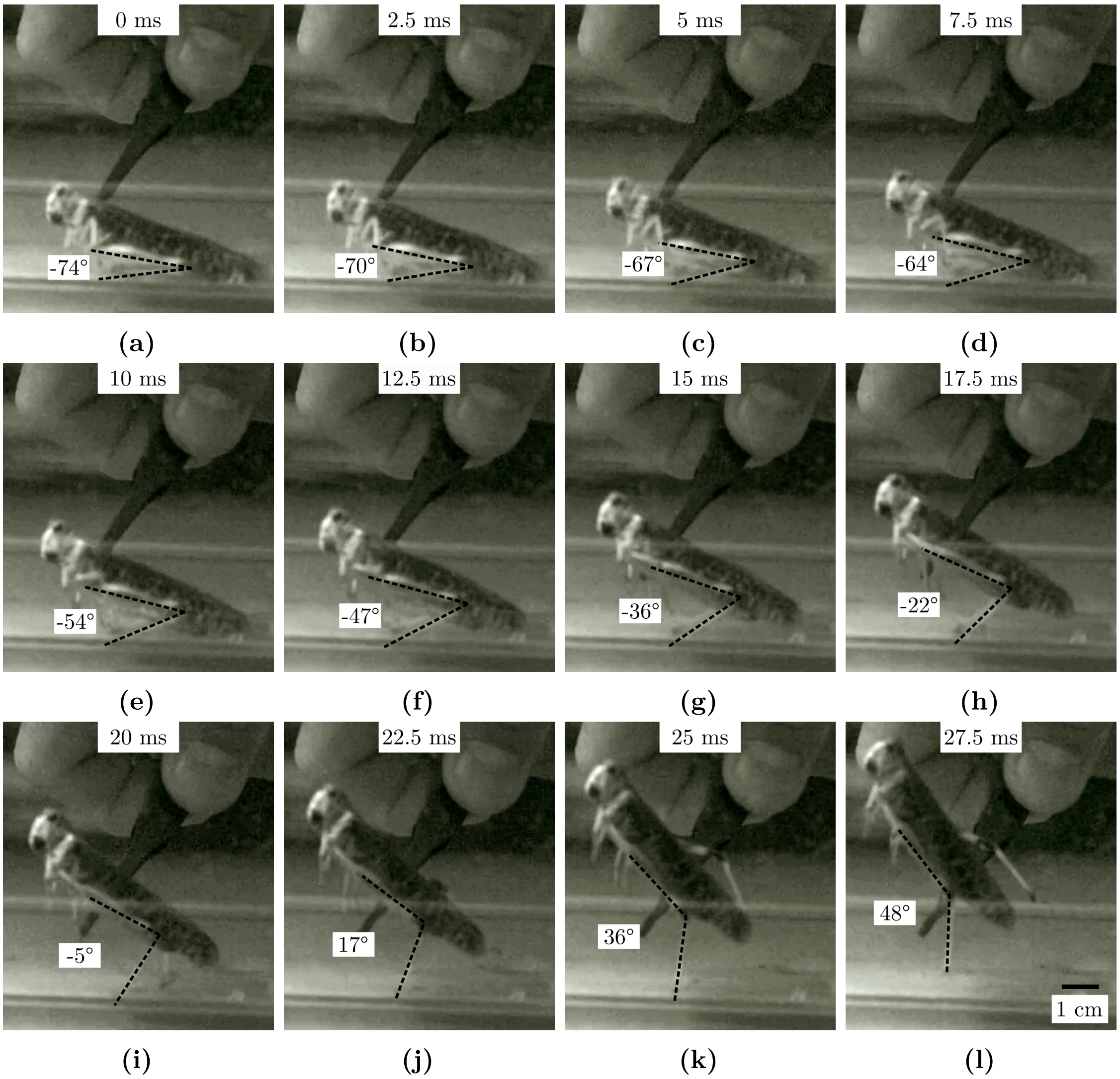
0 ms
-74°
2.5 ms
-70°
5 ms
-67°
7.5 ms
-64°
(a)
(b)
(c)
(d)
10 ms
-54°
12.5 ms
-47°
15 ms
-36°
17.5 ms
-22°
(e)
(f)
(g)
(h)
20 ms
-5°
22.5 ms
17°
25 ms
36°
27.5 ms
48°
1 cm
(i)
(j)
(k)
(l)

Figure 2.12: Jumping behavior of a locust captured with a high-speed camera at different timestamps. The tibiofemoral angle of the hind leg is shown, with 0° corresponding to the leg position in which the tibia is perpendicular to the femur. The images were digitally corrected using `enhance.pho.to`. The tibiofemoral angle was estimated using ImageJ [70].

are significantly larger and stronger than the others because they permit the strong jump of the locust. Finally, the abdomen is composed of eleven segments and the posterior telson. A diagram of the anatomy of a typical *Locusta migratoria* is shown in Figure 2.13.

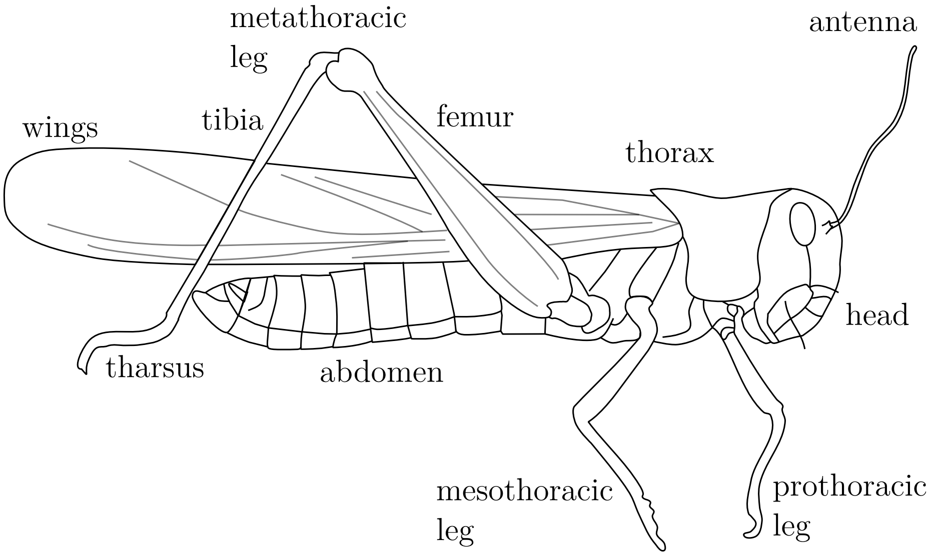
metathoracic
leg
antenna
wings
tibia
femur
thorax
head
tharsus
abdomen
mesothoracic
leg
prothoracic
leg

Figure 2.13: Diagram of the anatomy of the *Locusta migratoria*.

2.3.2 Nervous system

Most of the neurons of the locust are monopolar, with a single projection from the soma that splits to form the dendrites and the axon [71]. The central nervous system (CNS) and the large branches of the peripheral nerves are protected by the perineurium. The perineurium, in turn, is surrounded by a thick layer called the *neural lamella*. The combination of the perineurium and the neural lamella forms the *nerve sheath*, which protects and nourishes the nerve [72, 73].

The CNS of the locust comprises the brain in the head and nine ganglia that run along the ventral side of the body [74]. The first is the subesophageal ganglion which controls the movement of the mouthparts. Directly posterior to this come the pro-, meso- and metathoracic ganglia. Each ganglion has five or six nerves branching to each side that innervate the muscles and sensilla of the thorax. These ganglia control mainly the legs and wings, so they are important for the animal locomotion. The last five are the smaller abdominal ganglia [71]. The brain and the ganglia are joined by interganglionic connectives, making them work as a central nervous processing unit. A 3D schematic of the ganglia relative to the locust body is shown in Figure 2.14.

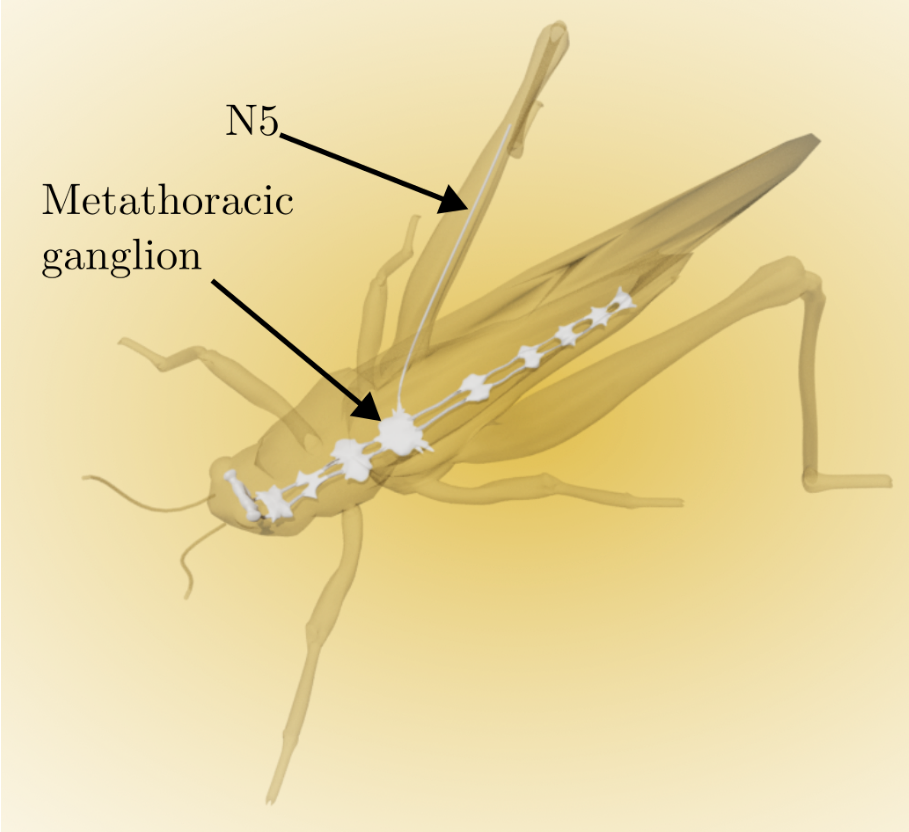

Figure 2.14: 3D model of the nervous system of the *Locusta migratoria.* The chain of ganglia is displayed in white, with a reference N5 emerging from the metathoracic ganglion and innervating the hind leg.

In this work, the movement of the hind leg of the locust was chosen as the standard biomarker for stimulation experiments. The hind leg is innervated mainly by the fifth nerve (nerve 5 or N5) of the metathoracic ganglion and it comprises sensory (afferent) and motor (efferent) neurons [75–77]. Figure 2.15 shows a cross-sectional view of the N5 at the level of the metathorax. One advantage of the locust is that only about 70 motoneurons totally control the movement of this leg, including fast and slow extension, flexion, and tarsal movement, naturally enhancing selective stimulation compared to mammals [78]. One particular motoneuron found in the N5 is called the *fast extensor tibiae (FETi)*, which is involved in the jump of the locust. This nerve fiber is around 15 µm in diameter, around three times larger than the rest of the fibers [75, 79, 80]. Neural recordings were also obtained from this nerve, both afferent and efferent. All the nerve interfacing procedures and neural recordings were carried out on the N5, unless stated otherwise.

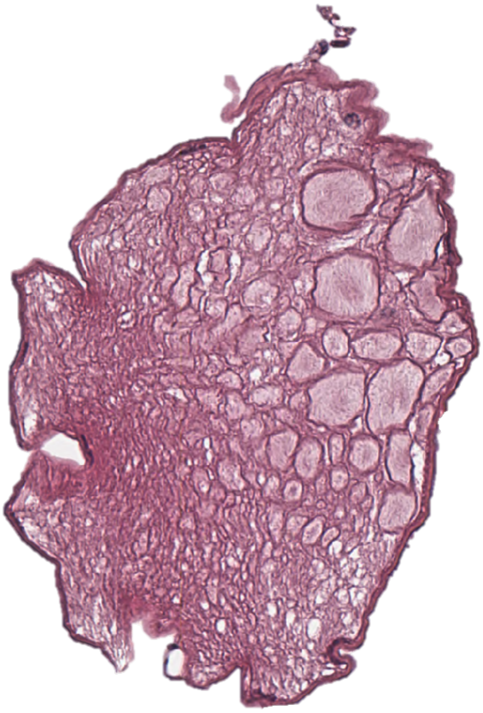

Figure 2.15: Cross-sectional view of the N5 of a *Locusta migratoria* at the level of the metathorax. The tissue slice has been stained with hematoxylin-eosin. The pink regions represent the axons. It can be seen that the axon size distribution is not uniform, with some fibers being visibly larger than others. The fuchsia structure that surrounds the nerve is the nerve sheath. This Figure was obtained in collaboration with Dr. Tanja Groll and PD Dr. Katja Steiger, Comparative Experimental Pathology, Technical University of Munich.

CHAPTER 3

Initial steps: rapid prototyping of a small nerve cuff

The chapter was reproduced in part with permission from Francisco Zurita, Fulvia Del Duca, Tetsuhiko Teshima, Lukas Hiendlmeier, Michael Gebhardt, Harald Luksch and Bernhard Wolfrum. The original publication "F. Zurita et al., In vivo closed-loop control of a locust's leg using nerve stimulation. *Sci Rep.* **2022** Jun 27;12(1):10864. PMID: 35760828; PMCID: PMC9237135." is available on `https://www.ncbi.nlm.nih.gov/pmc/articles/PMC9237135/`, doi: 10.1038/s41598-022-13679-z.

3.1 Preamble

Activity of an innervated tissue can be modulated based on an acquired biomarker through feedback loops. How to convert this biomarker into a meaningful stimulation pattern is still a topic of intensive research. In this chapter, I present a simple closed-loop mechanism to control the mean angle of a locust's leg in real time by modulating the frequency of the stimulation on its extensor motor nerve. The nerve is interfaced with a custom-designed cuff electrode and the feedback loop is implemented online with a proportional control algorithm, which runs solely on a microcontroller without the need of an external computer. The results show that the system can be controlled with a single-input, single-output feedback loop. The model described in this chapter can serve as a primer for young researchers to learn about neural control in biological systems before applying these concepts in advanced systems.

3.2 Introduction

Interfacing the nervous system with stimulation and recording devices can be used to diagnose and treat nervous system disorders. Such neurotechnology-based concepts are successfully exploited in a variety of medical applications: in the central nervous system, cochlear implants are routinely used to restore hearing by directly stimulating the auditory nerve. In addition, deep brain stimulation is applied to treat symptoms from Parkinson's disease and depression [81, 82]. Furthermore, several strategies for specific disease treatment have recently evolved based on bioelectronic interfacing with the peripheral nervous system. For example, electric stimulation of the vagus nerve has been used for the treatment of epilepsy and depression, and research is being conducted on its effectiveness to treat heart conditions and even respiratory symptoms associated with COVID-19 [10, 13, 83–85]. Stimulation of the posterior tibial nerve has been investigated to treat incontinence [86] and transcutaneous electrical nerve stimulation (TENS) has long been used as a palliative for chronic pain [87]. Applying neural modulation in humans is difficult due to complex, time-dependent, and largely uncharacterized response behavior. This means that the same stimulus may yield different responses, not only when applied in different subjects (inter-subject variability) [88], but also within the same subject at different times (intra-subject variability) [89, 90]. Since the most commonly applied method of modulating neural activity is in an open-loop fashion, i.e., without monitoring the output variable, the response has high variability. To account for this variability, a closed-loop strategy is crucial to monitor the desired outputs and adapt the modulation parameters accordingly to achieve some degree of control over the output variable [91–96]. The concept of control in the scope of this chapter should be understood from a control theory perspective, in which the use of an output signal of a system is used to modify the command signal of this system to reduce the difference between the desired and actual output signal [97]. Sun et al. review four clinical cases where closed-loop systems were used with better results compared to open-loop systems [98] . Kassiri et al. discuss the benefits of closed-loop stimulation in the treatment of epilepsy [99]. In view of the advantages, new devices with potential for closed-loop applications are emerging for the peripheral [100, 101], and the central nervous system [102, 103]. In particular, implantable and potentially adaptive systems are desired for long-term studies. In this context, multisite electrodes have been leveraged to selectively stimulate appropriate nerve fibers [104] and miniaturization as well as power delivery strategies have been implemented [105, 106].

Fundamental research on closed-loop bioelectronic intervention strategies is typically carried out using animal models, usually rodents and other smaller mammals. For example, closed-loop vagus nerve stimulation has been shown to enhance recovery of spinal cord injury in rats [106] , and a closed-loop gait control system has been demonstrated in a cat [107]. Furthermore, a closed-loop approach targeting the peripheral nervous system has been shown for bladder control using optogenetic methods in mice [108]. Different strategies have also been explored to achieve a closed-loop control using frequency-modulated stimulation. Wenger et al. presented a neuromodulation approach for gradual control of mammalian gait, by targeting the spinal cord and recruiting the sensory fibers that elicit a leg reflex movement [109]. Choosing an appropriate control approach can enhance fiber selectivity, which is important to prevent eliciting undesired responses [6].

As an alternative to mammals, insects prove to be useful animal models for fundamental research as well as educational purposes. Their nervous system is simpler than that of mammals and allows for more precise targeting of the tissue. Additionally, in vitro studies with insects permit the analysis and characterization of their different subsystems, isolated from the influence of the rest of the body [110]. Insects have also inspired computational models to test various control strategies, making them a versatile model [111–113]. While different approaches and electrode designs have been proposed to interface with peripheral nerves in literature [114, 115], the small size of peripheral nerves limits their applicability in insects. For this reason, many in vivo experiments carried out on insects attempt to close the loop by directly applying electrical stimulation to the target muscles instead of the nerve innervating them [110, 116, 117].

In this chapter, I demonstrate the control of a locust's leg angle extension via a feedback-loop strategy by directly stimulating one of the extensor motor nerves. A nerve cuff is fabricated using a 3D-printed mold allowing rapid prototyping of the interface. The elicited leg movement is measured with a commercial flexible resistor and controlled in real time using a train of digital-level voltage pulses implemented with a microcontroller.

3.3 Materials and methods

3.3.1 Control loop design

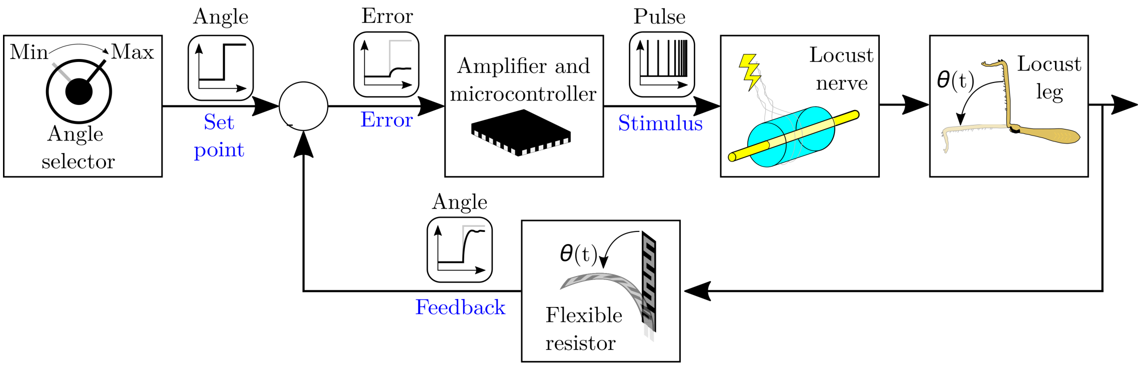
Min
Max
Angle selector
Angle
Set point
Error
Error
Amplifier and microcontroller
Pulse
Stimulus
Locust nerve
θ(t)
Locust leg
Angle
Feedback
θ(t)
Flexible resistor

Figure 3.1: Scheme of the implemented control loop. The angle set point is selected and the measured leg angle subtracted from it to conform the error signal, which is sampled by the microcontroller. A proportional control algorithm runs in the microcontroller, varying the period of the stimulus signal applied on the nerve. The leg angle is sensed with a flexible resistor to provide the feedback.

Figure 3.1 shows a scheme of the proposed control loop. It starts with the selection of the desired angle set point. The feedback signal is then subtracted from the set point signal to produce an error signal. We implemented the subtraction with an operational amplifier (TL094, Texas Instruments, Dallas, USA) in a differential configuration. Both signals are buffered with operational amplifiers in voltage-follower configurations before subtraction and the amplitude of the feedback signal is calibrated to match the amplitude of the set point signal. The error signal is sampled using the internal analog–to–digital converter (ADC) of the microcontroller (nRF52840, Nordic Semiconductor, Oslo, Norway) at a sampling rate of 10 ksps. We configured the microcontroller to generate a train of monophasic pulses with a fixed pulse width of 100 µs and an amplitude of 3 V. The period of the applied train pulses is modulated proportionally to the error signal. We limited the duration of the pulses to 100 µs to avoid redox reactions that could be generated due to the large amplitude of the stimulation. The period of the output is calculated as $T = 250\,\mathrm{ms} - A \cdot e(t)$, where T is the output period, $e(t)$ is the error signal in V, and A is an amplification factor, which was empirically set to $0.36\,\mathrm{s\,V^{-1}}$. The output period is clipped to a minimum of 50 ms and a maximum of 250 ms. A flexible resistor (ZD10-100, Fafeicy) attached to the leg using a 50-µm nylon string measured the joint angle. A set of pulleys guide the string along a path that increases the bending of the resistor with the joint angle and thus, increases the error signal. The angle span goes from 0° to 90°, making the flexible resistor change its impedance from 50 to 3 kΩ.

3.3.2 Electrode fabrication

We implemented a simple 3D fabrication approach that allows rapid prototyping of cuff electrodes. The cuff electrodes were designed to fit the diameter of the targeted nerve. First, we fabricated molds to shape the cuff into a cylinder. The layout for the molds was designed using a 3D computer-aided design software (Fusion 360, Autodesk, Inc., San Rafael, USA). We fabricated the molds with a commercial resin (Detax Medicalprint Clear, 385 nm, Detax GmbH & Co. KG, Ettlingen, Germany) using a stereolithographic 3D printer (MiiCraft 50X, MiiCraft, Hsinchu, Taiwan). The mold was separated into top and bottom parts with a cylindrical cavity of

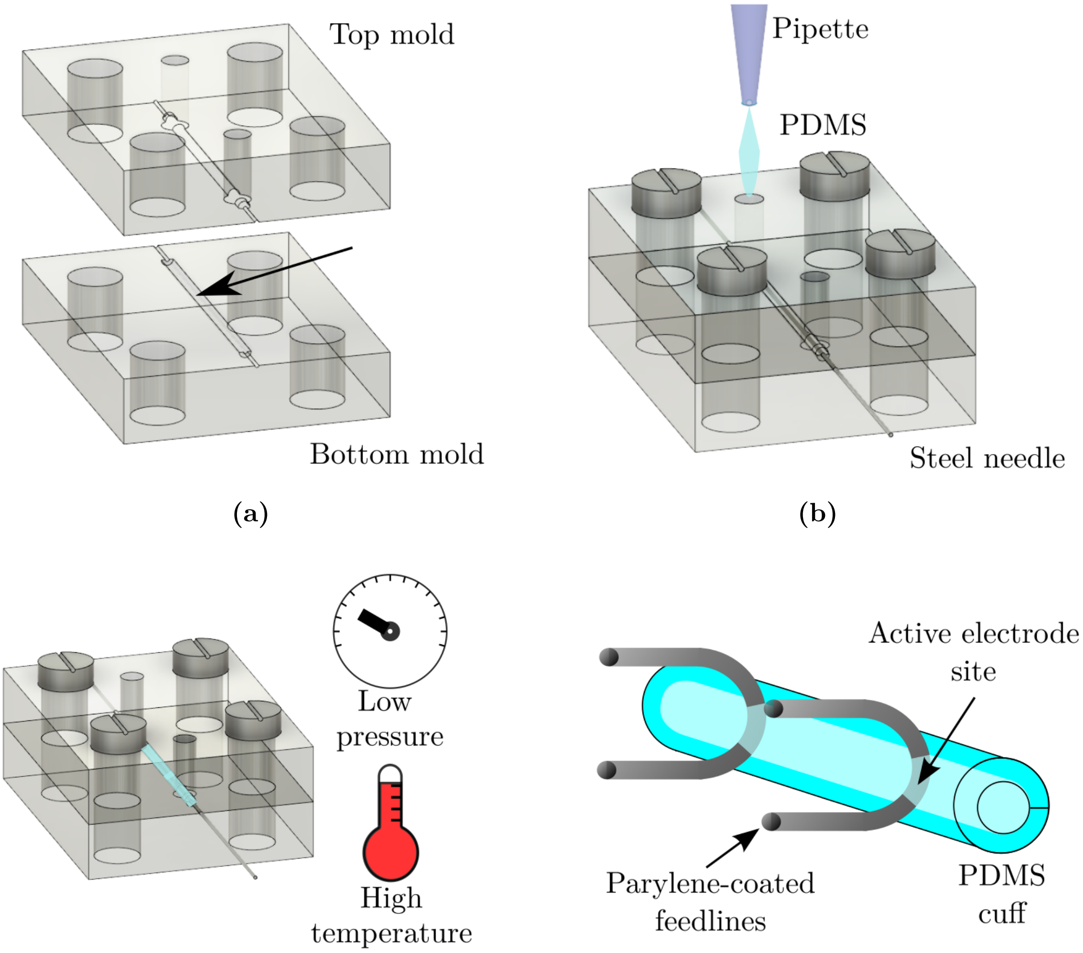
Top mold
Bottom mold
(a)
Pipette
PDMS
Steel needle
(b)
Low pressure
High temperature
(c)
Active electrode site
Parylene-coated feedlines
PDMS cuff
(d)

Figure 3.2: PDMS cuff fabrication steps. **(a)** The mold for the cuff is 3D-printed as two separated parts. After assembly, the two parts form a cavity with the desired dimension of the cuff. **(b)** The molds are tightly screwed together, and a needle is placed inside the mold to form the cuff's lumen. PDMS is cast inside the resulting tube-shaped cavity. **(c)** The excess air in the PDMS is removed by degassing in a vacuum chamber and the PDMS is thermally cured. **(d)** After curing, the tube is detached from the mold and the stimulation electrodes are inserted through the PDMS tube. The cuff is then cut to a length of ~1 mm and opened along the tube to enable nerve insertion. Finally, the exterior of the electrode is coated with parylene-C.

900 µm in diameter to cast the substrate of the cuff. Two orifices were included in the top part of the mold for insertion of the cuff material and venting the air trapped

inside the cavity during the pipetting process (Figure 3.2(a)). The molds further included supporting structures to align a steel needle of 150 µm in diameter along the cylindrical cavity, which formed the lumen of the cuff. After the mold was assembled and the top and bottom parts were screwed together, the cuff material was pipetted into the cavity with the needle in its center (Figure 3.2(b)). Silicone elastomer, polydimethylsiloxane (PDMS, Sylgard 184, Dow Chemical, Midland, USA) at a 5:1 base-to-catalyzer ratio was used as cuff material to provide sufficient stiffness for withstanding the latter insertion procedure with the nerve. We placed the mold with the uncured PDMS into a low-pressure chamber overnight to remove the trapped air and avoid the formation of bubbles in the PDMS. Subsequently, we cured the PDMS in an oven at 80 °C for around 8 h (Figure 3.2(c)). After curing, we detached the PDMS tube from the mold and removed the needle. Two silver wires (127 µm in diameter) were inserted through the tube so that the wire would only tangentially touch the inner wall of the tube (Figure 3.2(d)). The wires were separated by ~500 µm from each other. Finally, the cuff was cut to a length of 1 mm and opened along the side of the tube to provide access for the nerve insertion. We coated the electrode with a 3-µm-thick layer of parylene-C to passivate the exposed wire outside of the cuff using a chemical vapor deposition system (Plasma Parylene Systems GmbH, Rosenheim, Germany). Inside the deposition system, dichloro-di(p-xylylene) (Daisan Kasei, Japan) was first vaporized at 150 °C and then pyrolyzed at 740 °C to generate chloro-p-xylylene monomer. The monomer was then deposited at room temperature. Finally, we manually removed any traces of parylene insulation from the active electrode sites inside the cuff.

3.3.3 Electrochemical characterization of the electrodes

We performed chronoamperometry (CA) and impedance spectroscopy (EIS) to characterize the electrodes inside the nerve cuff using a two-electrode configuration vs. open circuit potential (OCP) (PalmSens4, Palmsens, Houten, The Netherlands). Both measurements were done in locust's saline solution ($147\,\mathrm{mmol\,dm^{-3}}$ NaCl, $10\,\mathrm{mmol\,dm^{-3}}$ KCl, $4\,\mathrm{mmol\,dm^{-3}}$ $CaCl_2$, $3\,\mathrm{mmol\,dm^{-3}}$ NaOH, and $10\,\mathrm{mmol\,dm^{-3}}$ HEPES buffer, Sigma Aldrich, St. Louis, USA) [118]. One electrode was set as the working electrode and the other was set as the combined reference and counter electrode. Voltage steps of 50 mV, 1 V and 3 V were applied in the CA measurement, after a stabilization period of 1 s to OCP. The EIS measurement was performed between 5 Hz and 500 kHz, with a sinusoidal signal of 10 mV of amplitude. Cyclic voltammetry scans were applied between -1 and 1 V at $10\,\mathrm{mV\,s^{-1}}$ for 10 cycles to precondition the surface of the electrodes before each CA and EIS measurement.

3.3.4 Surgery and nerve interfacing

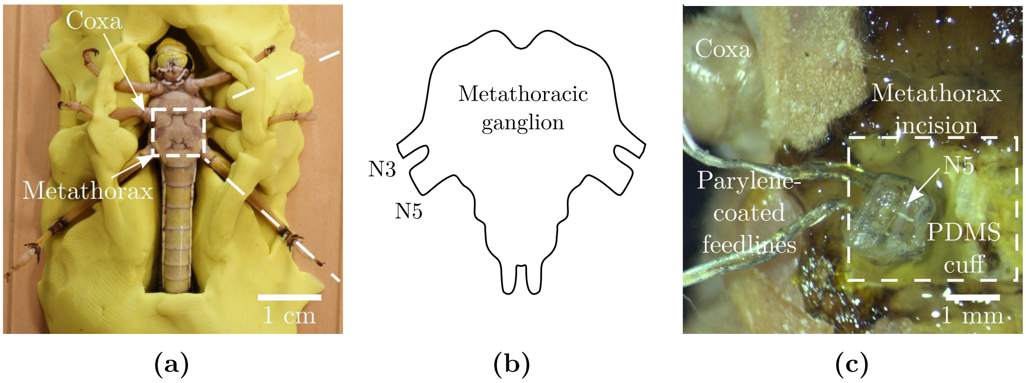

Figure 3.3: (a) *Locusta migratoria* prior to the surgery in clay bed. (b) Scheme of the metathoracic ganglion and the nerves innervating the hind leg. (c) Microscope image of the surgical incision on the metathorax of the locust, showcasing the N5 immediately before insertion in the cuff electrode.

We chose the insect *Locusta migratoria* for the experiments because it has a relatively simple nervous system and opted for the tibiofemoral angle of the hind leg as biomarker. The experimental unit consisted of an adult female. We controlled the angle by stimulating the fast extensor tibiae motoneuron (FETi). This neuron has its soma and dendritic branches in the metathoracic ganglion and projects its axon into the nerve 5 (N5). Prior to the surgery, we anesthetized the locust by chilling it to 2 °C for around 30 min. Then, we placed it in a holder made of modelling clay with the ventral side facing upward, as shown in Figure 3.3(a). For the surgery, we removed the cuticle of the metathorax and carefully cut the muscles attached to it, to expose the metathoracic ganglion (Figure 3.3(b)). Next, we removed the air sacs and the trachea to reveal the desired nerve, which innervates the metathoracic legs. With the aid of a micromanipulator, we slid N5 into the cuff electrode (Figure 3.3(c)). The electrodes were used to stimulate the FETi by delivering the appropriate pulses at a frequency determined by the controller. Finally, we connected the electronic setup and recorded the set point, the error signal, and the pulse train using an oscilloscope (InfiniiVision DSOX2024A, Keysight, Santa Rosa, USA). As angle set points we applied step and ramp functions to characterize the response of the locust movement to different stimuli conditions. In addition, we captured the displacement of the leg on video and extracted the extension angle using image processing (MATLAB R2020b, Mathworks). To this end, the algorithm determined the geometric center of the leg for each frame and calculated the angle via the difference between the center points of each frame and the center point of the first frame, with the tibiofemoral joint as the origin.

3.4 Results and discussion

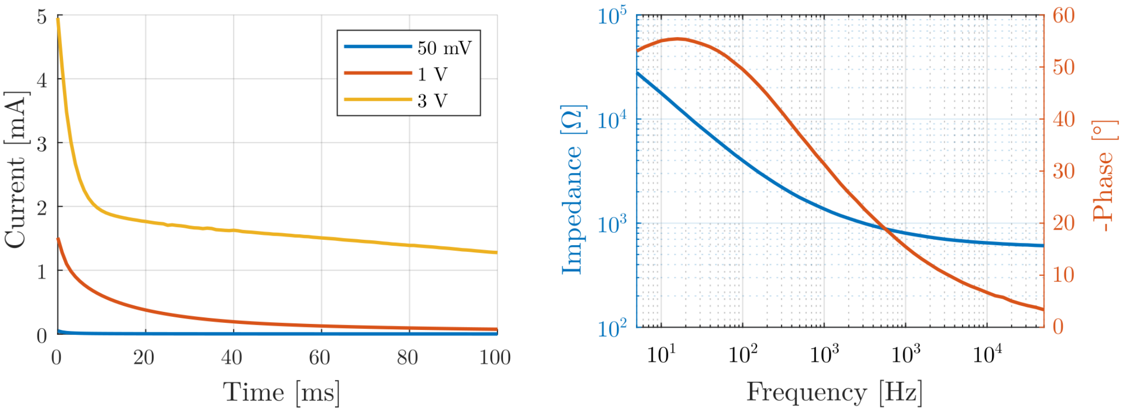

(a) **(b)**

Figure 3.4: Electrochemical characterization of the custom-made cuff electrodes in saline solution. The characterization was performed in a bipolar configuration between the two stimulation electrodes in the cuff. **(a)** Chronoamperogram for three different voltage step amplitudes. **(b)** Impedance spectroscopy analysis exhibiting a combined impedance of ~1.4 kΩ @ 1 kHz.

3.4.1 Electrode characterization

We characterized the electrodes before their implantation using chronoamperometry and impedance spectroscopy. Figure 3.4(a) shows the results of chronoamperometry applying voltage steps ranging from 50 mV to 3 V. As expected, the current response scales with the amplitude. For a voltage step of 50 mV we observe a capacitive spike in the range of tenths of µA. Afterward, the current quickly decays to 0 µA due to the negligible impact of Faradaic contributions at such a low voltage. For higher voltages we observe a more pronounced contribution of the Faradaic current. At a voltage step of 3 V, the capacitively induced exponential current decay is only dominant during the first 10 ms. Afterwards we observe a slower decay, which is likely caused by effects of diffusive mass transport limiting the Faradaic current.

To minimize possible aversive effects due to the presence of Faradaic reactions, we fixed the pulse width to 100 µs, where the capacitive contribution to the current is dominant. Reducing Faradaic reaction in in vivo implementations is important, as both DC currents and the species produced electrochemically at the electrode can damage the nerve tissue [119]. The EIS results are shown in Figure 3.4(b), showcasing an absolute impedance of both electrode–electrolyte interfaces in series around 1.4 kΩ at 1 kHz.

3.4.2 Control strategy

Figure 3.5(a) shows the results for the 10 trials of the voltage step stimulation and Figure 3.5(b) for the 5 trials of the voltage ramp stimulation. The set point signal for Figure 3.5(a) was given by a ~2 V step function. As a guiding value, we related this voltage level to an angle of 75°, estimated from the mean angle in the experimental results. The change in the set point produced an error signal that was encoded into a stimulation rate via the microcontroller. The limb reacted to the change of stimulation rate and produced an extension of the locust's leg captured by video recordings. The mechanical response was additionally sensed by the flexible resistor, increasing the feedback and decreasing the error signal. As expected, this led to an initial error maximum, due to the inertia of the leg movement. This abrupt transient can be mitigated by the incorporation of a derivative factor in the control loop. Additionally, the steady-state error can be eliminated by the incorporation of an integrative factor. The delay between successive stimulation pulses is maximum when the error signal is minimum and decreases abruptly at the step onset instant. In addition to the step response, we analyzed the closed-loop stimulation of the locust's leg to a continuously varying control signal in form of a cyclic ramp. The signals for the ramp stimuli are presented in Figure 3.5(b) (shown as 5 traces of 2 ramp cycles). The individual signals were obtained as previously described for the step response. As we can see in Figure 3.5(b), the locust's leg followed the ramp control signal repetitively. Interestingly, an asymmetry between extension and flexion of the leg was observed in the experiment. The extension followed the control signal with a steeper response. Furthermore, an oscillation was evident at low angles (flexion state). These results can be explained by the chosen configuration for rate-based stimulation of the extensor nerve. At very low frequencies, we observe the response to individual pulses, which deviate the leg from the flexion state, which is not directly controlled by stimulation in our experiments. Furthermore, the flexion of the leg and return to resting position is determined by the tendon of the tibiofemoral joint and the intrinsic neural activity and reflexes of the locust. To achieve more precise control of the leg position, both the flexor and extensor nerve should be controlled independently and the natural feedback mechanisms suppressed.

We analyzed the correlation between the frequency (computed as the inverse of the inter-pulse delay) and the angle of the leg for the voltage ramp experiment. Figure 3.6 shows the scattering of the angles corresponding to different frequencies. Two linear clusters can be identified, one corresponding to the flexion and the other to the extension of the leg. The separation of the same trajectory in two different clusters might be explained by feedback signals on the flexor nerve, which possibly depend on the previous state. The results demonstrate that it is possible to control

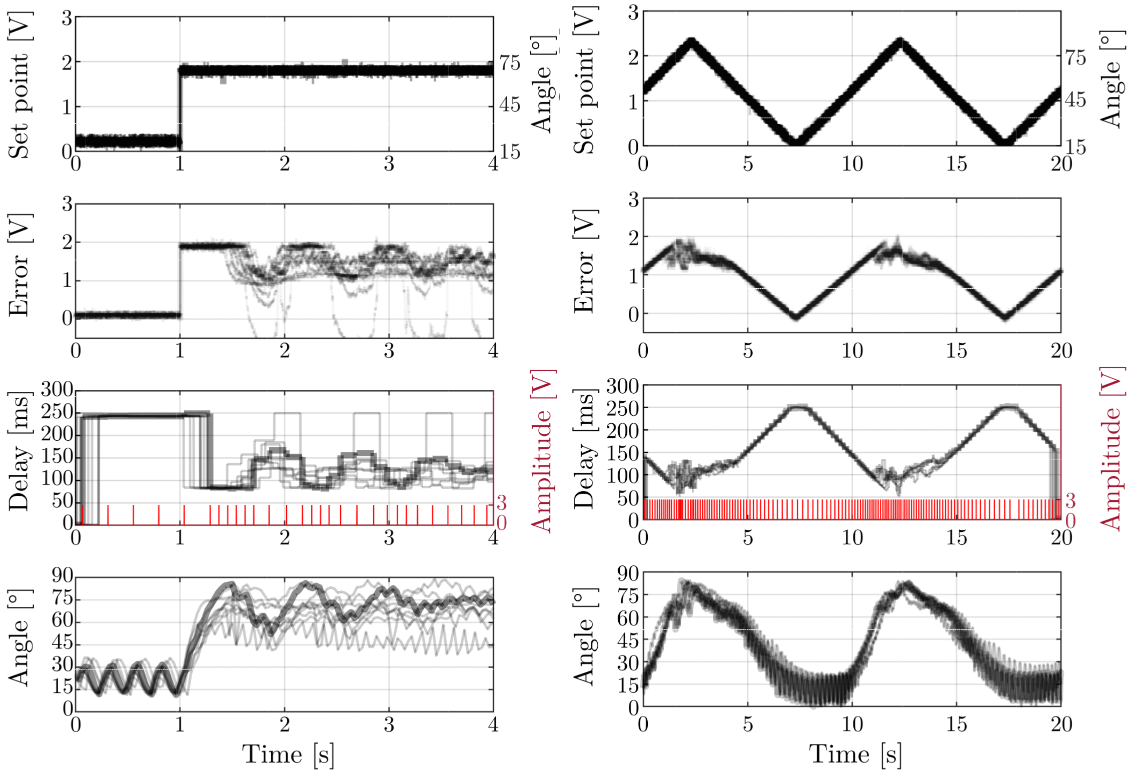

(a) (b)

Figure 3.5: A set point voltage is applied to determine the desired angle of the leg. The error between set point and feedback signals is converted into a stimulation pulse pattern (red), and a corresponding inter-pulse delay. The stimulation pattern triggers a response in the leg angle, which is extracted from video recordings. In **(a)** the black traces show 10 repetitions of the same experiment, whereas in **(b)** they show 5 repetitions of the same experiment. The thicker black traces correspond to the indicated pulse pattern.

the angle of a locust's hind leg using a simple, closed-loop stimulation strategy. In particular, the control was achieved using short voltage pulses and varying the delay between them. Fast pulse-generation devices can be implemented using simple commercial microcontrollers, which offer configurable outputs for multisite stimulation and are easily accessible. Furthermore, fast pulses are advantageous because they allow a large proportion of the current to be capacitive instead of faradic, thus decreasing the occurrence of redox reactions, which could be harmful to the surrounding tissue [120].

Multiple aspects could be advanced to improve the precision of this intervention in future implementations. Most importantly, a single stimulation site and a simple proportional control strategy limit the degree of precision that can be achieved. Consequently, multisite selective stimulation of a single nerve or coordinated stimulation of different nerves is paramount for precise control using this concept [121, 122]. Another important factor for reliable control is the transducer. In this work, we opted for an ink-based flexible resistor, because we wanted to minimize the mechanical load on the leg. However, the nonlinear response of the chosen transducer influences the control strategy. Other angle transducers, such as potentiometers, could represent a very high mechanical load for the leg of the locust, thus interfering with the free movement. A low-friction rotary encoder with an analog-voltage output or more advanced thin-film flexible resistors could be the best compromise between precision and mechanical load. Finally, while a proportional control strategy sufficed for our purposes, more complex strategies would bring additional benefits, such as the absolute elimination of the error signal with the addition of an integrative factor in the control loop. The demonstrated concept of controlling a variable in a non-fully characterized system might be applied to other systems such as the degradation of fat into heat by stimulating nerves innervating adipose tissue and monitoring its temperature as control parameter.

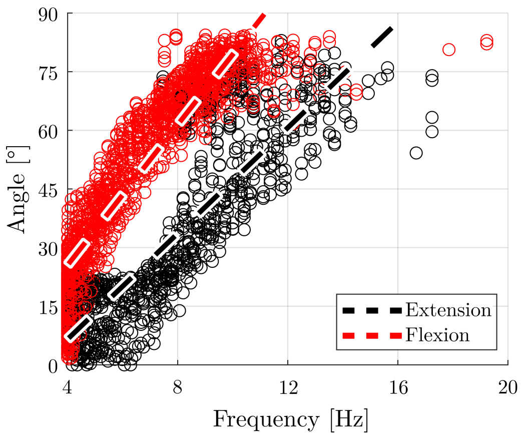

Figure 3.6: Scatter plot of the angle of the leg versus the frequency of stimulation, computed as the inverse of the inter-pulse delay, for the voltage ramp experiment. The upper cluster (red) represents the trajectory of flexion of the leg, whereas the lower cluster (black) represents the trajectory of extension of the leg. The linear fits are computed using the method of least-squares.

3.5 Conclusions

In this chapter, I demonstrated a closed-loop stimulation system to control the angle of extension of a locust's leg in real time by stimulating its extensor nerve with custom cuff electrodes. The system is implemented by a microcontroller that generates a rate-coded stimulation signal, and a flexible resistor provides the feedback signal. The results show that the average leg angle can be controlled using a time-dependent input and a stimulation signal between approximately 4 and 20 Hz. However, the presented model remains simple and limited for stimulation as it only comprises two electrodes. In the following chapters, I evaluate more complex devices, novel fabrication techniques and their performance for stimulating and recording.

CHAPTER 4

3D-printed nerve cuffs

The chapter was reproduced in part with permission from Francisco Zurita, Leroy Grob, Amelie Erben, Fulvia Del Duca, Hauke Clausen-Schaumann, Stefanie Sudhop, Oliver Hayden and Bernhard Wolfrum. I was responsible for the design of the electrodes, in vivo experiments and data analysis. The original publication "F. Zurita et al., Fully 3D-Printed Cuff Electrode for Small Nerve Interfacing. *Adv. Mater. Technol.* **2022**, 2200989. https://doi.org/10.1002/admt.202200989." is available on `https://onlinelibrary.wiley.com/doi/full/10.1002/admt.202200989/`, doi: 10.1002/admt.202200989.

4.1 Preamble

Interfacing with the peripheral nervous system is a powerful method for diagnosing and treating several diseases, such as drug-resistant epilepsy and depression. In most clinical applications, large nerves such as the vagus and the hypoglossal nerve are targeted. Large nerves carry multiple nerve fibers, and maintaining selectivity of a specific target response demands complex stimulation strategies. As the large trunks bifurcate toward their distal ends, their diameter and number of comprised fibers reduce. Consequently, interfacing small nerves can provide increased fiber selectivity. However, their small size presents challenges to the fabrication and implantation of suitable electrodes due to their fragility and constrained environments. Here, a cuff electrode that combines two-photon stereolithography and 3D inkjet printing techniques for the selective interfacing of small nerves in vivo is introduced. The device is easy to implant, and its size can be tailored for specific nerve dimensions. Its capability to record and selectively stimulate is demonstrated by targeting a locust's hind leg nerve.

4.2 Introduction

As stated previously, nerves comprise multiple axons, which makes selective interfacing challenging. Invasive intra-neural interfacing methods achieve a higher selectivity by placing the electrodes inside the nerve [52, 123, 124]. However, such invasiveness can lead to foreign body reactions, which are problematic for long-term implantations [125]. Extraneural electrodes, such as the one presented in the previous chapter, interface with the nerves without penetrating them but have a reduced spatial resolution, as they are only in contact with the surface of the nerve [126, 127]. This limitation is especially critical for the most widespread applications of PNI, such as healthcare and movement restoration, which commonly target the larger nerves of the body that comprise multiple nerve fibers, and their stimulation often elicits undesired side effects [128]. Different approaches and techniques have been developed to increase fiber selectivity during nerve stimulation [129]. Increasing the number of electrode sites is a common strategy to partially overcome these limitations [30].

A complementary method to increase selectivity and limit undesired side effects is to interface smaller nerves comprising fewer axons. While the custom-made cuff electrode approach presented in the previous chapter was simple and successful, the final size of the electrode was much larger than the interfaced nerve. Furthermore, it featured only two active sites, which are suboptimal for selective interfacing. As small nerves in humans can scale down to double-digit micrometers, materials and techniques used to fabricate electrodes have to be refined in size, flexibility, and stiffness to ensure the vitality of these delicate structures during interfacing [28, 129]. Commercially available cuff electrodes can interface with small nerves in the range of 100 µm in diameter and below (e.g., CorTec GmbH, Freiburg, Germany, MicroProbes, Gaithersburg, MD, USA). However, the overall dimension of these devices is usually much larger due to fabrication constraints (around 10× for inner diameters of 100 µm), which often proves inconvenient for implantation due to space restrictions. In addition to size, the difficulty of interfacing is a common practical limitation. Most cuff electrodes require buckling or stitching the structure around the nerve, which often demands a high degree of skill from the practitioner.

The fabrication of suitable cuff electrodes has been enhanced in the last years with the incorporation of additive manufacturing technologies to rapidly prototype cost-effective novel devices and sensors. As a result, 3D-printed microscale devices have been fabricated for electrical stimulation [130]. In particular, two-photon stereolithography (TPS) is one of the few techniques that is capable of fabricating free-form structures at sub-micron accuracy [131, 132]. Previous studies on TPS-fabricated devices for electrical stimulation include alignment tools to assemble carbon fiber electrodes, microscaffolds for drug loading accompanying flexible electrode arrays for cochlear insertions, free-standing microelectrodes with carbon electro-active surfaces, as well as electrode-laden nanoclips capable of interfacing with nerves $> 50\,\mu\text{m}$ in diameter [27, 133–136]. These studies have achieved the measurements of spontaneous multiunit activity, stimulation-evoked compound responses, auditory brain stem responses, in vivo dopamine response, and nerve activity [137].

This chapter proposes an additively manufactured, multichannel cuff electrode for interfacing with micrometer-sized nerves that can stimulate and record neural activity. We combine inkjet-printed 3D microelectrodes and TPS-printed 3D cuffs to produce the interfacing devices. Our 3D microelectrodes function as active sites, while 3D-printed cuffs provide mechanical attachment to small nerves. In contrast to previous devices that combine photolithographic methods with TPS, inkjet printing permits rapid prototyping of 3D electrodes by reducing the number of fabrication steps and the lack of need for a cleanroom. Additionally, we show the stimulation and recording capabilities of the proposed electrode in a locust model. This multisite design can evoke different neural responses when used with the appropriate stimulation patterns.

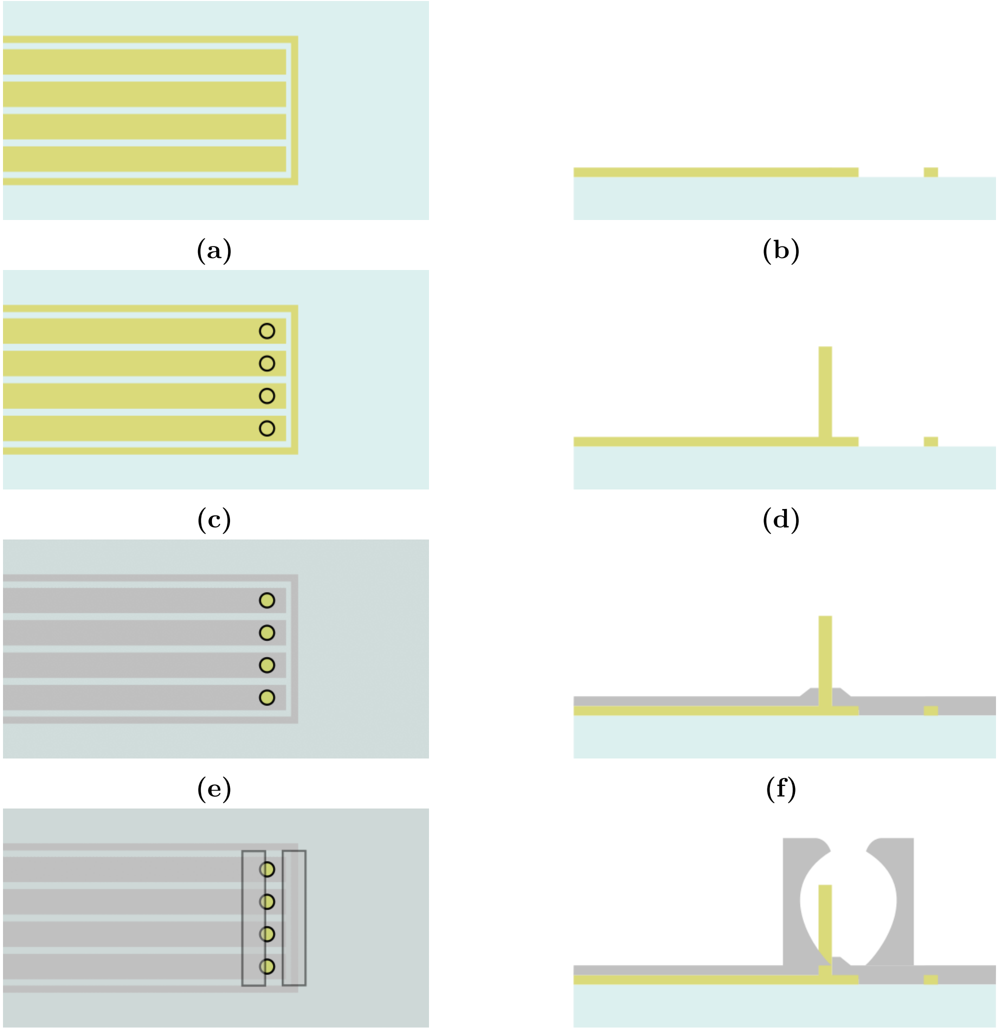

(a) **(b)**

(c) **(d)**

(e) **(f)**

(g) **(h)**

Figure 4.1: Electrode fabrication process of the proposed cuff electrode. **(a)**, **(b)** Printing of the feedline connectors. **(c)**, **(d)** Printing of the 3D microelectrodes via successive deposition of Ag nanoparticle ink droplets on top of each other. **(e)**, **(f)** Deposition of the insulation layer covering the feedlines. **(g)**, **(h)** Fabrication of the 3D nerve cuff via two-photon stereolithography.

4.3 Materials and methods

4.3.1 Inkjet-printed 3D microelectrode arrays

3D microelectrodes were printed on a 50-µm-thick polyethylene naphthalate (PEN) film (Teonex Q65HA, DuPont Teijin Films, Wilton, UK), using a silver nanoparticle ink (Silverjet DGP 40LT-15C, Sigma-Aldrich, St. Louis, MO, USA) with an inkjet printer (CeraPrinter F-Series, Ceradrop, Limoges, France). Before printing, room temperature Ag nanoparticle ink was sonicated (Bransonic ultrasonic cleaner 5510E-MTH, Branson ultrasonics, Danbury, CT, USA) for 20 min, filtered using a poly(vinylidene fluoride) filter (GD/X, Whatman, Maidstone, UK; pore size: 0.2 µm), and filled into a disposable 1 pL cartridge (DMC-11601, Fujifilm Dimatix, Santa Clara, CA, USA). The waveform applied to the piezoelectric actuator has been previously described [138]. The sample stage and the nozzle plate were held at 60 and 55 °C, respectively. The feedlines for the 3D microelectrodes were printed with an ejection frequency of 1 kHz, a drop spacing of 40 µm, and an individual Ag nanoparticle droplet diameter of ~60 µm on the PEN film (Figure 4.1(a), Figure 4.1(b)). 1000 droplets of Ag nanoparticle ink (~250 µm height) were used to form the 3D microelectrodes using a moving printed head (continuous printing method), with a drop-to-drop time interval of 3.75 s (Figure 4.1(c), Figure 4.1(d)). Once printed, the Ag nanoparticle ink was dried on the sample stage and thermally sintered in a preheated oven at 220 °C for 2 h. In order to not induce thermal stress, the sides of the PEN foil were taped (Kapton tape, VWR, Darmstadt, Germany) to a glass petri dish and slowly cooled down to room temperature after sintering for 2 h.

4.3.2 Printing the passivation

After sintering the 3D microelectrodes, an ultraviolet (UV) curable acrylate ink (PA-1210-004, JNC Corporation, Tokyo, Japan) was used to passivate the feedlines whilst allowing the 3D microelectrodes to protrude through the insulation layer (Figure 4.1(e), Figure 4.1(f)). Before printing, the UV curable acrylate ink was filtered through a 0.22 µm polyethersulfone (PES) filter (TPP, Trasadingen, Switzerland), loaded into a 1 pL cartridge (DMC-11601, Fujifilm Dimatix, Santa Clara, CA, USA) and covered with Al foil to protect the ink against light. Individual sensors were placed and held on the printer's substrate holder. In the print layout, a 20 µm spacing around the 3D electrodes was defined to ensure that the electrode structures were not covered in passivation ink. A single nozzle was used with the same waveform previously applied for the Ag nanoparticle ink during the print. The single nozzle was manually aligned with the 3D microelectrodes using the printer's on-board camera. A two-step passivation process was established without any O_2 plasma activation using a heated nozzle plate (40 °C) and sample stage (50 °C). The first layer comprised of individual droplets of cured acrylate ink (diameter ~50 µm) spaced evenly with a pitch of 100 µm. Thereafter, a layer of acrylate ink was printed with an ejection frequency of 1 kHz and a drop spacing of 32.5 µm. Lastly, the ink was cured using an inbuilt UV lamp with an approximate dose of $1\,\mathrm{J\,cm^{-2}}$.

4.3.3 Two-photon stereolithographic cuff printing and laser cutting

All cuffs were designed with Fusion 360 (Autodesk, 2020), exported as STL files, and converted to print job instructions using Describe. The inkjet-printed 3D microelectrodes were aligned and selectively exposed with an erbium-doped femtosecond laser source (center wavelength 780 nm) using Nanoscribe GT Photonics Professional operating in dip-in mode (Figure 4.1(g), Figure 4.1(h)). Power amounted to 150 mW using a 25× (NA 0.8) objective. Cuffs were printed using IP-S resin (all Nanoscribe GmbH, Karlsruhe, Germany). After printing with the two-photon stereolithographic printer, a 3-axis UV laser marker (MD-U1000C, Keyence, Osaka, Japan) was used to cut the cuff sensor along the already predefined silver outlines. The laser was set to 1.5 kW, with a shutter frequency of 100 kHz, and writing at a speed of $100\,\mathrm{mm\,s^{-1}}$. The outline was etched with the laser for a total of 100 repetitions. The substrate was aligned and focused using the on-board Keyence software.

4.3.4 Electrochemical characterization of cuff sensors

Electrochemical impedance spectroscopy was performed to characterize the 3D microelectrodes using a potentiostat (VSP-300, Bio-Logic Science Instruments, Seyssinet-Pariset, France). Locust's saline solution ($147\,\mathrm{mmol\,dm^{-3}}$ NaCl, $10\,\mathrm{mmol\,dm^{-3}}$ KCl, $4\,\mathrm{mmol\,dm^{-3}}$ $CaCl_2$, $3\,\mathrm{mmol\,dm^{-3}}$ NaOH, and $10\,\mathrm{mmol\,dm^{-3}}$ HEPES buffer, Sigma Aldrich, St. Louis, USA) was used as the electrolyte [118]. The measurements were carried out in a two-electrode setup. The individual 3D microelectrodes were set as the working electrode, and either a Pt mesh or another 3D microelectrode was used as a combined counter and reference electrode. No bias voltage was applied against the open circuit potential (E_{oc}) during the experiments. A sinusoidal waveform with an amplitude of 10 mV vs E_{oc} was applied to measure the impedance of the electrodes over a frequency range of 10^0–10^5 Hz.

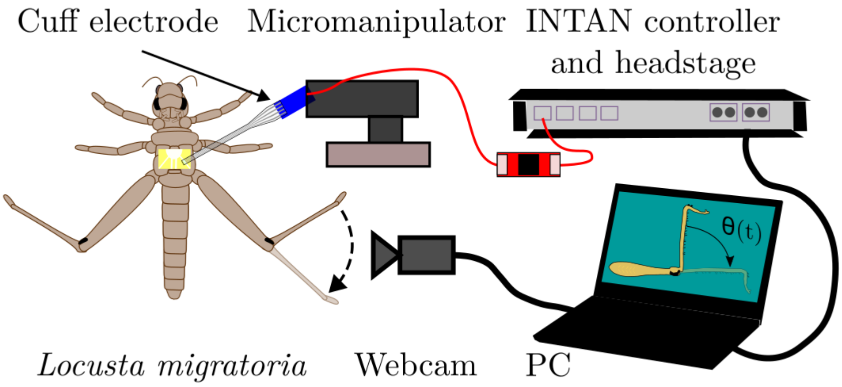

Figure 4.2: Experimental setup used to record the movement of the leg during stimulation. The subject *Locusta migratoria* was placed ventral face up. The N5 was exposed and interfaced with the cuff electrodes using a micromanipulator. The electrode was interfaced to an INTAN headstage, connected to an INTAN controller, which in turn was connected to a PC. A camera, connected to the same PC, was used to record the leg movement, and extract the tibiofemoral angle $\theta(t)$.

4.3.5 Nerve interfacing

Adult male and female locusts (*Locusta migratoria*) were used for the in vivo experiments. Since the study was conducted exclusively with locusts (insects), no special permission is required in Germany. All experiments comply with the German laws for animal welfare ("Deutsches Tierschutzgesetz"). Before the surgery, the locusts were anesthetized by cooling them down to ~2 °C for 30 min. Afterward, they were placed ventral side up on a modeling clay bed under a microscope. The cuticle of the metathorax and the air sacs below it were removed to expose the metathoracic ganglion and the N5, a nerve comprising the fibers responsible for the fast extension of the hind tibia. Then, locust's saline solution was applied to the thoracic cavity to prevent the nervous tissue from drying during the procedure. Next, with the aid of micromanipulators, the cuff electrode was approached, and the nerve was inserted into it. The contact pads of the electrodes were interfaced to a

4-pin zero insertion force (ZIF) connector (Würth Elektronik GmbH & Co. KG, Germany). This connector bridged the electrodes to an INTAN RHX control system, using the RHS2116 headset (INTAN Technologies, USA) to stimulate and record activity from the nerve. A schematic of the experimental setup is shown in Figure 4.2.

The first stimulation protocol consisted of trains of charge-balanced biphasic current pulses of 1 kHz, with an amplitude of 60 µA and a duration of 500 µs per phase. Opposite current pulses were applied simultaneously to two microelectrodes every 1 s, and the number of pulses per train was increased from 5 to 20 in steps of 5. For this protocol, the stimuli were driven between every combination of two individual electrodes, one with a leading cathodic phase and the other with a leading anodic phase. The second stimulation protocol consisted of 1 kHz trains of biphasic current pulses with an amplitude of 30 µA (all other parameters stayed the same). The stimuli were driven between every combination of two pairs of electrodes, one pair with a leading cathodic phase and the other pair with a leading anodic phase. In both protocols, the total stimulation current is preserved (i.e., 1 electrode with 60 µA or 2 electrodes with 30 µA at each phase), and the magnitude of the current per phase, cathodic and anodic, was equal at any given time, to drain all the current that was sourced. The elicited movement of the leg for both protocols was recorded on camera, and the tibiofemoral joint angle was estimated using MATLAB (MATLAB 2020b, MathWorks, USA).

Finally, neural activity of the N5 was recorded from all channels at 30 ksps. The recording setup consisted of the microelectrodes interfacing the nerve on one side of the metathorax and a Ag/AgCl electrode set as the reference electrode positioned in the abdomen of the subject. To elicit neural activity, two insect pins were inserted at the distal end of the femur separated ~1 mm from each other, and delivered a ~6 ms, 2 V pulse between them every 2 s. The acquired signals were subsequently processed using MATLAB. A second-order high-pass Butterworth filter with a cutoff frequency of 100 Hz was applied in the forward and backward direction, to remove low-frequency noise without phase distortion.

4.4 Results and discussion

Peripheral nerve interfacing is often performed in large nerves in mammals, such as the sciatic nerve of rats (Ø ~1 mm). However, small-nerve interfacing requires the implementation of an equally small interfacing electrode, which presents two challenges: the fabrication of the small electrode and a delicate interfacing procedure. Therefore, we developed a small cuff electrode with a straightforward interfacing mechanism, depicted conceptually in Figure 4.3(a). With this design, the interfacing is accomplished by simply sliding the nerve inside the cuff opening. Furthermore, we demonstrate the capability of our device to interface insect nerves of ~150 µm in diameter in only ~1 mm of nerve length (Figure 4.3(b)). Figure 4.3(c)-Figure 4.3(e) shows scanning electron microscope images of the cuff electrode devices, showcasing the electrodes (yellow false-colored), the 3D-printed cuff, and the cavity to insert the nerve. They present an estimated geometric surface area of ~0.02 mm^2.

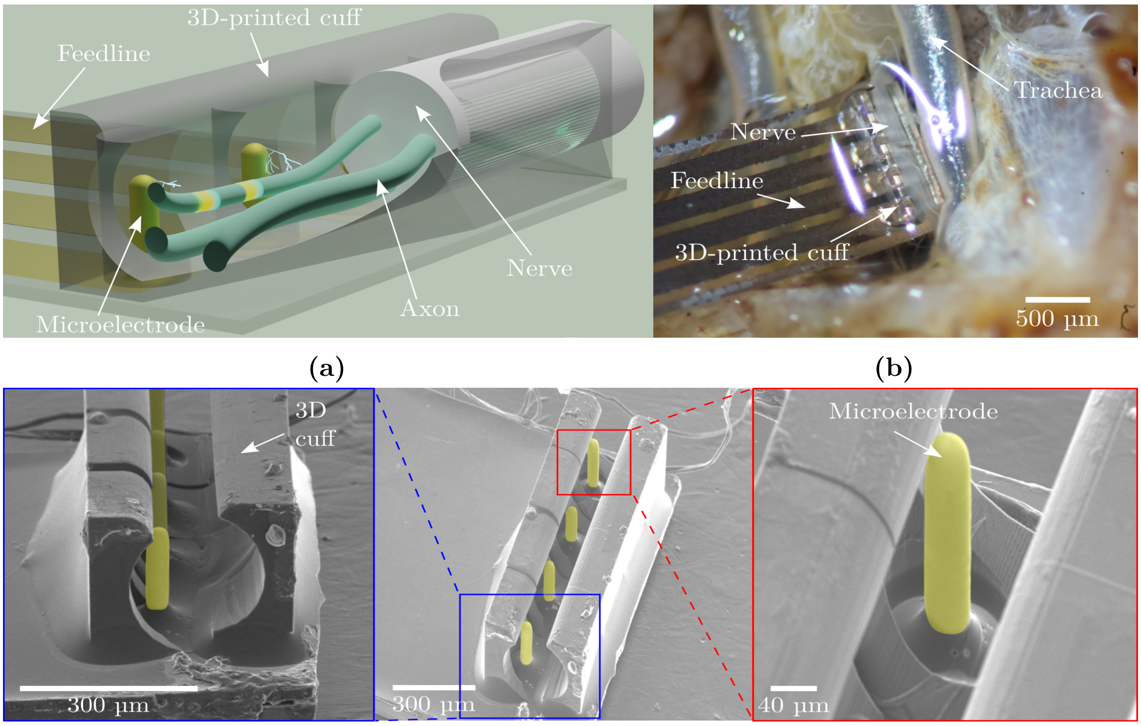
3D-printed cuff
Feedline
Nerve
Axon
Microelectrode
Trachea
Nerve
Feedline
3D-printed cuff
500 µm
3D cuff
300 µm
300 µm
Microelectrode
40 µm

(a) **(b)**

(c) **(d)** **(e)**

Figure 4.3: Nerve interfacing with the 3D-printed cuff electrode. **(a)** Concept image of a nerve with three axons, interfaced with our designed cuff electrode. The nerve is only shown along half the length of the cuff electrode for a better view of the axons and 3D microelectrodes. **(b)** Microscopy image of the cuff electrode wrapping around a nerve (N5) of a locust. **(c)**–**(e)** Tilt-corrected scanning electron microscope images of the fabricated cuff electrode. A substrate tilt of 45° **(d)**, **(e)**, and 70° **(c)** were used to image the cuff electrode. The 3D electrodes have been false-colored in yellow for clarity. All 3 images were taken using an accelerating voltage of 15 kV.

4.4.1 Electrochemical characterization of the electrodes

Impedance measurements were conducted in locust Ringer solution to investigate the electrochemical behavior of the printed electrodes for stimulation. The measurements were performed in a two-electrode configuration to characterize the impedance of the system as a whole. First, we evaluated the performance of each individual electrode against a platinum electrode serving as combined counter and

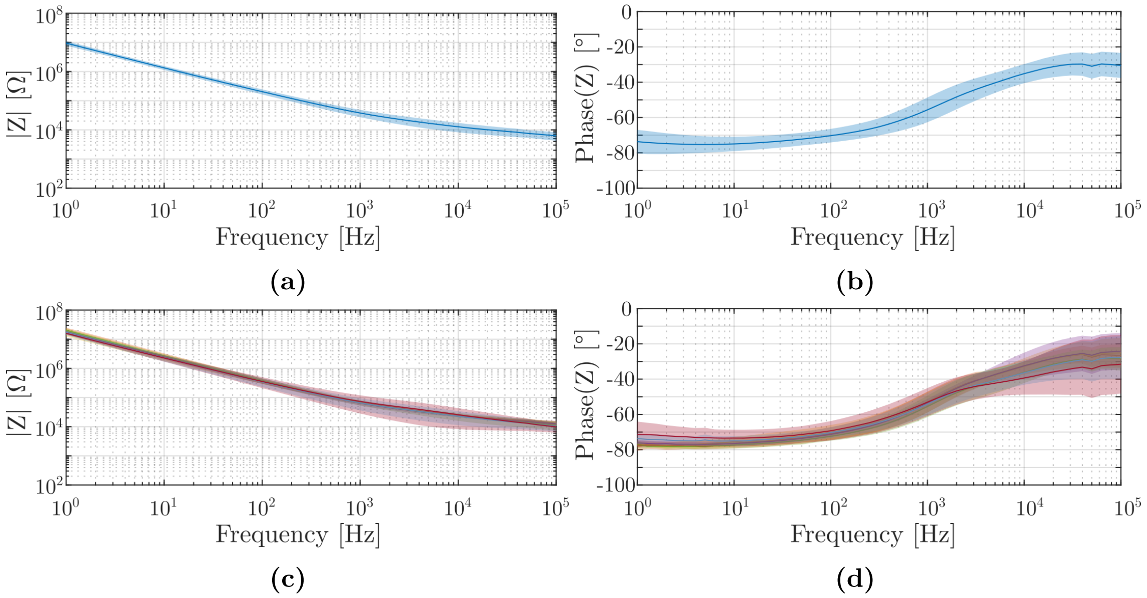

(a) (b) (c) (d)

Figure 4.4: Electrochemical impedance spectroscopy characteristics of the electrode. **(a)**,**(c)** Magnitude and **(b)**,**(d)** phase of the impedance of differently configured 3D electrodes in locust saline. Averaged impedance data between 3D electrodes and a Pt mesh in **(a)** and **(b)** (n = 16). Averaged impedance data between two 3D electrodes measured against each other in different configurations in **(c)** and **(d)** (n = 3 – 5).

reference electrode. The exposed surface of the counter electrode was several orders of magnitude larger than the actual working electrode to avoid significant voltage drops in the two-electrode configuration. Afterward, we repeated this measurement between individual electrodes, since the stimulation signal is applied in this configuration. Figure 4.4(a), Figure 4.4(b) shows the impedance between each individual 3D electrode and a combined counter and reference Pt mesh electrode, showcasing an impedance magnitude of ~30 kΩ @ 1 kHz. Figure 4.4(c), Figure 4.4(d) shows the impedance between two individual 3D electrodes, one set as the working electrode and the other as the combined counter and reference electrode. The impedance between individual electrodes increases by a factor of ~2 compared to the first setup, which is expected as the Pt mesh electrode presents a lower impedance due to its larger surface area.

4.4.2 Stimulation results

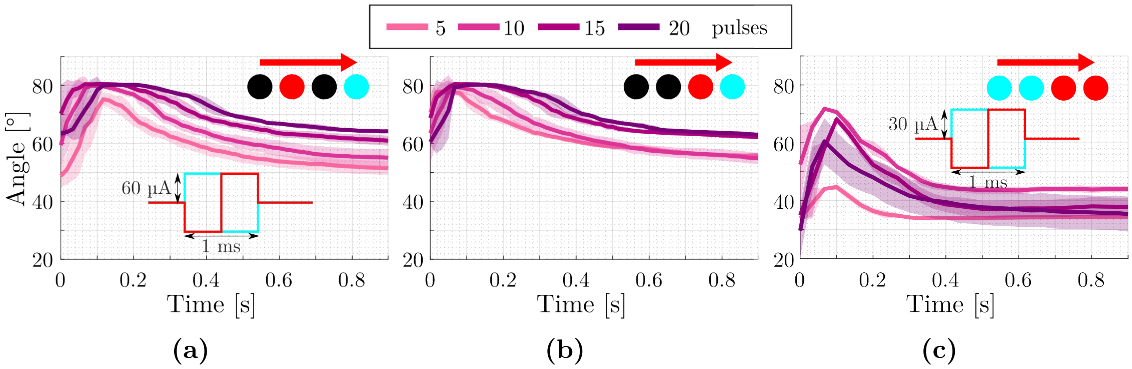

(a) **(b)** **(c)**

Figure 4.5: Tibiofemoral joint angle span elicited through electrical stimulation. Different electrode combinations were used, with a leading cathodic phase (red), a leading anodic phase (light blue), and inactive electrode (black). The red arrow indicates the proximal-to-distal direction of the nerve relative to the electrodes. The stimulation current was a sequence of bipolar pulses in succession starting at t = 0, shown in **(a)** and **(c)**. **(a)**, **(b)** The stimulus is a bipolar current pulse train of 60 µA of amplitude and 500 µs pulse duration between two individual electrodes. The number of delivered pulses ranges from 5 to 20, and each trace shows the mean and standard deviation of 20 stimulation events. **(c)** The stimulus is a bipolar current pulse train of 30 µA of amplitude and 500 µs pulse duration between two pairs of electrodes. For this last scenario, movement was elicited when both phases were on adjacent electrodes. For all other combinations of pairs of electrodes, no movement was elicited.

The N5 is a nerve that comprises fibers responsible for the fast tibiofemoral angle extension of the locust's hind leg in movements like jumping and kicking. We interfaced our cuff electrodes with this nerve to validate its stimulation capabilities. The elicited motion of the hind leg of the locust was captured on camera.

Initially, we investigated the influence of the number of stimulation pulses on the observed leg extension using only 2 out of the 4 individual electrodes to assess movement using the simplest electrode configuration. In this configuration, the biphasic stimulation threshold that needs to be delivered to perceive movement was found to be 24 µA, 500 µs phase duration, which corresponded to a light twitching movement. To reliably elicit measurable leg extension, we applied a stimulus signal using a train of 1 kHz, 60 µA biphasic pulses (3 mA mm^{-2} estimated current density). Each phase was 500 µs long, and each train comprised 5 to 20 individual pulses. The pulse trains were delivered every 1 s, at t = 0. The response to the different stimulation patterns is depicted in Figure 4.5(a) and Figure 4.5(b). The movement traces corresponding to other combinations can be found in Appendix E. Each trace exhibits the mean and standard deviation of the angle variation of the tibiofemoral joint of the leg elicited by the stimulation signal ($n_{\mathrm{repetition}} = 20$). The electrodes used are shown in red (leading cathodic phase) and light blue (leading anodic phase). The unused electrodes are shown in black. The 6 possible combinations were tested, and leg movement was elicited in all of them. While the initial angle varied within the experiment, we observed a tendency for lower maximum leg extension and faster retraction when applying only 5 pulses as opposed to higher pulse numbers. We further investigated the influence of pairing different electrodes on the elicited leg response using four stimulation electrodes simultaneously. To assess the geometric influence of the electrode configuration on the elicited movement response, always two electrodes were set on the same phase while all electrodes delivered the same stimulating current magnitude. Each electrode delivered 1 kHz, 30 µA biphasic pulses to keep the total delivered current per phase the same as in the previous experiment (1.5 mA mm^{-2} estimated current density). Figure 4.5(c) shows the result for a combination of both leading cathodic (“C”) and anodic (“A”) phases on the same end of the cuff electrode (“AACC”). A similar result was achieved by inverting the leading phases for this case (“CCAA”). However, for all other combinations of “C” and “A”, no movement was elicited. To exclude the possibility that the lack of absolute injected charge causes the absence of a response, we increased the number of pulses up to 100, to no avail. However, an increase in current amplitude to 35 µA and, therefore, an increased charge per phase, elicited leg movement again with only 5 pulses. Further increasing the current amplitude decreases the elicited angle span because the average final position of the leg approaches its full extension. This phenomenon can be attributed to the stronger depolarization caused by tetanic contraction, making the contraction last longer [139]. While both stimulation protocols (using 2 or 4 electrodes) delivered the same charge, movement could not be elicited for some combinations, suggesting that the electrode configuration influences the stimulation pattern.

4.4.3 Simulation of activating function

To investigate the influence of the electrode configuration on the activating function, we performed finite element method simulations with COMSOL Multiphysics (COMSOL AB, Stockholm, Sweden). The activating function f_x for extracellular nerve stimulation along the fiber length coordinate x is proportional to the second spatial derivative of the extracellular potential along the fiber $f_x \propto d^2V/dx^2$ [140]. Since the electric field is related to the electric potential by $\mathbf{E} = -\nabla V$, the activating function can be expressed as $f_x \propto -dE_x/dx$. In the following, we refer to the normalized activating function $f_{n,x} = -dE_x/dx$, disregarding the proportional factor because we are only interested in a comparative analysis. Given a medium with conductivity σ, the electric field $\mathbf{E}$ is related to the current density $\mathbf{j}$ following Ohm's law $\mathbf{j} = \sigma\mathbf{E}$. Therefore, the applied stimulation current modulates the electric field and, consequently, the activating function along the nerve. The microelectrodes, the 3D-printed nerve cuff, and locust saline solution were modeled using material properties of Ag ($\sigma = 6.3 \times 10^7\,\mathrm{S\,m^{-1}}$), insulating material, and PBS electrolyte solution ($\sigma = 1.52\,\mathrm{S\,m^{-1}}$), respectively. The nerve was modeled as a cylinder ($r = 80\,\mathrm{\mu m}$, $\sigma = 0.57\,\mathrm{S\,m^{-1}}$ in the direction along the axon, $0.083\,\mathrm{S\,m^{-1}}$ in the other two directions) surrounded by a nerve sheath ($d = 10\,\mathrm{\mu m}$, $\sigma = 2.1 \times 10^{-3}\,\mathrm{S\,m^{-1}}$), as shown in Figure 4.6(a) [141]. The nerve comes in contact with the electrode at a height where the horizontal (xy) plane crosses the center of the nerve. Further information on the simulation conditions can be found in Appendix F.

The longitudinal component of the electric field E_x was computed for two electrode configurations, CCAA and CACA, where again "C" stands for a cathodic stimulation pulse, and "A" for an anodic stimulation pulse. Figure 4.6(b) and Figure 4.6(c) show E_x on a plane parallel to the base of the cuff that cuts through the middle of the nerve for CCAA and CACA, respectively (top view). It can be seen that E_x reaches higher values for CCAA than for CACA, suggesting that the electrode phase influences E_x. Then, we computed E_x and the activating function along the center of the nerve for CCAA and CACA, and the results are shown in Figure 4.6(d) and Figure 4.6(e), respectively. The activating function has a higher amplitude for CCAA than for CACA, suggesting that the CCAA configuration is more likely than the CACA configuration to elicit a neural response given the same stimulation amplitude, which is in line with the observed behavior. Furthermore, the obtained activating function values for comparable injected charge are similar to those reported in the literature [142]. These results suggest that spatial selectivity is possible by modulating the stimulation current and generating the desired activating function.

4.4.4 Recording of neural activity

The N5 comprises nerve fibers that convey sensory information to the metathoracic ganglion (afferent) or motor signals from the ganglion to the leg (efferent). We elicited movement and recorded activity of the nerve on all electrodes to validate the ability of our device to detect electrophysiological signals. The average noise floor of all channels was $11.7\,\mu V_{rms}$. The acquired neural signals presented a phase delay between electrodes, only found in two combinations: from ch1 to ch4 and from ch4 to ch1 (ch1 being the most proximal electrode to the ganglion and ch4 the most distal). Since no other phase combination was found, we believe this lag can be attributed to the propagation velocity of both efferent (ch1 to ch4) and afferent (ch4 to ch1) neural signals. Figure 4.7 shows the mean and standard deviation for 50 occurrences of each signal propagation event. These results demonstrate our cuff electrode's capability to distinguish between afferent and efferent nerve fiber activity. Given the time difference between the peak of the pulses from channels 1 to 4, and knowing that the distance between them corresponds to $768\,\mu m$ by design, we estimated a mean conduction velocity of 3.47 and $0.88\,m\,s^{-1}$ standard deviation. Furthermore, the delay estimation does not distinguish between individual nerve fibers, which means that the spikes recorded could correspond to compound action potentials (CAPs). CAPs comprise multiple fibers' activity and last longer than individual action potentials, which could introduce errors when estimating the propagation velocity. Conduction velocities previously reported in the literature on motor fibers found in the crural nerve of the locust range from 1.6 to 2.3 $\mathrm{m\,s^{-1}}$ [75]. To the best of our knowledge, there are no reports on localized conduction velocity of the N5 at a close distance to the ganglion. Phase measurements could be used, for example, for the detection or evaluation of neurodegenerative diseases that affect the action potential propagation velocity along the nerve, like multiple sclerosis, or to extract features to increase the recording selectivity using neural networks [25, 143].

Although we were able to record neural activity with our device, the SNR achieved is low due to the imperfect electrical sealing of the individual electrodes [144, 145]. This incomplete sealing derives from the unsuccessful polymerization of the resin at the interface of the individual electrodes, and it occurs when the laser used for two-photon stereolithography is focused in their vicinity. This effect is most likely due to the absorption characteristics of Ag (between 350 and 500 nm) at the laser's wavelength (780 nm), which results in a reflection of the light. This reflection results in an overexposure of the resin, creating bubbles that prevent its correct polymerization. To improve the electrode sealing, a non-metallic conductor, such as PEDOT:PSS, could be used as the material for the 3D microelectrodes [146, 147]. This material would potentially improve the polymerization around the 3D microelectrodes, given its energy absorption characteristics at wavelengths above 310 nm [148]. Furthermore, a PEDOT:PSS coating would reduce the electrode voltage generated during stimulation, preventing the occurrence of undesired electrochemical reactions [149].

The importance of proper sealing for nerve interfacing becomes clear when we compare our device with standard hook electrode recordings (see Figure G.1 in Appendix G). Pulling the nerve out of the hemolymph with Ag hook electrodes, typically results in an improvement of both, stimulation and recording, due to the reduction of leakage current through the external electrolyte. However, when the hook electrodes are immersed in the electrolyte (comparable to an in vivo configuration), the stimulation and recording performance degrades drastically due to a lack of electrical insulation between the electrodes. In such a configuration, no action potentials were visible during recording with immersed hook electrodes. Similarly, in Chapter 3 we interfaced the N5 with custom Ag electrodes within a silicone cuff. While stimulation was possible with such a device, recording of activity was not successful, probably due to an insufficient sealing at the planar Ag electrode surface. In contrast to the hook electrode and planar cuff electrode, the printed 3D cuff electrode device was able to stimulate and record from the N5 when immersed in the electrolyte.

Future improvements should address concepts for fast implantation procedures without risking damage to the nerve structure as well as possibilities for long-term application. Although Ag is widely used in electrophysiological measurement, it is not recommended for long-term use, due to known biocompatibility issues. A potential improvement in this regard could be gained by electroplating the 3D electrodes with Au or Pt or conductive polymers, such as PEDOT:PSS, which has been shown to achieve low cytotoxicity and high electrochemical stability [138, 150].

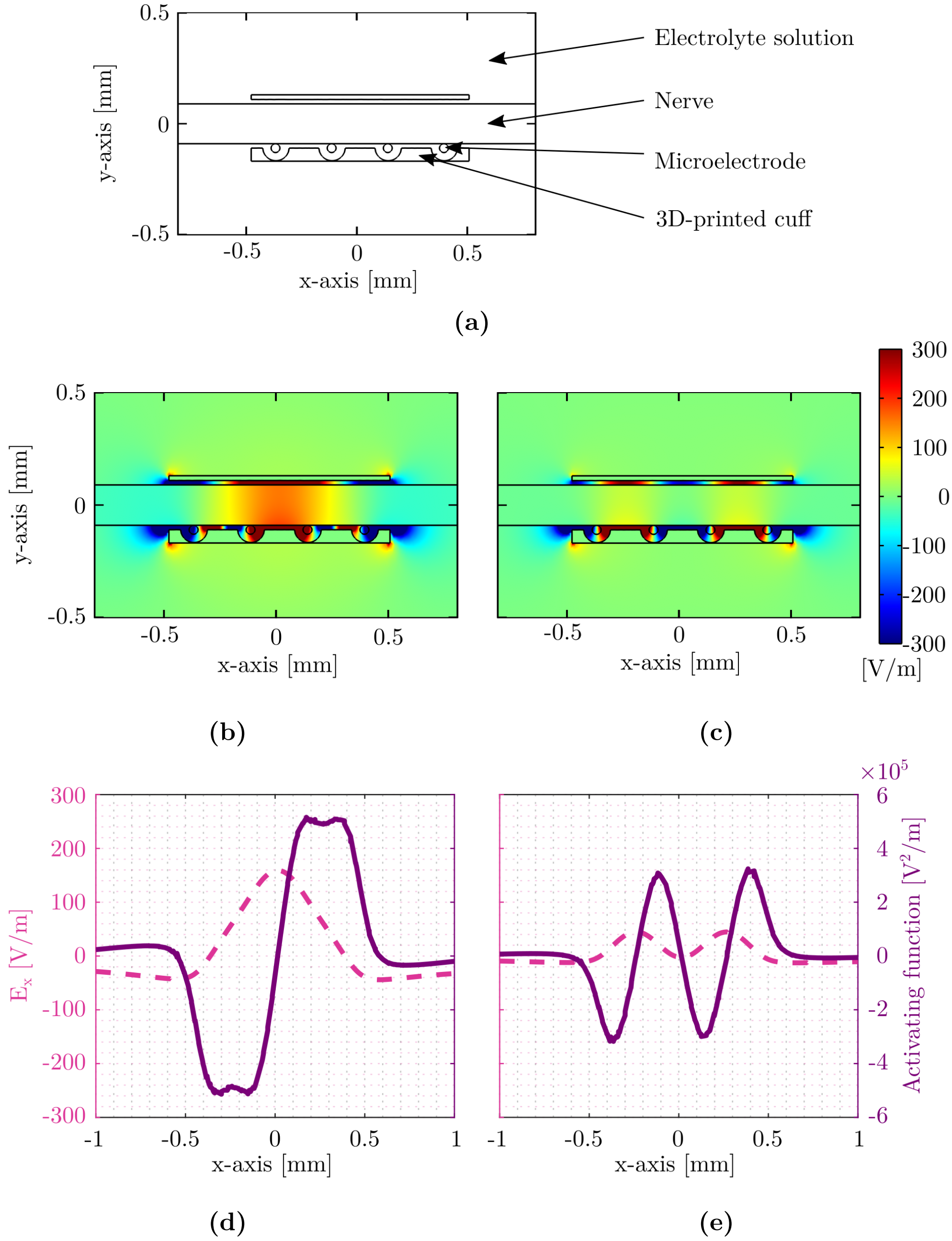

(a)

(b) (c)

(d) (e)

Figure 4.6: Finite-element-method simulations of the electric field and activating functions for two electrode configurations. **(a)** Top view of the simulated elements on a plane cutting through the middle of the nerve, perpendicularly to the microelectrodes. E_x component of the electric field for **(b)** CCAA and **(c)** CACA configurations. E_x component and activating function along the center line of the nerve (y = 0) for **(d)** CCAA and **(e)** CACA configurations.

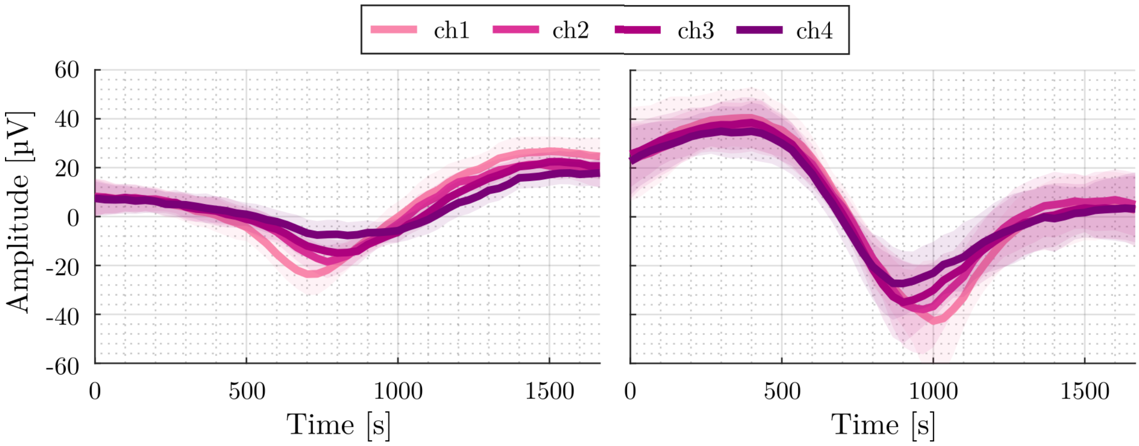

(a) **(b)**

Figure 4.7: Mean and standard deviation for 50 compound action potential events. **(a)** The phase of the channels leads in proximal (ch1) to distal (ch4) direction, hinting activity from efferent nerve fibers. **(b)** The phase of the channels leads in distal (ch4) to proximal (ch1) direction, hinting activity from afferent nerve fibers.

4.5 Conclusions

In this chapter, I presented a novel, entirely additively-manufactured, 3D cuff electrode for small nerve interfacing. The individual electrodes are made of inkjet-printed Ag, whereas the cuffing mechanism is 3D-printed around the electrodes using two-photon stereolithography, offering a straightforward mechanical attachment with the nerve. I demonstrate successful stimulation and recording of a locust nerve involved in the fast tibiofemoral joint extension. Different combinations of electrodes, stimulation amplitude, and phase can be used to elicit different movement patterns on the animal's leg. Furthermore, the device can determine the direction of propagation of neural activity along the nerve by analyzing the phase of the recorded signals. I believe this technique could be useful for the rapid development of custom-sized nerve interfaces and be applied in implantable therapies that require modulation or monitoring of nerve activity. However, Ag should be avoided for long-term use due to biocompatibility issues. Furthermore, the electrode count of the device is limited to four. In the following chapter, I will evaluate further PNI techniques that increase the number of electrodes and use more biocompatible materials, which also feature straightforward nerve attachment mechanisms.

CHAPTER 5

Further approaches to improve small nerve interfacing

The chapter was reproduced in part with permission from Lukas Hiendlmeier, Francisco Zurita, Jonas Vogel, Fulvia Del Duca, George Al Boustani, Hu Peng, Inola Kopic, Marta Nikić, Tetsuhiko Teshima, and Bernhard Wolfrum. I was responsible for electrochemical characterization of the electrodes, their in vivo implementation and the subsequent data analysis. The original publication "L. Hiendlmeier et al., 4D-Printed Soft and Stretchable Self-folding Cuff Electrodes for Small-nerve Interfacing. *Advanced Materials.* **2023** 2210206" is available on `https://doi.org/10.1002/adma.202210206`. The fabrication and electrochemical characterization of the pre-folded electrodes was reproduced in part with permission from Sebastian Freko from his Master's thesis "Development, Fabrication and Characterization of a Memory-Shaped, Parylene-Based Cuff Electrode for Peripheral Nerve Interfacing" and is presented here for completion. Part of Figure 5.4 has been shown in his thesis, as well as the data shown in Figure 5.5(a).

5.1 Preamble

Peripheral nerve interfacing (PNI) has a high clinical potential for treating various diseases, like obesity or diabetes. However, currently existing electrodes present challenges to the interfacing procedure, which limits their clinical application, in particular when targeting small peripheral nerves ($< 200\,\mu\text{m}$). To improve the electrode handling and implantation, we fabricate two nerve interfaces that can cuff around a small nerve. The first one presents a water-absorbing hydrogel that triggers a self-folding mechanism, whereas the second one is already pre-folded and the insertion is performed by lightly pulling the nerve. I demonstrate the straightforward implantation and extraction of both devices as well as their capabilities for electrical interfacing with a multi-electrode configuration.

5.2 Introduction

PNI is normally carried out on the larger nerve trunks of the body, which simplifies the electrode manufacturing and interfacing procedures. However, as stated before, larger nerve trunks comprise several nerve fibers, and their stimulation often elicits unintended neuromodulatory responses. Fiber selectivity can be improved using intraneural electrodes that pierce through the nerve tissue to come closer to the axons [52, 124, 151]. Nevertheless, this procedure causes trauma to the nerve and triggers a strong foreign body response (FBR), quickly degrading the electrodes' performance [125, 152]. This trauma can be generated either because of the stiffness of the shuttle that guides the electrode inside the nerve or because of the stiffness of the electrode itself, such as the Utah-array electrode [153–155].

The use of cuff electrodes for nerve interfacing intrinsically reduces trauma, as they do not pierce the nerve tissues. This trauma can be further mitigated via carefully selecting the fabrication materials to reduce the mechanical mismatch between the cuff and the nerve. Soft and stretchable materials, like hydrogels and silicone elastomers, are typically used for the fabrication of nerve cuffs [15, 29, 126, 156–158]. Alternatively, conformal thin-film materials, such as polyimide and parylene-C, present good biocompatibility and chemical stability [15, 31, 137, 159–161] and, therefore, have been gaining attention for PNI [162–164]. In particular, parylene-C permits the thermal reshaping of its structure through a process known as *thermoforming*. This process can be leveraged to produce 3D neural interfaces, such as nerve cuffs [165].

Besides the fabrication materials, mechanical attachment to the nerve is also important for PNI [166]. Recently developed models of cuff electrodes present a pre-folded shape achieved using stress during their fabrication. Their implantation procedure usually requires manual unfolding during nerve interfacing [167], which becomes increasingly difficult and risky as the cuff size decreases. In particular, thin-film electrodes are typically very challenging to handle. New methods are being explored to interface cuff electrodes with small nerves. For example, there are shape-memory polymers that fold when heated to body temperature [59]. Another approach uses a combination of swelling and flexible materials to fold the electrode around the nerve when in contact with water, achieving folding diameters of about 50 µm, but so far, none of these methods have shown successful stimulation and recording performance on small nerves below 200 µm in vivo [168, 169].

In this chapter, I evaluate two novel multi-contact cuff electrodes for small nerves. The first device consists of a 4D-printed electrode with a self-folding structure that wraps around small nerves during the insertion. The second device is pre-rolled using thermoforming to shape the cuff to the dimension of the nerve. Its insertion mechanism reduces to simply pulling the electrode for the nerve to slide smoothly inside, making the interfacing mechanism extremely simple. Furthermore, the extraction mechanism is also simplified, as it only involves gently pulling the electrode out. The device features parylene-C as a substrate that supports a Pt/Ir alloy as the electrode material. Pre-rolled and multisite parylene-C cuff electrodes have already been successfully used for PNI, but their cuffing dimensions ($> 350\,\mu\text{m}$) are not applicable for our target nerves ($< 200\,\mu\text{m}$) [164, 170]. The suitability for implantation of both devices is tested in our animal model. The devices are straightforward to fabricate, as they dispense with complex and costly lithographic techniques, and allow to easily exchange the metal used, for example, Pt or Au.

5.3 Materials and methods

In the following, I describe the characterization methods for both devices. We used adult male and female locusts (*Locusta migratoria*) for the in vivo experiments. Since the study was conducted exclusively with insects, no special permission is required in Germany. All experiments complied with the German laws for animal welfare (“Deutsches Tierschutzgesetz”).

5.3.1 Self-folding cuff electrodes

Electrochemical characterization

Electrochemical impedance spectroscopy (EIS) and cyclic voltammetry (CV) were performed to characterize the electrodes using a potentiostat (PalmSens4, PalmSens, Netherlands) in PBS. EIS was performed in a three-electrode setup, using a Pt mesh counter and a Ag/AgCl ($3\,\mathrm{mol\,dm^{-3}}$ NaCl) reference electrode. During the experiments, no bias voltage was applied against the open circuit potential (E_{oc}). A sinusoidal wave with an amplitude of 10 mV vs. E_{oc} was applied to measure the impedance of the electrodes between 1 Hz and 500 kHz. CV was performed in the same three-electrode setup over a potential range of $-1.6\,\mathrm{V}$ to $1.7\,\mathrm{V}$, with a scan rate of $100\,\mathrm{mV\,s^{-1}}$. This voltage range was swept 10 times, and only the last voltammogram was used for the data analysis.

The voltage response of the electrodes to biphasic current pulses was recorded with an oscilloscope (InfiniiVision DSOX2024A, Keysight, USA). The current pulses were applied with an electrophysiology stimulator/amplifier chip (RHS2116, Intan Technologies, USA). The phase of each pulse had a duration of 300 µs (leading cathodic) with a 50 µs interphase delay. The amplitude of the pulses ranged between 100 and 1000 µA in steps of 100 µA.

In vivo experiments

The surgical procedure used was already described in Chapter 3. The cuff electrode was approached with the aid of micromanipulators and fine tweezers and wrapped around the nerve. The contact pads of the electrodes were interfaced with a 6-pin zero insertion force (ZIF) connector (Würth Elektronik GmbH & Co. KG, Germany). This connector bridged the electrodes to an INTAN RHX control system, using the RHS2116 headset (INTAN Technologies, USA) to stimulate and record activity from the nerve. Locust's saline solution was applied to the thoracic cavity to prevent the nervous tissue from drying during the procedure ($147\,\mathrm{mmol\,dm^{-3}}$ NaCl, $10\,\mathrm{mmol\,dm^{-3}}$ KCl, $4\,\mathrm{mmol\,dm^{-3}}$ $CaCl_2$, $3\,\mathrm{mmol\,dm^{-3}}$ NaOH and $10\,\mathrm{mmol\,dm^{-3}}$ HEPES buffer, Sigma Aldrich, St. Louis, USA [118]).

The N5 was stimulated with two biphasic current pulses (leading cathodic, 300 µs apart) with an amplitude of 70 µA and a duration of 300 µs per phase, separated by a 100 µs delay between phases. The pulse pattern was delivered every 2 s, and the leg movement response was captured on camera. The tibiofemoral joint angle was estimated using a self-written code in MATLAB (MATLAB 2022a, MathWorks, USA).

Finally, the neural activity of the N5 was recorded from all channels at 30 ksps. The recording was performed against a Ag/AgCl electrode on the contralateral side of the metathorax. The abdomen of the animal was lightly touched with a non-metallic instrument to elicit a motor reaction. The acquired signals were subsequently filtered in MATLAB using a FIR band-pass filter between 0.8 and 2.2 kHz [171].

5.3.2 Pre-folded cuff electrodes

Mechanical characterization

The opening force of the cuff electrodes was measured with a tensile tester (Universal Testing Machine 106, TesT GmbH, Germany). A copper wire with a diameter of 150 µm was mounted on a 3D-printed platform and tightened with screws. The cuff electrode was then carefully wrapped around the copper wire. Both the cuff electrode and the base were mounted on the tensile tester and pulled apart from each other slowly at $0.5\,\mathrm{mm\,min^{-1}}$. The increasing force was recorded until the cuff electrode detached from the wire. The maximum force span was computed for each cuff electrode. $\mathrm{n_{long}} = 16$ devices with a length of $\mathrm{l_{long}} = 1.6\,\mathrm{mm}$ and $\mathrm{n_{short}} = 29$ devices with a length of $\mathrm{l_{short}} = 1.2\,\mathrm{mm}$ were used for this measurement.

Electrochemical characterization

The electrochemical properties of the electrodes were characterized using CV and EIS in a Faraday cage using locust's saline solution at room temperature in a three-electrode setup as described before. The measurements were carried out with a potentiostat (PalmSens4, PalmSens, Netherlands). Before the measurements, the electrodes were cleaned by linearly sweeping their voltage 10 times back and forth between $-0.2\,\mathrm{V}$ and $1.5\,\mathrm{V}$ vs. Ag/AgCl at an absolute rate of $500\,\mathrm{mV\,s^{-1}}$ in $0.2\,\mathrm{mol\,dm^{-3}}$ $\mathrm{H_2SO_4}$. The potential of the CV experiments was swept between -0.6 and $0.8\,\mathrm{V}$ vs. Ag/AgCl with a scan rate of $50\,\mathrm{mV\,s^{-1}}$ to keep the Pt/Ir electrode polarization within the water window. Three cycles were recorded in every experiment, whereby the last cycles were used for the analysis. The cathodic charge storage capacity ($\mathrm{CSC_c}$) was calculated using Equation (2.14).

The EIS was measured in a frequency range from 0.1 Hz to 5 kHz by applying a sinusoidal signal with an amplitude of 10 mV. The electrodes were then subject to a long-term stimulation process, consisting of the application of 10^7 biphasic stimulation pulses (100 µA and 300 µs per phase, 1 ms pulse period) and the EIS measurements were conducted again.

In vivo experiments

After the surgical procedure already described in Chapter 3, the cuff electrode was approached with the aid of tweezers and the nerve slid into it. The electrode contact pads were interfaced with a flat cable using conductive tape (ECATT 9703, 3M, USA) and the other end of the cable was connected to a zero-insertion-force (ZIF) connector (Würth Elektronik GmbH & Co. KG, Germany). The ZIF connector was then interfaced to an INTAN RHS2116 headset and used to drive the stimulation currents, as described before. The stimulation signal consisted of a biphasic pulse of 400 µs and 45 µA per phase, with an inter-pulse delay of 100 µs. The nerve was stimulated every 3 s and the leg movement response was captured on camera. Finally, the tibiofemoral joint angle was estimated using a self-written code in MATLAB (MATLAB 2022a, MathWorks, USA).

The cuff electrodes were implanted in 12 subjects to assess their implantation effects in insects. Surgery without implantation was performed on another group of 12 subjects which served as a control group. Their wounds were sealed and the two groups were kept in separate terrariums at ~30 °C and a 12 h light period for two weeks. Afterward, the implanted subjects were sacrificed and samples of the metathorax were fixed in 10% neutral buffered formalin and decalcified using a formic acid-based decalcifying solution. Sections of 2 µm were cut using a rotating microtome (RM2245 Leica Biosystems, Wetzlar, Germany). The sections were then stained with hematoxylin-eosin and Masson's trichrome following standard procedures. The slides were then scanned in 40× magnification using a whole-slide brightfield scanner (Aperio AT2, Leica Biosystems, Wetzlar, Germany).

5.4 Results and discussion

5.4.1 Self-folding cuff electrodes

Electrochemical characterization

Typically, a low electrode impedance is desirable for stimulation to deliver the necessary amount of charge while minimizing the polarization of the electrodes. A high electrode polarization could elicit redox reactions on the surface of the electrodes, which generate noxious species or degrade the performance of the electrodes. To assess the influence of stimulation on the electrode performance, we compared the impedance obtained from the EIS measurements of 16 electrodes before and after applying 10^6 stimulation pulses. The Bode plots for both cases are presented in Figure 5.1(a), showcasing that the average magnitude of the impedance of the electrodes increases slightly after the stimulation. For example, at 1 kHz, the magnitude of the impedance increases from ~6 to ~10 kΩ, and similar changes are seen across all measured frequencies. This result is expected, as the stimuli could have briefly generated gas bubbles between the Au micro-cracks, delaminating some weakly attached Au.

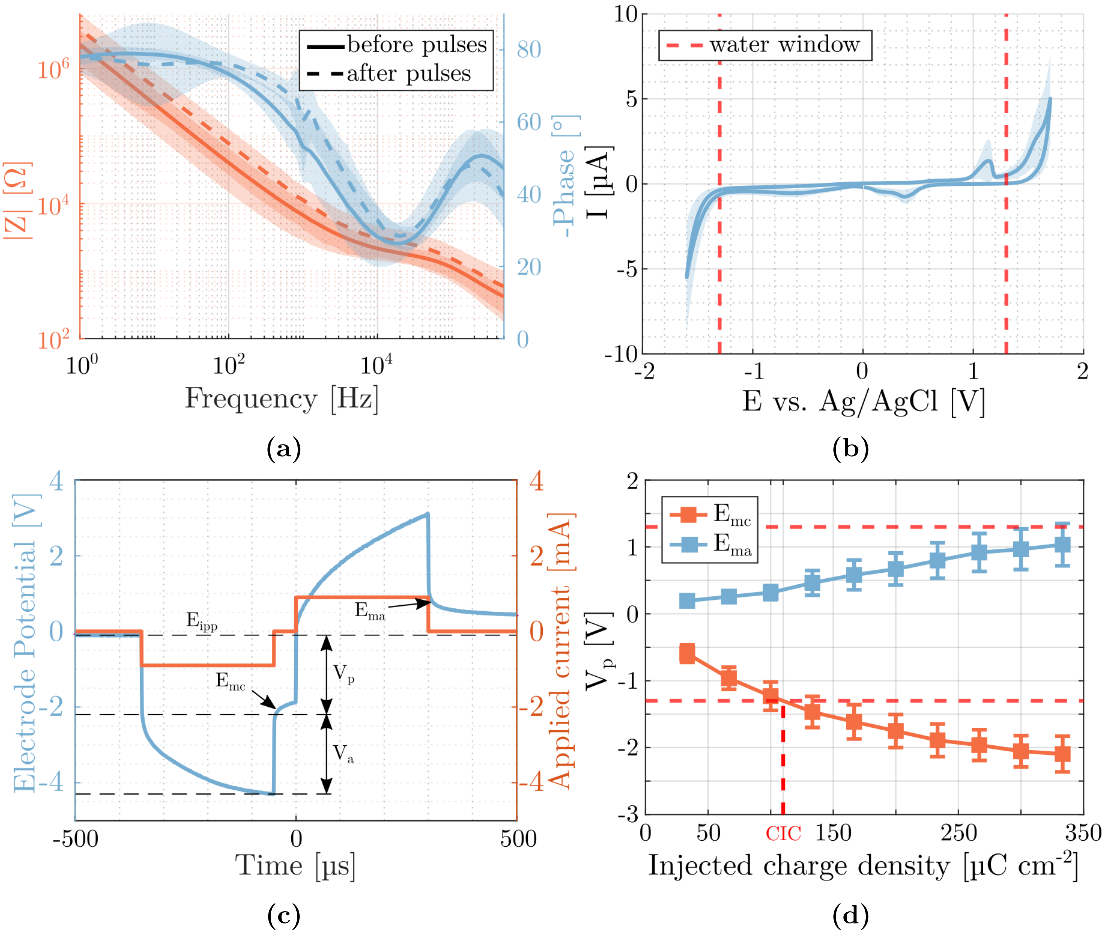

Figure 5.1: Electrochemical characterization of the active electrode in PBS. **(a)** Bode plots of the impedance of the electrodes in PBS depicted as the mean and the standard deviation of 16 electrodes. The solid and dashed lines show the EIS before and after delivering 10^6 biphasic current pulses, respectively. **(b)** CV of 16 electrodes scanned at 50 mV s^{-1}. We determine the water window to be at ±1.3 V. **(c)** Representative voltage transient resulting from a 0.9 mA biphasic stimulation pulse. Here, we showcase the relevant voltage values to calculate the electrode's charge injection capacity (CIC). This trace corresponds to an injected charge density of 300 µC cm^{-2}. **(d)** The charge injection density of 16 electrodes, shown in mean and standard deviation. The charge injection capacity is estimated to be 121 µC cm^{-2}.

We conducted CV measurements to further characterize the electrodes' stability and determine the water window. The mean and standard deviation of the 16 voltammograms for Au vs. Ag/AgCl (3 mol dm^{-3} NaCl) with a Pt mesh counter electrode in PBS are shown in Figure 5.1(b). The high current magnitudes at the highest and lowest applied voltages correspond to the electrolysis of water. Therefore, we set a conservative water window in the range of ±1.3 V. Lower current peaks can be noticed at ~1.1 V (anodic) and ~0.6 V (cathodic) vs. Ag/AgCl, probably corresponding to the oxidation and reduction of Au, respectively.

The electrode's charge injection capacity (CIC) determines how much charge can be injected into the electrolyte without polarizing the electrode beyond undesired limits. We set the water window as the safe stimulation limit in our case. We stimulated 16 electrodes with cathodic-leading biphasic pulses of increasing amplitude ranging from 100 to 1000 µA and show one of the voltage transient responses in Figure 5.1(c). The most cathodic (E_{mc}) and most anodic (E_{ma}) electrode polarization voltages are acquired from the measurements and compared with the water window. Determining these voltage levels from a voltage transient is challenging, and there are even attempts to automate their calculation [172]. We estimated V_a visually and then calculated E_{mc} using Equation (2.16). E_{ma} was estimated using the same formula but using the $\varDelta V$ and V_a values from the anodic part of the trace. Then, we converted the injected current to the surface charge density as $Q_{inj} = (I_{inj} \cdot t_p) \,/\, A$, where Q_{inj} represents the injected surface charge density, I_{inj} the stimulation current amplitude per phase, t_p the phase duration, and A the electrode area. The mean and standard deviation of the corresponding E_{mc} and E_{ma} estimations are presented in Figure 5.1(d) using a fit of the discrete values with a quadratic regression. We finally estimated the CIC as the injected charge corresponding to the intersection between the first polarization voltage E_{mc} or E_{ma} and the established water window, obtaining a CIC of $121\,\mu C\,cm^{-2}$. These values are slightly lower but in the same order of magnitude as results reported in literature for Au electrodes ($200\,\mu C\,cm^{-2}$) [173]. The reduced CIC compared to flexible but non-deformable electrodes can be caused by the micro-cracking design. For applications requiring higher CICs, the performance could be potentially improved with an additional coating of a porous conductive polymer, such as PEDOT:PSS [173, 174].

In vivo validation

We interfaced the N5 of the locust *Locusta migratoria* to validate the in vivo performance of the 4D cuff electrodes. The small size of this nerve (~150 µm in diameter) and the limited useful length for interfacing inside the metathoracic cavity (~2 mm) make the locusts an excellent model to test the interfacing capabilities of our device. The cuff electrode we present has 6 channels, an inner diameter of ~150 µm when folded and a width of 850 µm. However, making a multichannel planar electrode with the appropriate dimensions for a small nerve in a restricted environment is only half the story. Interfacing with small nerves usually requires a great deal of skill from the practitioner. Commercially available cuff electrodes are traditionally fixed to the nerve by stitching or buckling around them, which is more challenging at smaller scales (e.g., CorTec GmbH, Freiburg, Germany, MicroProbes, Gaithersburg, MD, USA). Our self-foldable cuff electrodes are comparatively easy to attach to the nerve, as they just need to be approached to it, wrapping around it after contact with water in 20 to 30 s.

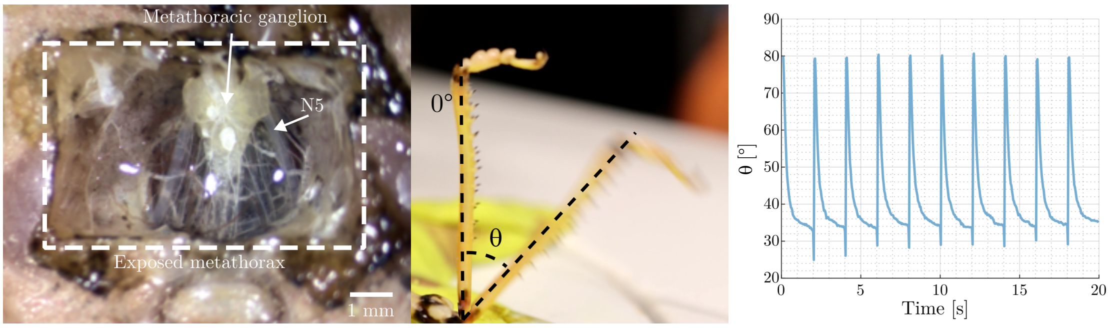

(a) **(b)** **(c)**

Figure 5.2: Interfacing of the locust N5 with the 4D cuff electrode. **(a)** Metathoracic cavity of a locust, exposing the metathoracic ganglion and nerves. **(b)** Movement of the hindleg elicited by the nerve stimulation. **(c)** Angle of the leg over ten stimulation pulses.

Stimulation To validate the stimulation capabilities of the 4D cuff electrode, we stimulated the nerve with biphasic current pulses and recorded the elicited leg response on camera. The pulses were delivered between 2 electrodes every 2 s. The stimuli triggered the leg's fast extensor tibiae neuron (FETi), provoking it to extend its tibiofemoral joint [74]. Figure 5.2(c) showcases one stimulation experiment comprising 10 stimulation pulses and showing the tibiofemoral joint angle vs. time, with similar values for every stimulation pulse. Repetitions of the same experiment in other subjects showed variability in the elicited angle span between the subjects but repeatability within the same subject. This can be attributed to the position of the electrode with respect to the nerve and its proximity to the FETi, which varied between subjects.

Recording Additionally to the stimulation, we also evaluated the recording capability of the electrodes. After nerve attachment, we could detect spontaneous neural activity, which was always present even without movement, probably corresponding to sensory signals. Then, we elicited movement by lightly touching the abdomen of the locust. Correspondingly, the sudden movement of the leg was reflected as larger and bursting neural activity. A representative trace of the recording is shown in Figure 5.3(a). The signal was band-pass filtered between 0.8 and 2.2 kHz to reduce noise and muscle movement artifacts [171, 175, 176]. After filtering, the noise floor was calculated to be ~4 μV_{rms}. Traditional extra-neural recording techniques, such as interfacing with hook electrodes, usually record action potentials with higher amplitudes when the nerve is pulled out of the hemolymph. Nevertheless, it is important to highlight that the presented recordings were performed with the electrode immersed in the animal's hemolymph, a condition for implantable electrodes that hook electrodes cannot meet. Furthermore, the geometrical arrangement of the 6-channel cuff electrode permits the distinction of the direction of propagation of the neural activity along the nerve, depending on the dephasing profile, with electrodes 1 to 6 (ch1-ch6) going in the proximal to distal direction. Figure 5.3(b) shows a ch1-leading signal, corresponding to efferent motor neural activity, while Figure 5.3(c) depicts a ch6-leading signal, corresponding to afferent sensory neural activity. In one minute of the shown trace, 218 efferent and 129 afferent signals were detected.

Extraction During the experiment, the cuff electrode moved along with the nerve when the animal moved without detaching. However, when the cuff pulls the nerve

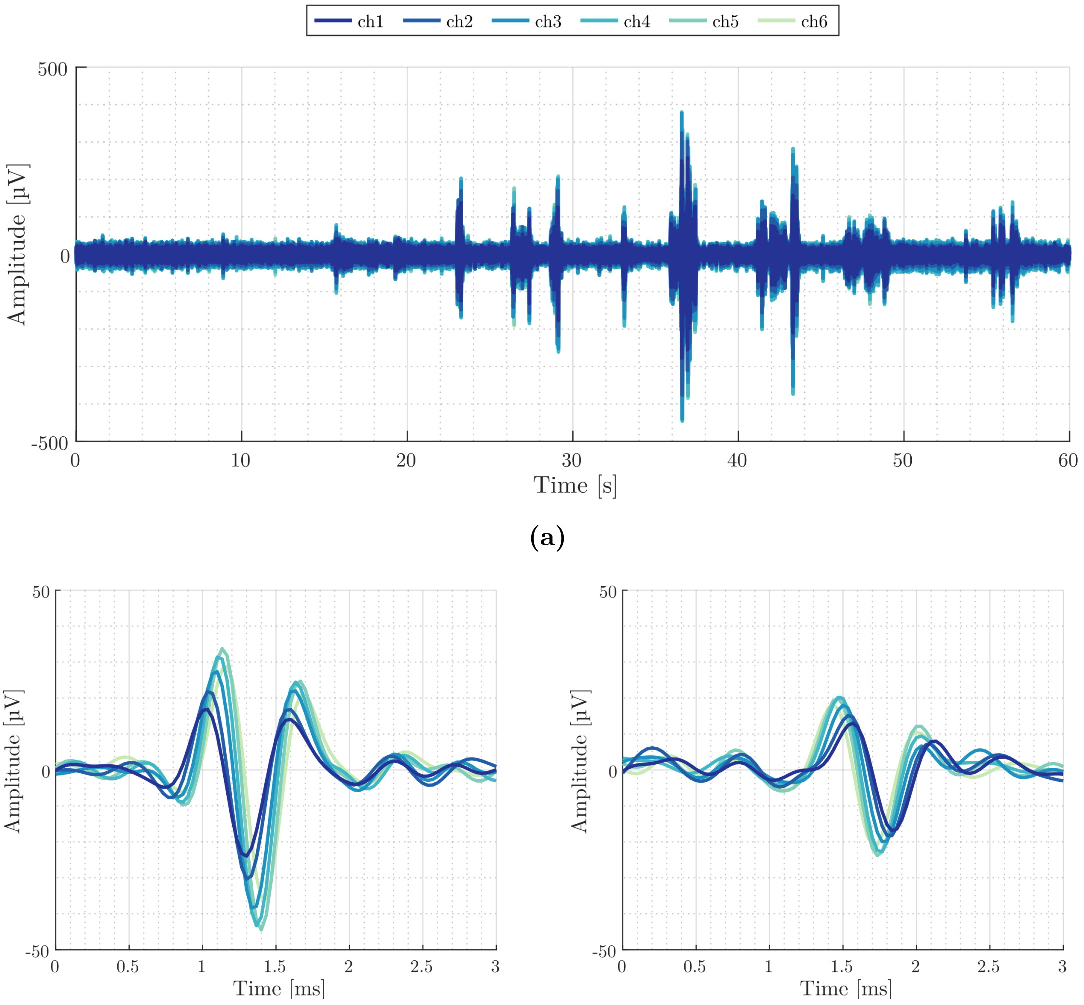

(a)

(b) **(c)**

Figure 5.3: Electrophysiological recordings of spontaneous activity of the N5 with a 6-channel cuff electrode. **(a)** Activity during one minute, the larger spikes correspond to leg movement. Zoomed-in snippets from the main trace at different times show **(b)** a motor signal traveling from the ganglion to the leg (efferent) and **(c)** a sensory signal traveling from the leg to the ganglion (afferent). The direction of propagation of the signal can be determined from the observed phase delay between the different channels, with **(b)** the most proximal channel (ch1) leading during efferent activity and **(c)** lagging during afferent activity.

more strongly, the cuff electrode can unfold again. Using this property, the cuff electrodes were detached from the nerve after every experiment by gently pulling them off. Leg movement was normally elicited as a response to light touches on the abdomen of the locust after extraction of the cuff electrode. This observation suggests that the interfacing and the extraction cause little or no damage to the nerve.

5.4.2 Pre-folded cuff electrodes

Electrode fabrication

The pre-folded devices are made with a parylene-C substrate and Pt/Ir electrodes. The electrodes are distributed along the length of the cuff (l) and around its inner circumference (h) in an $l \times h$ fashion. The 6-electrode design presents a 2×3 distribution, whereas the 15-electrode has a 3×5 distribution. The fabricating procedure for a 6-electrode cuff is shown in Figure 5.4(a) – Figure 5.4(f) and a picture of the final device in Figure 5.4(g). The device is flexible and can accommodate the narrow spaces where small nerves are usually found (Figure 5.4(h)). The cuff diameter can be tuned easily tuned to fit custom nerve sizes (Figure 5.4(i)). The interfacing mechanism simply consists of sliding the nerve inside the cuff. Since the electrode is made of ~10-µm-thick parylene-C, it is highly flexible and bendable. This feature permits the electrode to deform and access otherwise restricted areas to interface the nerve.

Mechanical characterization

One important characteristic of cuff electrodes is the mechanical compliance to the interfaced tissue. Since the nerves are in movement with respect to other tissue, the cuff electrodes should be strong enough to remain attached to the nerves under these conditions. However, a very strong compressing force can generate nerve trauma and

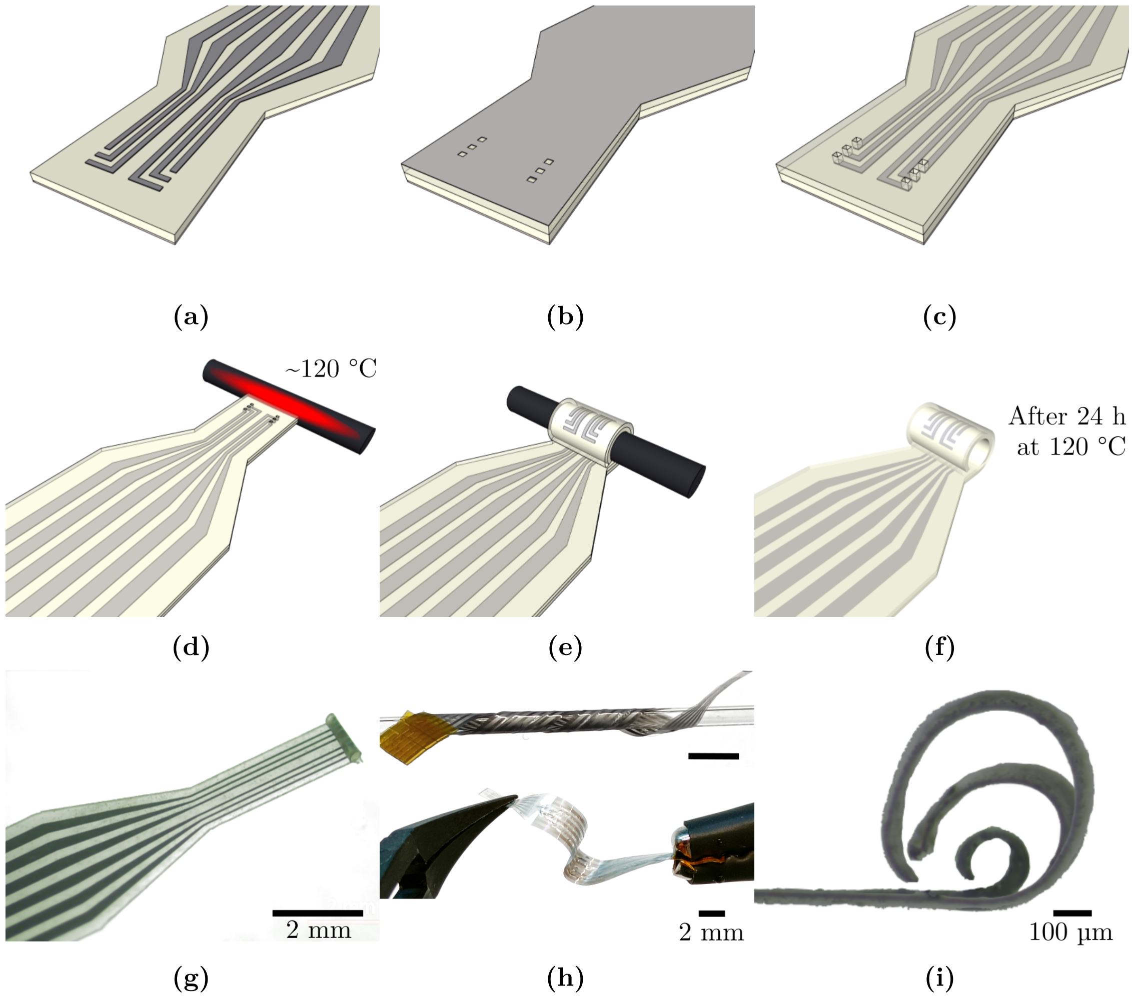

(a) (b) (c)

(d) (e) (f)

(g) (h) (i)

Figure 5.4: The pre-folded electrodes are fabricated by **(a)** depositing a substrate of 5 µm parylene-C, sputtering Pt/Ir on top and patterning it to the shape of the electrodes. Then, **(b)** a second layer of parylene-C is deposited on top, followed by a metal coating of Al, which serves as a masking layer for etching the parylene-C. The coating over the electrode sites is laser-etched. Finally, **(c)** the parylene-C over the electrode sites is O_2-etched and the masking layer is removed with KOH. To pre-fold the device, **(d)** its tip is attached to a resistively heated wire of the desired diameter of the target nerve. After attachment, **(e)** the cuff is rolled and later thermoformed to obtain the final cuff shape **(f)**. **(g)** shows a picture of the device at the end of the fabrication process. **(h)** The final device is highly flexible, which is advantageous for implantation in constrained spaces. **(i)** The diameter of the cuff can be easily tuned to the desired nerve.

should be avoided. We estimated the compression force of our devices by measuring the force necessary to open the cuff. This measurement was carried out by attaching the cuff electrodes to a nerve surrogate and pulling it slowly while measuring the force until detachment. For this purpose, we used long ($n_{long} = 16$, $l_{long} = 1.6\,mm$) and short ($n_{short} = 29$, $l_{short} = 1.2\,mm$) devices and determined that the maximum opening force was $F_{open} = \sim 25\,mN$. The obtained low opening-force values suggested that the electrode extraction could be performed by simply pulling the electrode off the nerve, which was later experimentally confirmed. Nerve stretching experiments performed in small rodents show that a force of approximately $3.25 \pm 0.54\,N$ is required to break the nerve, and $0.71 \pm 0.18\,N$ is required to abolish compound action potentials [177]. In comparison, the opening force values registered for our electrodes were between one and two orders of magnitude lower.

Electrochemical characterization

We performed cyclic voltammetry to determine the water window for our devices. The results of these characterizations are shown in Figure 5.5. Figure 5.5(a) shows the resulting voltammograms in mean and standard deviation for 12 electrodes before and after the thermoforming procedure. The water window can be determined between -0.6 and $0.8\,V$ vs. Ag/AgCl. The particular shape of the voltammograms corresponds to the results in literature [178]. From the voltammogram of the folded electrode, we computed the CSC_c of the electrodes, a value that characterizes how much charge they can store, and obtained a value of $4.6\,mC\,cm^{-2}$. This value is consistent with those reported in the literature for Pt/Ir electrodes with the same atomic ratio (80/20) measured at the same scan rate [179, 180].

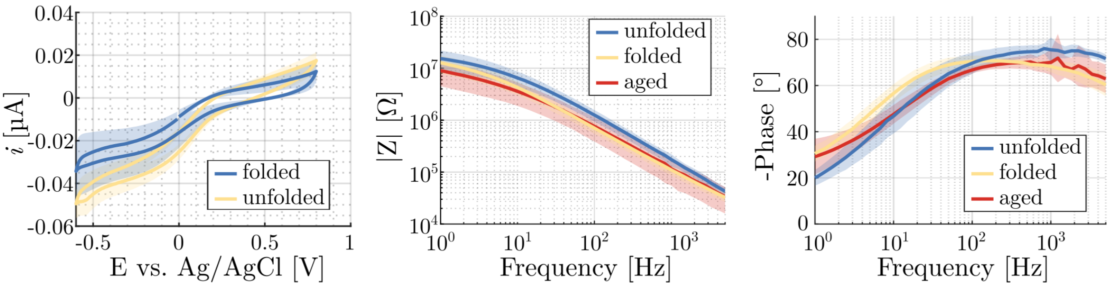

(a) **(b)** **(c)**

Figure 5.5: Electrochemical characterization of the pre-folded devices. **(a)** Voltammograms for unfolded and folded electrodes (n = 12). **(b)** Magnitude and **(c)** phase of the impedance of unfolded, folded and long-term stimulated ("aged") electrodes (n = 12).

Nerve stimulation involves delivering current through the electrode-electrolyte interface. However, delivering enough current to elicit a nerve response without damaging the electrode is a current challenge for thin-film electrodes [174, 181]. To make matters worse, thin-film metallic electrodes are prone to delamination [182]. Since electrochemical stability is an important characteristic of thin-film electrodes, we simulated long-term usage of the electrodes by delivering biphasic currents with amplitudes of 100 µA, ~2 times larger than those usually required for nerve stimulation. The electrode stability was assessed with EIS measurements. Figure 5.5(b) and Figure 5.5(c) show the impedance of 12 electrodes in mean and standard deviation before and after the application of 10^7 stimulation pulses. It can be seen that the long-term stimulation decreased the mean value of the impedance of the electrodes in the low-frequency range, probably due to electrode cleaning or the delamination of the passivation caused by the formation of gas bubbles on the electrodes.

Implantation procedure and interfacing

As explained previously, interfacing small nerves is a challenging task for the practitioner. Our pre-folded devices facilitate this task, as they just have to be positioned below the nerve, and a slight upward pull will cause the nerve to slide gently into the cuff. Pulling the cuff electrode beyond the opening force stated in the previous section will open the cuff, consequently releasing the nerve. After the extraction, the insect was able to use its leg normally, suggesting that no lasting damaged was caused to the nerve by either the interfacing or the extraction procedures.

Multi-electrode nerve cuffs can potentially recruit different axons or groups of axons independently, thus increasing the stimulation selectivity. Our devices increase the spatial selectivity by placing electrodes around the nerve. To assess the electrical performance of the electrodes, we stimulated the N5 under different 1-to-1 electrode combinations and recorded the elicited leg movement with a camera. The used device comprised 6 electrodes, and all combinations of 2 electrodes without repetitions $\binom{6}{2} = 15$ were tried. Movement was elicited only in 8 out of the 15 total combinations. Under the same stimulation conditions, no movement was elicited for the other 7 combinations, suggesting that the spatial electrode configuration plays a role in the selective stimulation of the nerve. Figure 5.6(e) shows the angle span achieved for every successful electrode combination ($\mathrm{n}_{\mathrm{repetition}} = 10$). It is important to note that the same experiment in different subjects is not bound to elicit the same results, as there is variability in the relative position between the electrode and the nerve in every interfacing procedure. Therefore, while we observed similar results in other subjects, we report them only for one subject in this work.

Post-implantation analysis

To assess the suitability of our electrodes in insects, we implanted them in 12 locusts and established a control group of also 12 locusts, which only underwent the surgical procedure. Immediately after the surgery, the subjects resumed their regular activities. Furthermore, they retained their jumping ability, suggesting that the implantation process did not affect the physiology of the nerve. They were kept in their terrariums under controlled temperature and light patterns and observed during the following two weeks. All the subjects in the implanted and control groups survived past the two weeks and did not show any impaired behavior or movement patterns, suggesting that our devices do not cause mortality of the subjects within the time frame of the experiment.

Next, we histologically evaluated the foreign body response (FBR) of the locusts to the implants. We performed hematoxylin-eosin (Figure 5.7(a)) and Masson's trichrome (Figure 5.7(b)) stainings according to standard protocols. The images show the formation of a monocellular capsule surrounding the cuff electrodes, which is not present on the nerves that were not interfaced (Figure 5.7(c)). There is no evidence of capsular fibrosis in Masson's trichrome stain (Figure 5.7(b)). The observable reaction is consistent with the physiological encapsulation process of foreign objects in our chosen locust species, as described previously by Brehélin et al. [183]. Consequently, these results suggest that our devices do not elicit abnormal FBR in our subjects.

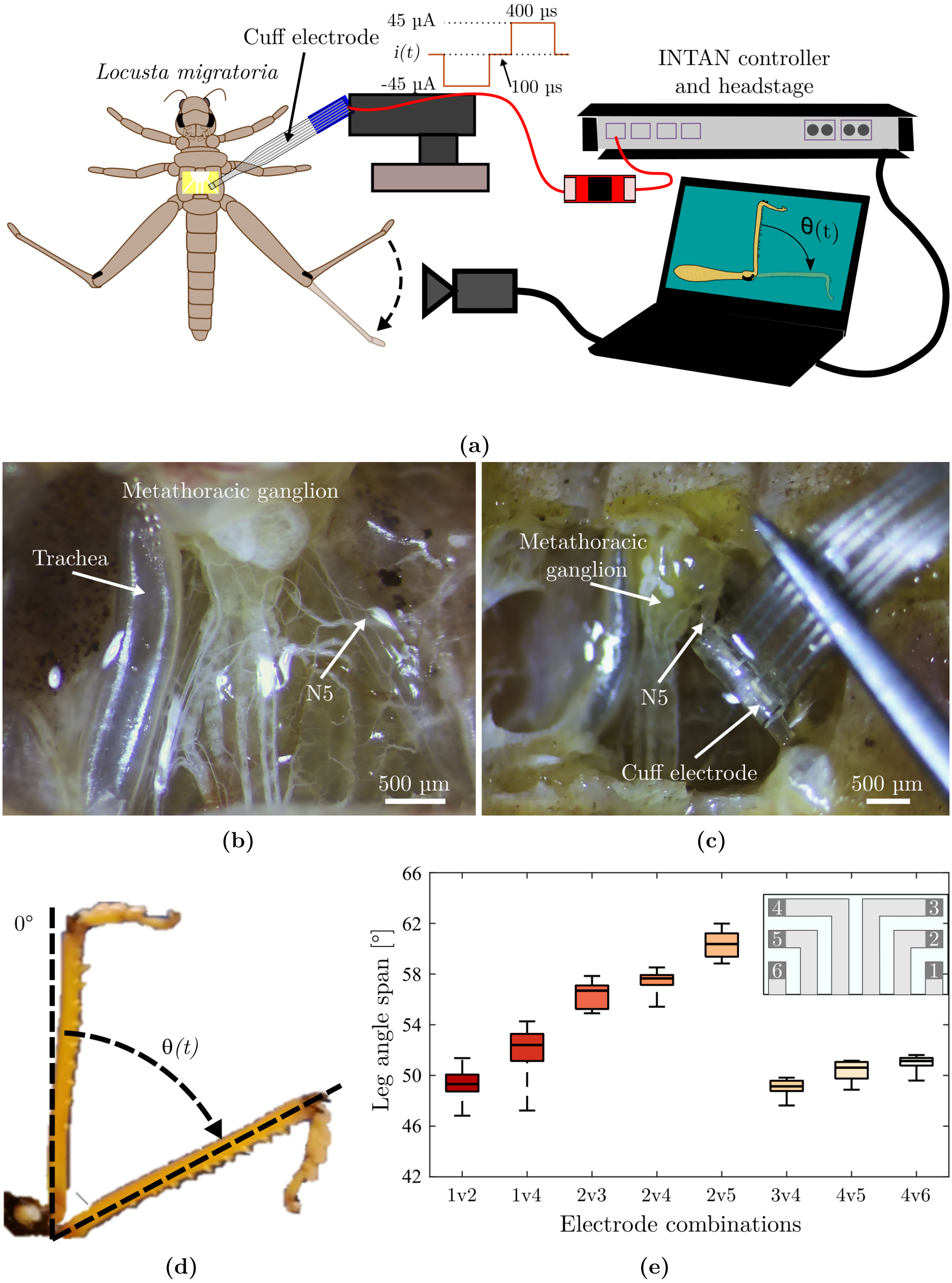
Locusta migratoria
Cuff electrode
45 µA
i(t)
-45 µA
400 µs
100 µs
INTAN controller
and headstage
θ(t)
(a)
Metathoracic ganglion
Trachea
N5
500 µm
(b)
Metathoracic
ganglion
N5
Cuff electrode
500 µm
(c)
0°
θ(t)
(d)
66
62
58
54
50
46
42
Leg angle span [°]
1v2
1v4
2v3
2v4
2v5
3v4
4v5
4v6
Electrode combinations
4
3
5
2
6
1
(e)

Figure 5.6: **(a)** Schematic of the setup used for in vivo experiments. **(b)** The metathoracic cavity of the locust prior to electrode interfacing, indicating the target nerve. **(c)** Successful nerve interfacing with our cuff electrode. **(d)** Superimposed hind leg image depicting how the angle is measured. **(e)** Angle span for the electrode combinations that elicited leg movement. The inset illustrates the location of the electrode number on the unrolled cuff.

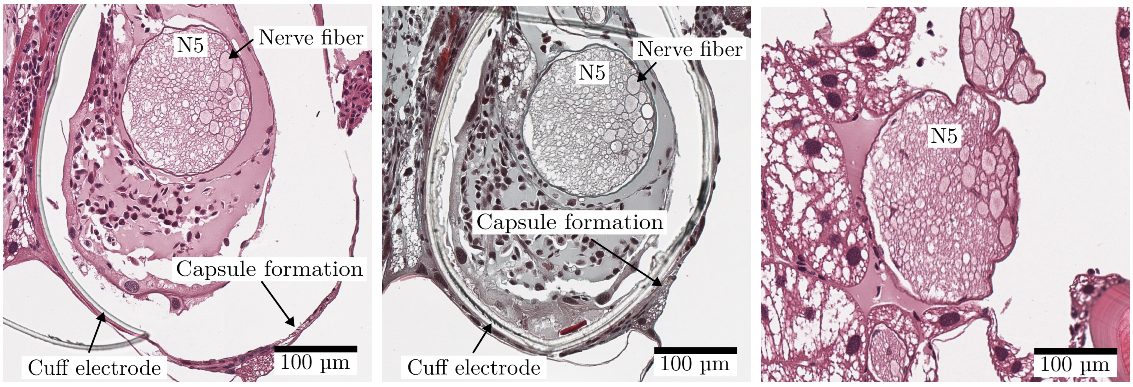
N5
Nerve fiber
Capsule formation
Cuff electrode
100 µm
N5
Nerve fiber
Capsule formation
Cuff electrode
100 µm
N5
100 µm

(a) **(b)** **(c)**

Figure 5.7: Histological images of the N5 interfaced with the pre-folded cuff electrodes stained with **(a)** hematoxylin-eosin and **(b)** Masson's trichome. A tissue layer is formed around the parylene-C cuff. The gap between the cuff and the nerve is due to the nerve shrinking during the fixation process. **(c)** A non-interfaced nerve does not present the capsule formation around it.

5.5 Conclusions

In this chapter, I presented two novel cuff electrode devices for small nerves. On the one hand, a 3D-printed electrode for PNI, which can fold itself into a cuff around small peripheral nerves when exposed to water during the surgery. The materials used for its fabrication make the electrode robust and easy to handle. Furthermore, the triggered self-folding mechanism greatly facilitates the interfacing procedure for the surgeon compared to other devices. I believe this simple handling is key to bringing PNI into a broader clinical application. Finally, I showed that the electrode can reliably stimulate small nerves and perform electrophysiological recordings from them. The successful in vivo results on insects suggest that acute functional interfacing of our devices is possible.

On the other hand, a parylene-C device that featured a pre-folded cuff shape acquired through a thermoforming process. Stimulation of the N5 in locusts with specific electrode configurations yielded repeatable tibiofemoral joint angle extension. Further, tissue histology after the survivability period showed a normal encapsulation FBR.

CHAPTER 6

Conclusions and outlook

In this work, I presented an analysis of extraneural interfaces for small peripheral nerves. Furthermore, I developed and characterized novel extraneural devices using state-of-the-art techniques and applied them in vivo. At the same time, I developed a small animal model framework using the insect *Locusta migratoria.* This animal model provides access to several small nerves, in particular the metathoracic N5 that innervates the hind leg of the locust and provides a natural biomarker for stimulation. Similarly, bidirectional neural recordings can be acquired from this nerve.

First, I developed a silicone-based cuff electrode and used it for in vivo stimulation in a closed-loop control system. Next, I designed and characterized a multi-contact cuff electrode for small nerves, which was fabricated using a combination of inkjet printing and two-photon stereolithographic techniques. I also validated its stimulating and recording selectivity in vivo. Finally, I characterized two novel electrodes made with soft and flexible materials, which were successfully implanted in the animal model for a period of two weeks. Moreover, a histological analysis of the interfaced tissue showed a normal encapsulation foreign body response for one of these devices.

In the rest of the chapter, I compare the presented electrodes in terms of their characteristics.

6.1 Recording and stimulation

Nerve recordings pick up the extracellular potentials that propagate along the nerve fibers. To effectively record from extraneural electrodes, there are some important characteristics to consider, such as low electrode impedance, a proper cuff seal, and high electrode count [144]. However, these characteristics often conflict with each other. For example, an increased number of electrodes within a cuff allocates a smaller surface area for each and, therefore, increases their impedance.

Hook electrodes and the PDMS cuff electrode presented low electrode impedance but with a low electrode count. The 3D-printed cuff electrode improved the electrode count while keeping the impedance low. Furthermore, it provided a better electrical sealing that allowed direction-selective recordings. The softer, self-folding cuff electrode increased the electrode count while also keeping a low impedance. However, the seal tended to be imperfect to the sides, usually decreasing the amplitude of the recorded signals on the electrodes close to the ends. Finally, the pre-folded device further increased the electrode count but compromised its impedance and signal recording was not possible. For future developments, the cuff sealing should be a priority for cuff-electrode development to enhance nerve recording. This could be improved through the use of flexible, compliant materials that accommodate the shape of the nerve and more reliable nerve attachment mechanisms.

The requirements for nerve stimulation are more relaxed compared to recording. However, electrode impedance and sealing are still important for proper stimulation. A very high impedance usually results in an increase in the electrode polarization, which enhances redox reactions, whereas poor sealing makes the stimulation current less effective and focused. The stimulation behavior of the presented electrodes was very similar, requiring biphasic current pulses of approximately 25 nC per phase to elicit a visible response. An exception to these observations are the hook electrodes, which only required half of the charge when pulled out of the electrolyte. However, they required much more charge per phase when immersed because of improper sealing. Finally, the effect of the relative position of the cuff electrodes around the nerve was noticeable. Since the FETi is closer to one side of the nerve, electrodes placed closer to this side required lower stimulation currents.

6.2 Selectivity and invasiveness

Perhaps the most important compromise of electrode design is the ratio between selectivity and invasiveness. The least invasive type of extraneural interfacing is placing the electrodes on top of the nerve. However, the lack of a mechanical attachment could cause a displacement between the electrode and the nerve over time. Nevertheless, this technique is clinically used, for example, to treat obstructive sleep apnea [184]. We validated the in vivo performance of a novel surface electrode fabricated with a substrate of chitosan nanofibers and different electrode materials such as carbon nanotubes, silver nanowires and PEDOT:PSS [185].

While hook electrodes achieve a good SNR in a mineral oil bath, they tend to be large and are restricted to a reduced number of electrodes. A further limitation of them is that they are not straightforward to implant, as their mechanical interfacing consists of pulling the nerve upwards to achieve it. The device presented in Chapter 3 is also made of thin metal wires but features a silicone cuff to cushion the nerve. Cuffs present the advantage of limiting the ionic current dispersion that permits the recording from more axons compared to hook electrodes [144]. This device can be implanted since the mechanical attachment is performed by the silicone tube. Nevertheless, the fabrication mechanism also restricts the number of active sites.

The fully 3D-printed cuff electrode presented in Chapter 4 has an increased number of contact sites distributed spatially along the length of the nerve. This design permitted to record the signals propagating along the nerve, estimate their conduction velocity and determine the direction of propagation. This result was later reproduced with the self-folding devices presented in Chapter 5. Electrodes distributed along the direction of propagation further permitted to create custom electric fields for stimulation, as shown in Chapter 4. The pre-folded devices presented in Chapter 5 present an electrode distribution both along and around the cuff. These devices displayed an improved selectivity, demonstrated by the stimulation of the FETi only under certain electrode combinations. Nevertheless, selective recording could not be achieved due to impedance issues and electrical noise.

Improving the selectivity while keeping the invasiveness of cuff electrodes low is an ongoing challenge for extraneural PNI. In the future, selectivity could be improved by increasing the number of electrodes while keeping their impedance low through the implementation of novel electrode materials.

6.3 Robustness and ease of implantation

Small nerves are delicate structures that benefit from equally soft electrodes to interface with them. If the Young's modulus between the nerve and the implant is large, there is a risk of nerve trauma during movement [129]. However, soft and small devices are also challenging to handle, which makes practitioners prefer more traditional approaches.

I attempted to improve the mechanical mismatch by using softer substrates but still robust enough to facilitate their handling and implantation. The PDMS cuff was a satisfactory attempt as both silicone and the metal had their own stiffness, which make the handling and implantation straightforward. This model was then improved with the 3D-printed electrodes, which had a smaller aspect ratio and featured a softer cuff and thinner metal conductors. However, stretchability and flexibility are important for implants because nerves are elastic structures that accommodate joint movement. That is why I also characterized flexible electrodes such as the self-folding and pre-folded devices (Chapter 5).

All in all, all the presented electrodes are straightforward to implant. However, the devices with thicker metal structures are easier to handle because they present a more rigid structure. The parylene-C device, while easy to implant and extract, presented challenges with handling, as well as the chitosan-based device. The best compromise between flexibility and ease of implantation comes from the self-folding structure, which presents a rigid but flexible resin substrate. This device can also be handled more freely and reused several times, showing great robustness.

6.4 Comparison of the different devices

To finish the comparison, I summarize the features of the different electrodes in table Table 6.1. “High”, “Medium” and “Low” grade the suitability of each electrode for the specific purpose. If the characterization has not been done, it is symbolized with “—”.

In the future, a device that connects the electrodes to a small processing unit, reads the signature of a nerve, processes its signals and produces a stimulating pattern that modulates the locust jump could be developed. The relatively large size of the locust could be further leveraged to develop a wireless, portable, closed-loop neuromodulation system. Such a closed-loop modulation strategy was shown in Chapter 3 but, in this case, the feedback loop was implemented externally.

Table 6.1: Comparison of the different devices presented in this thesis.

	Hooks	Mold-fabricated PDMS cuffs	3D-Printed	Self-folding	Pre-folded
Number of electrodes	2	2	4	6	6 & 15
Ease of handling	High	High	Medium	High	Medium
Recording selectivity	Low	Low	Medium	Medium	Medium
Recording SNR	Low	Low	Low	Medium	Low
Stimulation efficiency	High	High	Medium	High	High
Chronic implantation and survival rate	—	—	—	High	High

Totally-neural forward and feedback loops could improve the state of the art for the field of neural prostheses, endowing them with a more natural perception feeling [186, 187].

Bibliography

1. Deep Knowledge Analytics - NeuroTech Division: *NeuroTech Global Industry Landscape Overview 2019*. URL: `http://analytics.dkv.global/data/pdf/NeuroTech/NeuroTech-Landscape-Overview-Teaser.pdf` (visited on 11/05/2022) (cit. on p. 2).
2. NeuroTech Analytics: *NeuroTech Industry - Global NeuroTech Industry Investment Digest 2021*. URL: `http://analytics.neurotech.com/neurotech-investment-digest.pdf` (visited on 11/05/2022) (cit. on p. 2).
3. Nayak, Raghavendra and Ratan K. Banik: 'Current Innovations in Peripheral Nerve Stimulation'. *Pain Research and Treatment* (Sept. 13, 2018), vol. 2018: pp. 1–5 (cit. on p. 3).
4. Alexander, S. and D. Rowan: 'Electrical Control of Urinary Incontinence by Radio Implant. A Report of 14 Patients'. *British Journal of Surgery* (May 1968), vol. 55(5): pp. 358–364 (cit. on p. 3).
5. Judson, John P.: 'Radio-Frequency Electrophrenic Respiration: Long-Term Application to a Patient With Primary Hypoventilation'. *JAMA* (Mar. 18, 1968), vol. 203(12): p. 1033 (cit. on p. 3).

6. Guiraud, David et al.: 'Vagus Nerve Stimulation: State of the Art of Stimulation and Recording Strategies to Address Autonomic Function Neuromodulation'. *Journal of Neural Engineering* (Aug. 1, 2016), vol. 13(4): p. 041002 (cit. on pp. 3, 44).
7. Zabara, Jacob: 'Peripheral Control of Hypersynchronous Discharge in Epilepsy'. *Electroencephalography and Clinical Neurophysiology* (1985), vol. 61 (cit. on p. 3).
8. Afra, Pegah, Bola Adamolekun, Seyhmus Aydemir, and Glenn David Robert Watson: 'Evolution of the Vagus Nerve Stimulation (VNS) Therapy System Technology for Drug-Resistant Epilepsy'. *Frontiers in Medical Technology* (Aug. 26, 2021), vol. 3: p. 696543 (cit. on p. 3).
9. Lv, Hang, Yan-hua Zhao, Jian-guo Chen, Dong-yan Wang, and Hao Chen: 'Vagus Nerve Stimulation for Depression: A Systematic Review'. *Frontiers in Psychology* (Jan. 31, 2019), vol. 10: p. 64 (cit. on p. 3).
10. Johnson, Rhaya L. and Christopher G. Wilson: 'A Review of Vagus Nerve Stimulation as a Therapeutic Intervention'. *Journal of Inflammation Research* (May 2018), vol. Volume 11: pp. 203–213 (cit. on pp. 3, 42).
11. Yao, Guang, Lei Kang, Jun Li, Yin Long, Hao Wei, Carolina A. Ferreira, Justin J. Jeffery, Yuan Lin, Weibo Cai, and Xudong Wang: 'Effective Weight Control via an Implanted Self-Powered Vagus Nerve Stimulation Device'. *Nature Communications* (Dec. 2018), vol. 9(1): p. 5349 (cit. on p. 3).

12. Koopman, Frieda A., Sangeeta S. Chavan, Sanda Miljko, Simeon Grazio, Sekib Sokolovic, P. Richard Schuurman, Ashesh D. Mehta, Yaakov A. Levine, Michael Faltys, Ralph Zitnik, Kevin J. Tracey, and Paul P. Tak: ‘Vagus Nerve Stimulation Inhibits Cytokine Production and Attenuates Disease Severity in Rheumatoid Arthritis’. *Proceedings of the National Academy of Sciences* (July 19, 2016), vol. 113(29): p. 8284 (cit. on p. 3).

13. Staats, Peter, Georgios Giannakopoulos, Justyna Blake, Eric Liebler, and Robert M. Levy: ‘The Use of Non-invasive Vagus Nerve Stimulation to Treat Respiratory Symptoms Associated With COVID -19: A Theoretical Hypothesis and Early Clinical Experience’. *Neuromodulation: Technology at the Neural Interface* (Aug. 2020), vol. 23(6): pp. 784–788 (cit. on pp. 3, 42).

14. Larson, Christopher E. and Ellis Meng: ‘A Review for the Peripheral Nerve Interface Designer’. *Journal of Neuroscience Methods* (Feb. 2020), vol. 332: p. 108523 (cit. on pp. 3, 15).

15. Paggi, Valentina, Outman Akouissi, Silvestro Micera, and Stéphanie P Lacour: ‘Compliant Peripheral Nerve Interfaces’. *Journal of Neural Engineering* (June 1, 2021), vol. 18(3): p. 031001 (cit. on pp. 3, 83).

16. Carnicer-Lombarte, Alejandro, Shao-Tuan Chen, George G. Malliaras, and Damiano G. Barone: ‘Foreign Body Reaction to Implanted Biomaterials and Its Impact in Nerve Neuroprosthetics’. *Frontiers*

in Bioengineering and Biotechnology (Apr. 15, 2021), vol. 9: p. 622524 (cit. on p. 4).

17. Navarro, Xavier, Thilo B. Krueger, Natalia Lago, Silvestro Micera, Thomas Stieglitz, and Paolo Dario: ‘A Critical Review of Interfaces with the Peripheral Nervous System for the Control of Neuroprostheses and Hybrid Bionic Systems’. *Journal of the Peripheral Nervous System* (2005), vol. 10(3): pp. 229–258 (cit. on pp. 4, 17, 19).

18. Ortiz-Catalan, Max, Rickard Brånemark, Bo Håkansson, and Jean Delbeke: ‘On the Viability of Implantable Electrodes for the Natural Control of Artificial Limbs: Review and Discussion’. *BioMedical Engineering OnLine* (2012), vol. 11(1): p. 33 (cit. on p. 4).

19. Tyler, Dustin J. and Dominique M. Durand: ‘Functionally Selective Peripheral Nerve Stimulation with a Flat Interface Nerve Electrode’. *IEEE Transactions on Neural Systems and Rehabilitation Engineering* (2002), vol. 10(4): pp. 294–303 (cit. on pp. 4, 20).

20. Leventhal, Daniel K. and Dominique M. Durand: ‘Subfascicle Stimulation Selectivity with the Flat Interface Nerve Electrode’. *Annals of Biomedical Engineering* (June 2003), vol. 31(6): pp. 643–652 (cit. on p. 4).

21. Tan, Daniel W., Matthew A. Schiefer, Michael W. Keith, J. Robert Anderson, and Dustin J. Tyler: ‘Stability and Selectivity of a Chronic, Multi-Contact Cuff Electrode for Sensory Stimulation in Human Amputees’. *Journal of Neural Engineering* (Apr. 1, 2015), vol. 12(2): p. 026002 (cit. on p. 4).

22. Brill, N. A., S. N. Naufel, K. Polasek, C. Ethier, J Cheesborough, S. Agnew, L. E. Miller, and D. J. Tyler: 'Evaluation of High-Density, Multi-Contact Nerve Cuffs for Activation of Grasp Muscles in Monkeys'. *Journal of Neural Engineering* (June 1, 2018), vol. 15(3): p. 036003 (cit. on p. 4).

23. Silveira, Carolina, Emma Brunton, Sally Spendiff, and Kianoush Nazarpour: 'Influence of Nerve Cuff Channel Count and Implantation Site on the Separability of Afferent ENG'. *Journal of Neural Engineering* (Aug. 1, 2018), vol. 15(4): p. 046004 (cit. on p. 4).

24. Elyahoodayan, Sahar, Christopher Larson, Angelica M. Cobo, Ellis Meng, and Dong Song: 'Acute in Vivo Testing of a Polymer Cuff Electrode with Integrated Microfluidic Channels for Stimulation, Recording, and Drug Delivery on Rat Sciatic Nerve'. *Journal of neuroscience methods* (2020), vol. 336: p. 108634 (cit. on p. 4).

25. Koh, Ryan G. L., Michael Balas, Adrian I. Nachman, and José Zariffa: 'Selective Peripheral Nerve Recordings from Nerve Cuff Electrodes Using Convolutional Neural Networks'. *Journal of Neural Engineering* (Jan. 31, 2020), vol. 17(1): p. 016042 (cit. on pp. 4, 75).

26. Birk, D.M., D. Yin, and K.V. Slavin: 'Regulation of Peripheral Nerve Stimulation Technology'. *Progress in Neurological Surgery*. Vol. 29. 2016: pp. 225–237 (cit. on p. 4).

27. Rowan, Cami C., Oliver Graudejus, and Timothy M. Otchy: 'A Microclip Peripheral Nerve Interface (μcPNI) for Bioelectronic Interfacing

with Small Nerves'. *Advanced Science* (Jan. 2022), vol. 9(3): p. 2102945 (cit. on pp. 4, 60).

28. Shi, Yue, Ruping Liu, Liang He, Hongqing Feng, Ye Li, and Zhou Li: 'Recent Development of Implantable and Flexible Nerve Electrodes'. *Smart Materials in Medicine* (2020), vol. 1: pp. 131–147 (cit. on pp. 4, 59).

29. Decataldo, Francesco, Tobias Cramer, Davide Martelli, Isacco Gualandi, Willian S. Korim, Song T. Yao, Marta Tessarolo, Mauro Murgia, Erika Scavetta, Roberto Amici, and Beatrice Fraboni: 'Stretchable Low Impedance Electrodes for Bioelectronic Recording from Small Peripheral Nerves'. *Scientific Reports* (Dec. 2019), vol. 9(1): p. 10598 (cit. on pp. 4, 83).

30. González-González, María A., Aswini Kanneganti, Alexandra Joshi-Imre, Ana G. Hernandez-Reynoso, Geetanjali Bendale, Romil Modi, Melanie Ecker, Ali Khurram, Stuart F. Cogan, Walter E. Voit, and Mario I. Romero-Ortega: 'Thin Film Multi-Electrode Softening Cuffs for Selective Neuromodulation'. *Scientific Reports* (Dec. 2018), vol. 8(1): p. 16390 (cit. on pp. 4, 59).

31. Xiang, Zhuolin, Shih-Cheng Yen, Swathi Sheshadri, Jiahui Wang, Sanghoon Lee, Yu-Hang Liu, Lun-De Liao, Nitish V. Thakor, and Chengkuo Lee: 'Progress of Flexible Electronics in Neural Interfacing – A Self-Adaptive Non-Invasive Neural Ribbon Electrode for Small Nerves Recording'. *Advanced Materials* (June 1, 2016), vol. 28(22): pp. 4472–4479 (cit. on pp. 4, 20, 83).

32. Kandel, Eric R., James H. Schwartz, Thomas M. Jessell, Steven Siegelbaum, A. James Hudspeth, and Sarah Mack: *Principles of Neural Science*. Vol. 4. McGraw-hill New York, 2000 (cit. on pp. 8, 11, 13).

33. Sunderland, Sir Sydney: 'The Anatomy and Physiology of Nerve Injury'. *Muscle & Nerve* (Sept. 1990), vol. 13(9): pp. 771–784 (cit. on p. 9).

34. Horch, Kenneth W. and Daryl R. Kipke: *Neuroprosthetics: Theory and Practice*. Vol. 8. World Scientific, 2017 (cit. on pp. 9, 13).

35. Squire, Larry, Nicholas C. Spitzer, Darwin Berg, Floyd E. Bloom, Sascha du Lac, and Anirvan Ghosh: *Fundamental Neuroscience*. Academic press, 2012 (cit. on p. 11).

36. Hodgkin, A. L. and A. F. Huxley: 'A Quantitative Description of Membrane Current and Its Application to Conduction and Excitation in Nerve.' *The Journal of physiology* (Aug. 1952), vol. 117(4): pp. 500–544 (cit. on p. 11).

37. Dayan, Peter and L. F. Abbott: *Theoretical Neuroscience: Computational and Mathematical Modeling of Neural Systems*. Computational Neuroscience. Cambridge, Mass: Massachusetts Institute of Technology Press, 2001. 460 pp. (cit. on p. 11).

38. Zhao, Y., S. Inayat, D. A. Dikin, J. H. Singer, R. S. Ruoff, and J. B. Troy: 'Patch Clamp Technique: Review of the Current State of the Art and Potential Contributions from Nanoengineering'. *Proceedings of the*

Institution of Mechanical Engineers, Part N: Journal of Nanoengineering and Nanosystems (Mar. 1, 2008), vol. 222(1): pp. 1–11 (cit. on p. 13).

39. Loeb, G.E. and R.A. Peck: 'Cuff Electrodes for Chronic Stimulation and Recording of Peripheral Nerve Activity'. *Journal of Neuroscience Methods* (Jan. 1996), vol. 64(1): pp. 95–103 (cit. on pp. 15, 20).

40. Carter, Matt, Rachel Essner, Nitsan Goldstein, and Manasi Iyer: *Guide to Research Techniques in Neuroscience.* Third edition. London San Diego, CA Cambridge, MA Oxford: Academic Press, an imprint of Elsevier, 2022. 394 pp. (cit. on p. 15).

41. Eggers, Thomas E., Yazan M. Dweiri, Grant A. McCallum, and Dominique M. Durand: 'Model-Based Bayesian Signal Extraction Algorithm for Peripheral Nerves'. *Journal of Neural Engineering* (Oct. 1, 2017), vol. 14(5): p. 056009 (cit. on p. 15).

42. Koole, P., J. Holsheimer, J.J. Struijk, and A.J. Verloop: 'Recruitment Characteristics of Nerve Fascicles Stimulated by a Multigroove Electrode'. *IEEE Transactions on Rehabilitation Engineering* (Mar. 1997), vol. 5(1): pp. 40–50 (cit. on p. 18).

43. Tyler, D.J. and D.M. Durand: 'A Slowly Penetrating Interfascicular Nerve Electrode for Selective Activation of Peripheral Nerves'. *IEEE Transactions on Rehabilitation Engineering* (Mar. 1997), vol. 5(1): pp. 51–61 (cit. on p. 18).

44. Kundu, Aritra, Kristian Rauhe Harreby, Ken Yoshida, Tim Boretius, Thomas Stieglitz, and Winnie Jensen: 'Stimulation Selectivity

of the “Thin-Film Longitudinal Intrafascicular Electrode” (tfLIFE) and the “Transverse Intrafascicular Multi-Channel Electrode” (TIME) in the Large Nerve Animal Model’. *IEEE Transactions on Neural Systems and Rehabilitation Engineering* (Mar. 2014), vol. 22(2): pp. 400–410 (cit. on p. 18).

45. Jung, Ranu, James J. Abbas, Sathyakumar Kuntaegowdanahalli, and Anil K. Thota: ‘Bionic Intrafascicular Interfaces for Recording and Stimulating Peripheral Nerve Fibers’. *Bioelectronics in Medicine* (Jan. 2018), vol. 1(1): pp. 55–69 (cit. on p. 18).

46. Grill, Warren M., Sharon E. Norman, and Ravi V. Bellamkonda: ‘Implanted Neural Interfaces: Biochallenges and Engineered Solutions’. *Annual Review of Biomedical Engineering* (Aug. 1, 2009), vol. 11(1): pp. 1–24 (cit. on p. 18).

47. Rijnbeek, Emil H., Nick Eleveld, and Wouter Olthuis: ‘Update on Peripheral Nerve Electrodes for Closed-Loop Neuroprosthetics’. *Frontiers in Neuroscience* (May 28, 2018), vol. 12: p. 350 (cit. on p. 18).

48. Agnew, William F. and Douglas B. McCreery: ‘Considerations for Safety with Chronically Implanted Nerve Electrodes’. *Epilepsia* (1990), vol. 31: S27–S32 (cit. on p. 18).

49. Lago, Natalia, Ken Yoshida, Klaus P. Koch, and Xavier Navarro: ‘Assessment of Biocompatibility of Chronically Implanted Polyimide and Platinum Intrafascicular Electrodes’. *IEEE Transactions on Biomedical Engineering* (Feb. 2007), vol. 54(2): pp. 281–290 (cit. on p. 18).

50. Malagodi, Mark S., Kenneth W. Horch, and Andrew A. Schoenberg: 'An Intrafascicular Electrode for Recording of Action Potentials in Peripheral Nerves'. *Annals of Biomedical Engineering* (July 1989), vol. 17(4): pp. 397–410 (cit. on p. 18).

51. Yoshida, K., K. Hennings, and S. Kammer: 'Acute Performance of the Thin-Film Longitudinal Intra-Fascicular Electrode'. *The First IEEE/RAS-EMBS International Conference on Biomedical Robotics and Biomechatronics, 2006. BioRob 2006.* The First IEEE/RAS-EMBS International Conference on Biomedical Robotics and Biomechatronics, 2006. BioRob 2006. Pisa, Italy: IEEE, 2006: pp. 296–300 (cit. on p. 18).

52. Boretius, Tim, Jordi Badia, Aran Pascual-Font, Martin Schuettler, Xavier Navarro, Ken Yoshida, and Thomas Stieglitz: 'A Transverse Intrafascicular Multichannel Electrode (TIME) to Interface with the Peripheral Nerve'. *Biosensors and Bioelectronics* (Sept. 15, 2010), vol. 26(1): pp. 62–69 (cit. on pp. 18, 58, 82).

53. Badia, Jordi, Tim Boretius, David Andreu, Christine Azevedo-Coste, Thomas Stieglitz, and Xavier Navarro: 'Comparative Analysis of Transverse Intrafascicular Multichannel, Longitudinal Intrafascicular and Multipolar Cuff Electrodes for the Selective Stimulation of Nerve Fascicles'. *Journal of Neural Engineering* (June 1, 2011), vol. 8(3): p. 036023 (cit. on p. 18).

54. Cutrone, A., J. Del Valle, D. Santos, J. Badia, C. Filippeschi, S. Micera, X. Navarro, and S. Bossi: 'A Three-Dimensional Self-Opening

Intraneural Peripheral Interface (SELINE)'. *Journal of Neural Engineering* (Feb. 1, 2015), vol. 12(1): p. 016016 (cit. on p. 18).

55. Branner, Almut and Richard Alan Normann: 'A Multielectrode Array for Intrafascicular Recording and Stimulation in Sciatic Nerve of Cats'. *Brain Research Bulletin* (Mar. 2000), vol. 51(4): pp. 293–306 (cit. on p. 18).

56. Coker, Robert A., Erik R. Zellmer, and Daniel W. Moran: 'Micro-Channel Sieve Electrode for Concurrent Bidirectional Peripheral Nerve Interface. Part A: Recording'. *Journal of Neural Engineering* (Apr. 1, 2019), vol. 16(2): p. 026001 (cit. on p. 19).

57. MacEwan, Matthew R., Erik R. Zellmer, Jesse J. Wheeler, Harold Burton, and Daniel W. Moran: 'Regenerated Sciatic Nerve Axons Stimulated through a Chronically Implanted Macro-Sieve Electrode'. *Frontiers in Neuroscience* (Dec. 8, 2016), vol. 10 (cit. on p. 19).

58. Günter, Clara, Jean Delbeke, and Max Ortiz-Catalan: 'Safety of Long-Term Electrical Peripheral Nerve Stimulation: Review of the State of the Art'. *Journal of neuroengineering and rehabilitation* (2019), vol. 16(1): pp. 1–16 (cit. on p. 20).

59. Zhang, Yingchao et al.: 'Climbing-Inspired Twining Electrodes Using Shape Memory for Peripheral Nerve Stimulation and Recording'. *Science Advances* (Apr. 2019), vol. 5(4): eaaw1066 (cit. on pp. 20, 83).

60. Brindley, G. S.: ‘An Implant to Empty the Bladder or Close the Urethra.’ *Journal of Neurology, Neurosurgery & Psychiatry* (Apr. 1, 1977), vol. 40(4): pp. 358–369 (cit. on p. 20).

61. Helmholtz, H.: ‘Studien über electrische Grenzschichten’. *Annalen der Physik und Chemie* (1879), vol. 243(7): pp. 337–382 (cit. on p. 21).

62. Kirby, Brian J.: *Micro- and Nanoscale Fluid Mechanics: Transport in Microfluidic Devices*. 2010 (cit. on pp. 22, 24).

63. Bard, Allen J., Larry R. Faulkner, and Henry S. White: *Electrochemical Methods*. 3rd ed. 2022 (cit. on pp. 24, 25).

64. Elgrishi, Noémie, Kelley J. Rountree, Brian D. McCarthy, Eric S. Rountree, Thomas T. Eisenhart, and Jillian L. Dempsey: ‘A Practical Beginner’s Guide to Cyclic Voltammetry’. *Journal of Chemical Education* (Feb. 13, 2018), vol. 95(2): pp. 197–206 (cit. on pp. 25, 26).

65. Cogan, Stuart F.: ‘Neural Stimulation and Recording Electrodes’. *Annual Review of Biomedical Engineering* (Aug. 1, 2008), vol. 10(1): pp. 275–309 (cit. on pp. 28, 30).

66. Rozman, Janez, Polona Pečlin, Andraž Mehle, and Martin Šala: ‘Electrochemical Performance of Platinum Electrodes within the Multi-Electrode Spiral Nerve Cuff’. *Australasian Physical & Engineering Sciences in Medicine* (Sept. 2014), vol. 37(3): pp. 525–533 (cit. on p. 28).

67. Gong, Cihun-Siyong, Wun-Jia Syu, Kin Lei, and Yih-Shiou Hwang: 'Development of a Flexible Non-Metal Electrode for Cell Stimulation and Recording'. *Sensors* (Sept. 29, 2016), vol. 16(10): p. 1613 (cit. on p. 28).

68. Cisnal, Ana, Frank R. R. Ihmig, Juan-Carlos Fraile, Javier Pérez-Turiel, and Víctor Muñoz-Martinez: 'Application of a Novel Measurement Setup for Characterization of Graphene Microelectrodes and a Comparative Study of Variables Influencing Charge Injection Limits of Implantable Microelectrodes'. *Sensors* (June 17, 2019), vol. 19(12): p. 2725 (cit. on p. 28).

69. Dick, Paul: 'Sensory Coding of Complex Visual Motion in the Locust (Locusta Migratoria)'. University of Saskatchewan, 2013 (cit. on p. 33).

70. Rasband, Wayne S.: 'National Institutes of Health, Bethesda, Maryland, USA'. *http://imagej. nih. gov/ij/* (2011), vol. (cit. on p. 35).

71. Chapman, R. F., Stephen J. Simpson, and A. E. Douglas: *The Insects: Structure and Function*. Fifth edition. New York: Cambridge University Press, 2013. 929 pp. (cit. on pp. 34, 36, 37).

72. Carlson, Stanley D. and Richard L. Saint Marie: 'Structure and Function of Insect Glia'. *Annual review of entomology* (1990), vol. 35(1): pp. 597–621 (cit. on p. 36).

73. Huber, Franz: 'Neural Integration (Central Nervous System)'. *The Physiology of Insecta*. Elsevier, 1974: pp. 3–100 (cit. on p. 36).

74. Burrows, Malcolm: ‘The Neurobiology of an Insect Brain’. (1996), vol. (cit. on pp. 36, 93).

75. Hoyle, G.: ‘The Anatomy and Innervation of Locust Skeletal Muscle’. *Proceedings of the Royal Society of London. Series B-Biological Sciences* (1955), vol. 143(911): pp. 281–292 (cit. on pp. 38, 75).

76. Pfahlert, Carsten and Reinhard Lakes-Harlan: ‘Thoracic Interneurons, Motorneurons and Sensory Neurons of Locusta Migratoria (Insecta: Orthoptera) in Primary Cell Culture’. *The Open Entomology Journal* (Oct. 13, 2008), vol. 2(1): pp. 6–13 (cit. on p. 38).

77. Matheson, Thomas and Laurence H. Field: ‘An Elaborate Tension Receptor System Highlights Sensory Complexity in the Hind Leg of the Locust’. *Journal of Experimental Biology* (Aug. 1, 1995), vol. 198(8): pp. 1673–1689 (cit. on p. 38).

78. Burrows, M.: ‘Motor Patterns during Kicking Movements in the Locust’. *Journal of Comparative Physiology A* (1995), vol. 176(3) (cit. on p. 38).

79. Cook, P. M.: ‘Observations on Giant Fibres of the Nervous System’. (1951), vol. (cit. on p. 38).

80. Banks, Daniel John: ‘Modelling Studies on Peripheral Nerve Neural Signal Transduction Using Thin-Film Microelectrodes’. University of Surrey (United Kingdom), 1994 (cit. on p. 38).

81. Groiss, S.J., L. Wojtecki, M. Südmeyer, and A. Schnitzler: 'Review: Deep Brain Stimulation in Parkinson's Disease'. *Therapeutic Advances in Neurological Disorders* (Nov. 2009), vol. 2(6): pp. 379–391 (cit. on p. 42).

82. Delaloye, Sibylle and Paul E. Holtzheimer: 'Deep Brain Stimulation in the Treatment of Depression'. *Clinical research* (2014), vol. 16(1): p. 9 (cit. on p. 42).

83. Aaronson, Scott T., Peter Sears, Francis Ruvuna, Mark Bunker, Charles R. Conway, Darin D. Dougherty, Frederick W. Reimherr, Thomas L. Schwartz, and John M. Zajecka: 'A 5-Year Observational Study of Patients With Treatment-Resistant Depression Treated With Vagus Nerve Stimulation or Treatment as Usual: Comparison of Response, Remission, and Suicidality'. *American Journal of Psychiatry* (July 2017), vol. 174(7): pp. 640–648 (cit. on p. 42).

84. González, Hernán F.J., Aaron Yengo-Kahn, and Dario J. Englot: 'Vagus Nerve Stimulation for the Treatment of Epilepsy'. *Neurosurgery Clinics of North America* (Apr. 2019), vol. 30(2): pp. 219–230 (cit. on p. 42).

85. Gold, Michael R., Dirk J. Van Veldhuisen, Paul J. Hauptman, Martin Borggrefe, Spencer H. Kubo, Randy A. Lieberman, Goran Milasinovic, Brett J. Berman, Sanja Djordjevic, Suresh Neelagaru, Peter J. Schwartz, Randall C. Starling, and Douglas L. Mann: 'Vagus Nerve Stimulation for the Treatment of Heart Failure'. *Journal of the American College of Cardiology* (July 2016), vol. 68(2): pp. 149–158 (cit. on p. 42).

86. Bhide, Alka A., Visha Tailor, Ruwan Fernando, Vik. Khullar, and Giuseppe Alessandro Digesu: 'Posterior Tibial Nerve Stimulation for Overactive Bladder—Techniques and Efficacy'. *International Urogynecology Journal* (May 2020), vol. 31(5): pp. 865–870 (cit. on p. 42).

87. Gibson, William, Benedict M. Wand, Catherine Meads, Mark J. Catley, and Neil E. O'Connell: 'Transcutaneous Electrical Nerve Stimulation (TENS) for Chronic Pain - an Overview of Cochrane Reviews'. *Cochrane Database of Systematic Reviews* (Apr. 3, 2019), vol. Ed. by Cochrane Pain, Palliative and Supportive Care Group (cit. on p. 42).

88. Bahmer, Andreas, Youssef Adel, and Uwe Baumann: 'Preventing Facial Nerve Stimulation by Triphasic Pulse Stimulation in Cochlear Implant Users: Intraoperative Recordings'. *Otology & Neurotology* (2017), vol. 38(10): e438–e444 (cit. on p. 42).

89. Nicol, D. J., M. H. Granat, S. J. M. Tuson, and R. H. Baxendale: 'Variability of the Dishabituation of Flexion Reflexes for FES Assisted Gait in Spinal Injured Man'. *Medical engineering & physics* (1998), vol. 20(3): pp. 182–187 (cit. on p. 43).

90. J. Kljajic, G. Valle, and S. Raspopovic: 'Modeling Sensory Adaptation to Peripheral Nerve Stimulation'. *2021 10th International IEEE/EMBS Conference on Neural Engineering (NER).* 2021 10th International IEEE/EMBS Conference on Neural Engineering (NER). May 4–6, 2021: pp. 788–791 (cit. on p. 43).

91. Zbrzeski, Adeline, Yannick Bornat, Brian Hillen, Ricardo Siu, James Abbas, Ranu Jung, and Sylvie Renaud: ‘Bio-Inspired Controller on an FPGA Applied to Closed-Loop Diaphragmatic Stimulation’. *Frontiers in Neuroscience* (June 16, 2016), vol. 10 (cit. on p. 43).

92. Rotermund, David, Udo A. Ernst, and Klaus R. Pawelzik: ‘Open Hardware for Neuro-Prosthesis Research: A Study about a Closed-Loop Multi-Channel System for Electrical Surface Stimulations and Measurements’. *HardwareX* (Oct. 2019), vol. 6: e00078 (cit. on p. 43).

93. Romero-Ugalde, Hector M., Virginie Le Rolle, Jean-Luc Bonnet, Christine Henry, Philippe Mabo, Guy Carrault, and Alfredo I. Hernandez: ‘Closed-Loop Vagus Nerve Stimulation Based on State Transition Models’. *IEEE Transactions on Biomedical Engineering* (July 2018), vol. 65(7): pp. 1630–1638 (cit. on p. 43).

94. Cork, Simon C., Amir Eftekhar, Khalid B. Mirza, Claudio Zuliani, Konstantin Nikolic, James V. Gardiner, Stephen R. Bloom, and Christofer Toumazou: ‘Extracellular pH Monitoring for Use in Closed-Loop Vagus Nerve Stimulation’. *Journal of Neural Engineering* (Feb. 1, 2018), vol. 15(1): p. 016001 (cit. on p. 43).

95. Wright, James, Vaughan G. Macefield, André van Schaik, and Jonathan C. Tapson: ‘A Review of Control Strategies in Closed-Loop Neuroprosthetic Systems’. *Frontiers in Neuroscience* (July 12, 2016), vol. 10: p. 312 (cit. on p. 43).

96. Lozano, Andres M. and Mark T. Rise: *Method of Treating Movement Disorders by Electrical Stimulation and/or Drug Infusion of the Pendunulopontine Nucleus*. Google Patents, 2002 (cit. on p. 43).

97. Frank, Steven A.: *Control Theory Tutorial: Basic Concepts Illustrated by Software Examples*. SpringerBriefs in Applied Sciences and Technology. Cham: Springer International Publishing, 2018 (cit. on p. 43).

98. Sun, Felice T. and Martha J. Morrell: ‘Closed-Loop Neurostimulation: The Clinical Experience’. *Neurotherapeutics* (July 2014), vol. 11(3): pp. 553–563 (cit. on p. 43).

99. Kassiri, Hossein, Sana Tonekaboni, M. Tariqus Salam, Nima Soltani, Karim Abdelhalim, Jose Luis Perez Velazquez, and Roman Genov: ‘Closed-Loop Neurostimulators: A Survey and A Seizure-Predicting Design Example for Intractable Epilepsy Treatment’. *IEEE Transactions on Biomedical Circuits and Systems* (Oct. 2017), vol. 11(5): pp. 1026–1040 (cit. on p. 43).

100. Falcone, Jessica D., Tristan Liu, Laura Goldman, Pogue David D, Loren Rieth, Chad E. Bouton, Malgorzata Straka, and Harbaljit S. Sohal: ‘A Novel Microwire Interface for Small Diameter Peripheral Nerves in a Chronic, Awake Murine Model’. *Journal of Neural Engineering* (July 10, 2020), vol. 17(4): p. 046003 (cit. on p. 43).

101. Hernandez-Reynoso, Ana G., Shrenevas Nandam, Jonathan M. O’Brien, Aswini Kanneganti, Stuart F. Cogan, Daniel K. Freeman, and Mario I. Romero-Ortega: ‘Miniature Electroparticle-Cuff for Wireless

Peripheral Neuromodulation’. *Journal of Neural Engineering* (Aug. 1, 2019), vol. 16(4): p. 046002 (cit. on p. 43).

102. Liu, Xilin, Milin Zhang, Andrew G. Richardson, Timothy H. Lucas, and Jan Van der Spiegel: ‘Design of a Closed-Loop, Bidirectional Brain Machine Interface System With Energy Efficient Neural Feature Extraction and PID Control’. *IEEE Transactions on Biomedical Circuits and Systems* (Aug. 2017), vol. 11(4): pp. 729–742 (cit. on p. 43).

103. Das, Rupam, Farshad Moradi, and Hadi Heidari: ‘Biointegrated and Wirelessly Powered Implantable Brain Devices: A Review’. *IEEE Transactions on Biomedical Circuits and Systems* (Apr. 2020), vol. 14(2): pp. 343–358 (cit. on p. 43).

104. Charkhkar, Hamid, Courtney E. Shell, Paul D. Marasco, Gilles J. Pinault, Dustin J. Tyler, and Ronald J. Triolo: ‘High-Density Peripheral Nerve Cuffs Restore Natural Sensation to Individuals with Lower-Limb Amputations’. *Journal of Neural Engineering* (Oct. 1, 2018), vol. 15(5): p. 056002 (cit. on p. 43).

105. Lee, Byunghun, Mukhesh K. Koripalli, Yaoyao Jia, Joshua Acosta, M. S. E. Sendi, Yoonsu Choi, and Maysam Ghovanloo: ‘An Implantable Peripheral Nerve Recording and Stimulation System for Experiments on Freely Moving Animal Subjects’. *Scientific Reports* (Apr. 17, 2018), vol. 8(1): p. 6115 (cit. on p. 43).

106. Ghanbari, Mohammad Meraj, David K. Piech, Konlin Shen, Sina Faraji Alamouti, Cem Yalcin, Benjamin C. Johnson, Jose M.

Carmena, Michel M. Maharbiz, and Rikky Muller: ‘A Sub-mm ^{3} Ultrasonic Free-Floating Implant for Multi-Mote Neural Recording’. *IEEE Journal of Solid-State Circuits* (Nov. 2019), vol. 54(11): pp. 3017–3030 (cit. on p. 43).

107. Park, Hangue, Kyunggeune Oh, Boris I. Prilutsky, and Stephen P. DeWeerth: ‘A Real-Time Closed-Loop Control System for Modulating Gait Characteristics via Electrical Stimulation of Peripheral Nerves’. *2016 IEEE Biomedical Circuits and Systems Conference (BioCAS).* 2016 IEEE Biomedical Circuits and Systems Conference (BioCAS). Shanghai, China: IEEE, Oct. 2016: pp. 95–98 (cit. on p. 43).

108. Mickle, Aaron D. et al.: ‘A Wireless Closed-Loop System for Optogenetic Peripheral Neuromodulation’. *Nature* (Jan. 2019), vol. 565(7739): pp. 361–365 (cit. on p. 44).

109. Wenger, Nikolaus, Eduardo Martin Moraud, Stanisa Raspopovic, Marco Bonizzato, Jack DiGiovanna, Pavel Musienko, Manfred Morari, Silvestro Micera, and Grégoire Courtine: ‘Closed-Loop Neuromodulation of Spinal Sensorimotor Circuits Controls Refined Locomotion after Complete Spinal Cord Injury’. *Science translational medicine* (2014), vol. 6(255): 255ra133–255ra133 (cit. on p. 44).

110. Richards, Christopher T. and Enrico A. Eberhard: ‘*In Vitro-Virtual-Reality* : An Anatomically Explicit Musculoskeletal Simulation Powered by *in Vitro* Muscle Using Closed Loop Tissue-Software Interaction’. *Journal of Experimental Biology* (Jan. 1, 2020), vol.: jeb.210054 (cit. on p. 44).

111. Rubeo, Scott, Nicholas Szczecinski, and Roger Quinn: ‘A Synthetic Nervous System Controls a Simulated Cockroach’. *Applied Sciences* (Dec. 22, 2017), vol. 8(1): p. 6 (cit. on p. 44).

112. Naris, Mantas, Nicholas S. Szczecinski, and Roger D. Quinn: ‘A Neuromechanical Model Exploring the Role of the Common Inhibitor Motor Neuron in Insect Locomotion’. *Biological Cybernetics* (Feb. 2020), vol. 114(1): pp. 23–41 (cit. on p. 44).

113. Strohmer, Beck, Poramate Manoonpong, and Leon Bonde Larsen: ‘Flexible Spiking CPGs for Online Manipulation During Hexapod Walking’. *Frontiers in Neurorobotics* (June 26, 2020), vol. 14: p. 41 (cit. on p. 44).

114. Raspopovic, Stanisa, Giacomo Valle, and Francesco Maria Petrini: ‘Sensory Feedback for Limb Prostheses in Amputees’. *Nature Materials* (2021), vol. 20(7): pp. 925–939 (cit. on p. 44).

115. Schiefer, Matthew A., Katharine H. Polasek, Ronald J. Triolo, G. C. J. Pinault, and Dustin J. Tyler: ‘Selective Stimulation of the Human Femoral Nerve with a Flat Interface Nerve Electrode’. *Journal of neural engineering* (2010), vol. 7(2): p. 026006 (cit. on p. 44).

116. Cao, Feng, Chao Zhang, Tat Thang Vo Doan, Yao Li, Daniyal Haider Sangi, Jie Sheng Koh, Ngoc Anh Huynh, Mohamed Fareez Bin Aziz, Hao Yu Choo, Kazuo Ikeda, Pieter Abbeel, Michel M. Maharbiz, and Hirotaka Sato: ‘A Biological Micro Actuator: Graded and Closed-Loop Control of Insect Leg Motion by Electrical Stimulation of

Muscles'. *PLoS ONE* (Aug. 20, 2014), vol. 9(8). Ed. by Lazzari, Claudio R.: e105389 (cit. on p. 44).

117. Zhang, Chao, Feng Cao, Yao Li, and Hirotaka Sato: 'Fuzzy-Controlled Living Insect Legged Actuator'. *Sensors and Actuators A: Physical* (May 2016), vol. 242: pp. 182–194 (cit. on p. 44).

118. Robertson, R. Meldrum, Kristin E. Spong, and Phinyaphat Srithiphaphirom: 'Chill Coma in the Locust, Locusta Migratoria, Is Initiated by Spreading Depolarization in the Central Nervous System'. *Scientific Reports* (Dec. 2017), vol. 7(1): pp. 1–12 (cit. on pp. 49, 64, 86).

119. Luo, Zhicong and Ming-Dou Ker: 'A High-Voltage-Tolerant and Precise Charge-Balanced Neuro-Stimulator in Low Voltage CMOS Process'. *IEEE Transactions on Biomedical Circuits and Systems* (Dec. 2016), vol. 10(6): pp. 1087–1099 (cit. on p. 52).

120. Giménez, Pablo, Ken Mukai, Kinji Asaka, Kenji Hata, Hideaki Oike, and T.F. Otero: 'Capacitive and Faradic Charge Components in High-Speed Carbon Nanotube Actuator'. *Electrochimica Acta* (Jan. 2012), vol. 60: pp. 177–183 (cit. on p. 55).

121. Zhou, Andy, Samantha R. Santacruz, Benjamin C. Johnson, George Alexandrov, Ali Moin, Fred L. Burghardt, Jan M. Rabaey, Jose M. Carmena, and Rikky Muller: 'A Wireless and Artefact-Free 128-Channel Neuromodulation Device for Closed-Loop Stimulation and Recording in Non-Human Primates'. *Nature Biomedical Engineering* (Jan. 2019), vol. 3(1): pp. 15–26 (cit. on p. 55).

122. Overstreet, Cynthia K., Jonathan Cheng, and Edward W. Keefer: 'Fascicle Specific Targeting for Selective Peripheral Nerve Stimulation'. *Journal of Neural Engineering* (Nov. 11, 2019), vol. 16(6): p. 066040 (cit. on p. 55).

123. Lacour, Stéphanie P., James J. Fitzgerald, Natalia Lago, Edward Tarte, Stephen McMahon, and James Fawcett: 'Long Micro-Channel Electrode Arrays: A Novel Type of Regenerative Peripheral Nerve Interface'. *IEEE Transactions on Neural Systems and Rehabilitation Engineering* (Oct. 2009), vol. 17(5): pp. 454–460 (cit. on p. 58).

124. Gaillet, Vivien, Annarita Cutrone, Fiorenzo Artoni, Paola Vagni, Ariastity Mega Pratiwi, Sandra Alejandra Romero, Dario Lipucci Di Paola, Silvestro Micera, and Diego Ghezzi: 'Spatially Selective Activation of the Visual Cortex via Intraneural Stimulation of the Optic Nerve'. *Nature biomedical engineering* (2020), vol. 4(2): pp. 181–194 (cit. on pp. 58, 82).

125. Lotti, Fiorenza, Federico Ranieri, Gianluca Vadalà, Loredana Zollo, and Giovanni Di Pino: 'Invasive Intraneural Interfaces: Foreign Body Reaction Issues'. *Frontiers in neuroscience* (2017), vol. 11: p. 497 (cit. on pp. 58, 82).

126. Lienemann, Samuel, Johan Zötterman, Simon Farnebo, and Klas Tybrandt: 'Stretchable Gold Nanowire-Based Cuff Electrodes for Low-Voltage Peripheral Nerve Stimulation'. *Journal of Neural Engineering* (2021), vol. 18(4): p. 045007 (cit. on pp. 58, 83).

127. Lee, Sanghoon, Wendy Yen Xian Peh, Nitish V. Thakor, Shih-Cheng Yen, and Chengkuo Lee: 'Vagus Nerve Stimulation (VNS) for Heart Rate Control Using Novel Neural Interfaces'. *2017 19th International Conference on Solid-State Sensors, Actuators and Microsystems (TRANSDUCERS).* 2017 19th International Conference on Solid-State Sensors, Actuators and Microsystems (TRANSDUCERS). Kaohsiung, Taiwan: IEEE, June 2017: pp. 1730–1733 (cit. on p. 58).

128. Fitchett, Adam, Svetlana Mastitskaya, and Kirill Aristovich: 'Selective Neuromodulation of the Vagus Nerve'. *Frontiers in Neuroscience* (May 24, 2021), vol. 15: p. 685872 (cit. on p. 58).

129. Bettinger, Christopher J.: 'Recent Advances in Materials and Flexible Electronics for Peripheral Nerve Interfaces'. *Bioelectronic Medicine* (Dec. 2018), vol. 4(1): p. 6 (cit. on pp. 58, 59, 109).

130. Ngan, Catherine G.Y., Rob M.I. Kapsa, and Peter F.M. Choong: 'Strategies for Neural Control of Prosthetic Limbs: From Electrode Interfacing to 3D Printing'. *Materials* (June 14, 2019), vol. 12(12): p. 1927 (cit. on p. 59).

131. Erben, Amelie et al.: 'Precision 3D-Printed Cell Scaffolds Mimicking Native Tissue Composition and Mechanics'. *Advanced Healthcare Materials* (Dec. 1, 2020), vol. 9(24): p. 2000918 (cit. on p. 60).

132. K. Lee, D. Yang, S. H. Park, T. W. Lim, and R. H. Kim: 'Improvement of Spatial Resolution in Two-Photon Stereolithography'. *2006 International Symposium on Biophotonics, Nanophotonics and Metamaterials.* 2006

International Symposium on Biophotonics, Nanophotonics and Metamaterials. 16–Oct. 18, 2006: pp. 8–14 (cit. on p. 60).

133. Gillis, Winthrop F., Charles A. Lissandrello, Jun Shen, Ben W. Pearre, Alket Mertiri, Felix Deku, Stuart Cogan, Bradley J. Holinski, Daniel J. Chew, Alice E. White, Timothy M. Otchy, and Timothy J. Gardner: 'Carbon Fiber on Polyimide Ultra-Microelectrodes'. *Journal of Neural Engineering* (Feb. 1, 2018), vol. 15(1): p. 016010 (cit. on p. 60).

134. Jang, Jongmoon, Jin-young Kim, Yeong Cheol Kim, Sangwon Kim, Namsun Chou, Seungmin Lee, Yun-Hoon Choung, Sohee Kim, Juergen Brugger, Hongsoo Choi, and Jeong Hun Jang: 'A 3D Microscaffold Cochlear Electrode Array for Steroid Elution'. *Advanced Healthcare Materials* (Oct. 2019), vol. 8(20): p. 1900379 (cit. on p. 60).

135. Yang, Cheng, Qun Cao, Pumidech Puthongkham, Scott T. Lee, Mallikarjunarao Ganesana, Nickolay V. Lavrik, and B. Jill Venton: '3D-Printed Carbon Electrodes for Neurotransmitter Detection'. *Angewandte Chemie International Edition* (Oct. 22, 2018), vol. 57(43): pp. 14255–14259 (cit. on p. 60).

136. Lissandrello, Charles A., Winthrop F. Gillis, Jun Shen, Ben W. Pearre, Flavia Vitale, Matteo Pasquali, Bradley J. Holinski, Daniel J. Chew, Alice E. White, and Timothy J. Gardner: 'A Micro-Scale Printable Nanoclip for Electrical Stimulation and Recording in

Small Nerves'. *Journal of Neural Engineering* (June 1, 2017), vol. 14(3): p. 036006 (cit. on p. 60).

137. Otchy, Timothy M., Christos Michas, Blaire Lee, Krithi Gopalan, Vidisha Nerurkar, Jeremy Gleick, Dawit Semu, Louis Darkwa, Bradley J. Holinski, Daniel J. Chew, Alice E. White, and Timothy J. Gardner: 'Printable Microscale Interfaces for Long-Term Peripheral Nerve Mapping and Precision Control'. *Nature Communications* (Dec. 2020), vol. 11(1): p. 4191 (cit. on pp. 60, 83).

138. Grob, Leroy, Philipp Rinklin, Sabine Zips, Dirk Mayer, Sabrina Weidlich, Korkut Terkan, Lennart J. K. Weiss, Nouran Adly, Andreas Offenhäusser, and Bernhard Wolfrum: 'Inkjet-Printed and Electroplated 3D Electrodes for Recording Extracellular Signals in Cell Culture'. *Sensors* (June 9, 2021), vol. 21(12): p. 3981 (cit. on pp. 62, 76).

139. Harischandra, Nalin, Anthony J. Clare, Jure Zakotnik, Laura M. L. Blackburn, Tom Matheson, and Volker Dürr: 'Evaluation of Linear and Non-Linear Activation Dynamics Models for Insect Muscle'. *PLOS Computational Biology* (Oct. 14, 2019), vol. 15(10). Ed. by Ayers, Joseph: e1007437 (cit. on p. 72).

140. Rattay, F.: 'The Basic Mechanism for the Electrical Stimulation of the Nervous System'. *Neuroscience* (Mar. 1999), vol. 89(2): pp. 335–346 (cit. on p. 72).

141. Grinberg, Yanina, Matthew A. Schiefer, Dustin J. Tyler, and Kenneth J. Gustafson: 'Fascicular Perineurium Thickness, Size, and

Position Affect Model Predictions of Neural Excitation'. *IEEE Transactions on Neural Systems and Rehabilitation Engineering* (Dec. 2008), vol. 16(6): pp. 572–581 (cit. on p. 73).

142. Aristovich, Kirill, Matteo Donega, Cathrine Fjordbakk, Ilya Tarotin, Christopher A.R. Chapman, Jaime Viscasillas, Thaleia-Rengina Stathopoulou, Abbe Crawford, Daniel Chew, Justin Perkins, and David Holder: 'Model-Based Geometrical Optimisation and in Vivo Validation of a Spatially Selective Multielectrode Cuff Array for Vagus Nerve Neuromodulation'. *Journal of Neuroscience Methods* (Mar. 2021), vol. 352: p. 109079 (cit. on p. 74).

143. Emad, Mohammad Reza, Leila Zeinali, Alireza Nikseresht, Mahshid Naseri, and Hajar Karimian: 'Peripheral Neuropathy in Multiple Sclerosis: An Electrophysiologic Study in Iranian Patients'. *Acta Medica Iranica* (2017), vol.: pp. 496–501 (cit. on p. 75).

144. Hoffer, Joaquín-Andrés and Klaus Kallesøe: 'How to Use Nerve Cuffs to Stimulate, Record or Modulate Neural Activity'. *Neural Prostheses for Restoration of Sensory and Motor Function*. Ed. by Chapin, John and Karen Moxon. Vol. 20005060. CRC Press, Sept. 27, 2000 (cit. on pp. 75, 106, 108).

145. Xu, Dongxin, Jingshan Mo, Xi Xie, and Ning Hu: 'In-Cell Nanoelectronics: Opening the Door to Intracellular Electrophysiology'. *Nano-Micro Letters* (Dec. 2021), vol. 13(1): p. 127 (cit. on p. 75).

146. Jones, Peter D., Anastasiya Moskalyuk, Clemens Barthold, Katja Gutöhrlein, Gerhard Heusel, Birgit Schröppel, Ramona Samba, and Michele Giugliano: 'Low-Impedance 3D PEDOT:PSS Ultramicroelectrodes'. *Frontiers in Neuroscience* (May 19, 2020), vol. 14: p. 405 (cit. on p. 75).

147. Criado-Gonzalez, Miryam, Antonio Dominguez-Alfaro, Naroa Lopez-Larrea, Nuria Alegret, and David Mecerreyes: 'Additive Manufacturing of Conducting Polymers: Recent Advances, Challenges, and Opportunities'. *ACS Applied Polymer Materials* (June 11, 2021), vol. 3(6): pp. 2865–2883 (cit. on p. 75).

148. Singh, Vinamrita and Tanuj Kumar: 'Study of Modified PEDOT:PSS for Tuning the Optical Properties of Its Conductive Thin Films'. *Journal of Science: Advanced Materials and Devices* (Dec. 1, 2019), vol. 4(4): pp. 538–543 (cit. on p. 75).

149. Donahue, Mary J., Christopher M. Proctor, and Xenofon Strakosas: 'Polymers/PEDOT Derivatives for Bioelectronics'. *Redox Polymers for Energy and Nanomedicine*. 2020: pp. 488–545 (cit. on p. 75).

150. Stříteský, Stanislav, Aneta Marková, Jan Víteček, Eva Šafaříková, Michal Hrabal, Lubomír Kubáč, Lukáš Kubala, Martin Weiter, and Martin Vala: 'Printing Inks of Electroactive Polymer PEDOT:PSS: The Study of Biocompatibility, Stability, and Electrical Properties: Electroactive Polymer PEDOT:PSS'. *Journal of Biomedical Materials Research Part A* (Apr. 2018), vol. 106(4): pp. 1121–1128 (cit. on p. 76).

151. Yan, Dongxiao, Ahmad A. Jiman, Elizabeth C. Bottorff, Paras R. Patel, Dilara Meli, Elissa J. Welle, David C. Ratze, Leif A. Havton, Cynthia A. Chestek, Stephen W. P. Kemp, Tim M. Bruns, Euisik Yoon, and John P. Seymour: 'Ultraflexible and Stretchable Intrafascicular Peripheral Nerve Recording Device with Axon-Dimension, Cuff-Less Microneedle Electrode Array'. *Small* (May 1, 2022), vol. 18(21): p. 2200311 (cit. on p. 82).

152. Renz, Aline F., Andreas M Reichmuth, Flurin Stauffer, Greta Thompson-Steckel, and Janos Vörös: 'A Guide towards Long-Term Functional Electrodes Interfacing Neuronal Tissue'. *Journal of Neural Engineering* (Dec. 1, 2018), vol. 15(6): p. 061001 (cit. on p. 82).

153. Christie, Breanne P., Max Freeberg, William D. Memberg, Gilles J. C. Pinault, Harry A. Hoyen, Dustin J. Tyler, and Ronald J. Triolo: '"Long-term Stability of Stimulating Spiral Nerve Cuff Electrodes on Human Peripheral Nerves"'. *Journal of NeuroEngineering and Rehabilitation* (Dec. 2017), vol. 14(1): p. 70 (cit. on p. 82).

154. Guo, Liang, ed.: *Neural Interface Engineering: Linking the Physical World and the Nervous System*. Cham: Springer International Publishing, 2020 (cit. on p. 82).

155. George, Jacob A., David M. Page, Tyler S. Davis, Christopher C. Duncan, Douglas T. Hutchinson, Loren W. Rieth, and Gregory A. Clark: 'Long-Term Performance of Utah Slanted Electrode Arrays and Intramuscular Electromyographic Leads Implanted Chronically in Human Arm

Nerves and Muscles'. *Journal of Neural Engineering* (Oct. 31, 2020), vol. 17(5): p. 056042 (cit. on p. 82).

156. Terkan, Korkut, Francisco Zurita, Touba Jamal Khalaf, Philipp Rinklin, Tetsuhiko Teshima, Tobias Kohl, and Bernhard Wolfrum: 'Soft Peripheral Nerve Interface Made from Carbon Nanotubes Embedded in Silicone'. *APL Materials* (Oct. 1, 2020), vol. 8(10): p. 101111 (cit. on p. 83).

157. Liu, Yuxin, Jia Liu, Shucheng Chen, Ting Lei, Yeongin Kim, Simiao Niu, Huiliang Wang, Xiao Wang, Amir M. Foudeh, Jeffrey B.-H. Tok, and Zhenan Bao: 'Soft and Elastic Hydrogel-Based Microelectronics for Localized Low-Voltage Neuromodulation'. *Nature Biomedical Engineering* (Jan. 8, 2019), vol. 3(1): pp. 58–68 (cit. on p. 83).

158. Afanasenkau, Dzmitry, Daria Kalinina, Vsevolod Lyakhovetskii, Christoph Tondera, Oleg Gorsky, Seyyed Moosavi, Natalia Pavlova, Natalia Merkulyeva, Allan V. Kalueff, Ivan R. Minev, and Pavel Musienko: 'Rapid Prototyping of Soft Bioelectronic Implants for Use as Neuromuscular Interfaces'. *Nature Biomedical Engineering* (Sept. 21, 2020), vol. 4(10): pp. 1010–1022 (cit. on p. 83).

159. Cobo, Angelica M., Christopher E. Larson, Kee Scholten, Jason A. Miranda, Sahar Elyahoodayan, Dong Song, Victor Pikov, and Ellis Meng: 'Parylene-Based Cuff Electrode With Integrated Microfluidics for Peripheral Nerve Recording, Stimulation, and Drug Delivery'. *Journal of Microelectromechanical Systems* (Feb. 2019), vol. 28(1): pp. 36–49 (cit. on p. 83).

160. Yu, Huaiqiang, Wenjie Xiong, Hongze Zhang, Wei Wang, and Zhihong Li: 'A Parylene Self-Locking Cuff Electrode for Peripheral Nerve Stimulation and Recording'. *Journal of Microelectromechanical Systems* (Oct. 2014), vol. 23(5): pp. 1025–1035 (cit. on p. 83).

161. Kim, Brian J. and Ellis Meng: 'Micromachining of Parylene C for bioMEMS: Micromachining of Parylene C for BioMEMS'. *Polymers for Advanced Technologies* (May 2016), vol. 27(5): pp. 564–576 (cit. on p. 83).

162. Tian, Pan, Wenwen Yi, Chaoyang Chen, Jie Hu, Jin Qi, Boshen Zhang, and Mark Ming-Cheng Cheng: 'Flexible 3D Carbon Nanotubes Cuff Electrodes as a Peripheral Nerve Interface'. *Biomedical Microdevices* (Mar. 2018), vol. 20(1): p. 21 (cit. on p. 83).

163. Seki, Yusuke, Shota Yamagiwa, Yusuke Morikawa, Hirohito Sawahata, Rika Numano, Makoto Ishida, and Takeshi Kawano: 'Hook and Loop Microfastener: Flexible Microelectrodes Tied to a Nerve'. *2017 IEEE 30th International Conference on Micro Electro Mechanical Systems (MEMS)*. 2017 IEEE 30th International Conference on Micro Electro Mechanical Systems (MEMS). Las Vegas, NV, USA: IEEE, Jan. 2017: pp. 117–120 (cit. on p. 83).

164. Kang, Xiaoyang, Jing-Quan Liu, Hongchang Tian, Bin Yang, Yanna Nuli, and Chunsheng Yang: 'Self-Closed Parylene Cuff Electrode for Peripheral Nerve Recording'. *Journal of Microelectromechanical Systems* (Apr. 2015), vol. 24(2): pp. 319–332 (cit. on pp. 83, 84).

165. Kim, B. J., B. Chen, M. Gupta, and E. Meng: 'Formation of Three-Dimensional Parylene C Structures via Thermoforming'. *Journal of*

Micromechanics and Microengineering (June 1, 2014), vol. 24(6): p. 065003 (cit. on p. 83).

166. Chen, Yihang, Nicholas J. Rommelfanger, Ali I. Mahdi, Xiang Wu, Scott T. Keene, Abdulmalik Obaid, Alberto Salleo, Huiliang Wang, and Guosong Hong: 'How Is Flexible Electronics Advancing Neuroscience Research?' *Biomaterials* (Jan. 2021), vol. 268: p. 120559 (cit. on p. 83).

167. Terutsuki, Daigo, Hayato Yoroizuka, Shin-ichiro Osawa, Yuka Ogihara, Hiroya Abe, Atsuhiro Nakagawa, Masaki Iwasaki, and Matsuhiko Nishizawa: 'Totally Organic Hydrogel-Based Self-Closing Cuff Electrode for Vagus Nerve Stimulation'. *Advanced Healthcare Materials* (Dec. 2022), vol. 11(23): p. 2201627 (cit. on p. 83).

168. Varga, Melinda, Marco Luniak, and Klaus-Jurgen Wolter: 'Novel Self-Folding Electrode for Neural Stimulation and Recording'. *2013 IEEE XXXIII International Scientific Conference Electronics and Nanotechnology (ELNANO).* 2013 IEEE XXXIII International Scientific Conference on Electronics and Nanotechnology (ELNANO 2013). Kiev: IEEE, Apr. 2013: pp. 237–240 (cit. on p. 83).

169. Thakur, Raviraj, Felix P. Aplin, and Gene Y. Fridman: 'A Hydrogel-Based Microfluidic Nerve Cuff for Neuromodulation of Peripheral Nerves'. *Micromachines* (Dec. 8, 2021), vol. 12(12): p. 1522 (cit. on p. 83).

170. Caravaca, A. S., T. Tsaava, L. Goldman, H. Silverman, G. Riggott, S. S. Chavan, C. Bouton, K. J. Tracey, R. Desimone, E. S. Boyden,

H. S. Sohal, and P. S. Olofsson: ‘A Novel Flexible Cuff-like Microelectrode for Dual Purpose, Acute and Chronic Electrical Interfacing with the Mouse Cervical Vagus Nerve’. *Journal of Neural Engineering* (Dec. 1, 2017), vol. 14(6): p. 066005 (cit. on p. 84).

171. Raspopovic, Stanisa, Jacopo Carpaneto, Esther Udina, Xavier Navarro, and Silvestro Micera: ‘On the Identification of Sensory Information from Mixed Nerves by Using Single-Channel Cuff Electrodes’. (2010), vol. (cit. on pp. 86, 94).

172. Cisnal, Ana, Juan-Carlos Fraile, Javier Pérez-Turiel, Victor Muñoz-Martinez, Carsten Müller, and Frank R. Ihmig: ‘A Measurement Setup and Automated Calculation Method to Determine the Charge Injection Capacity of Implantable Microelectrodes’. *Sensors* (Nov. 27, 2018), vol. 18(12): p. 4152 (cit. on p. 91).

173. Ganji, Mehran, Atsunori Tanaka, Vikash Gilja, Eric Halgren, and Shadi A. Dayeh: ‘Scaling Effects on the Electrochemical Stimulation Performance of Au, Pt, and PEDOT:PSS Electrocorticography Arrays’. *Advanced Functional Materials* (Nov. 2017), vol. 27(42): p. 1703019 (cit. on p. 92).

174. Oldroyd, Poppy and George G Malliaras: ‘Achieving Long-Term Stability of Thin-Film Electrodes for Neurostimulation’. *Acta Biomaterialia* (Feb. 2022), vol. 139: pp. 65–81 (cit. on pp. 92, 99).

175. Szymanska, Agnieszka A., Ashkan Hajirasooliha, and Zoran Nenadic: ‘Source Location as a Feature for the Classification of Multi-Sensor

Extracellular Action Potentials'. *2013 6th International IEEE/EMBS Conference on Neural Engineering (NER)*. 2013 6th International IEEE/EMBS Conference on Neural Engineering (NER). San Diego, CA, USA: IEEE, Nov. 2013: pp. 235–238 (cit. on p. 94).

176. Pollack, Gerald S. and Zen Faulkes: 'Representation of Behaviorally Relevant Sound Frequencies by Auditory Receptors in the Cricket Teleogryllus Oceanicus'. (1993), vol. (cit. on p. 94).

177. Stecker, Mark, Kelly Baylor, Jacob Wolfe, and Matthew Stevenson: 'Acute Nerve Stretch and the Compound Motor Action Potential'. *Journal of Brachial Plexus and Peripheral Nerve Injury* (Sept. 23, 2014), vol. 06(01): e11–e22 (cit. on p. 98).

178. Lu, Linlin, Xuefeng Fu, Yijuin Liew, Yongyi Zhang, Siyuan Zhao, Zheng Xu, Jingna Zhao, Da Li, Qingwen Li, Garrett B. Stanley, and Xiaojie Duan: 'Soft and MRI Compatible Neural Electrodes from Carbon Nanotube Fibers'. *Nano Letters* (Mar. 13, 2019), vol. 19(3): pp. 1577–1586 (cit. on p. 98).

179. Cogan, S.F., P.R. Troyk, J. Ehrlich, and T.D. Plante: 'In Vitro Comparison of the Charge-Injection Limits of Activated Iridium Oxide (AIROF) and Platinum-Iridium Microelectrodes'. *IEEE Transactions on Biomedical Engineering* (Sept. 2005), vol. 52(9): pp. 1612–1614 (cit. on p. 98).

180. Ganske, G., E. Slavcheva, A. van Ooyen, W. Mokwa, and U. Schnakenberg: 'Sputtered Platinum–Iridium Layers as Electrode Material

for Functional Electrostimulation'. *Thin Solid Films* (Mar. 2011), vol. 519(11): pp. 3965–3970 (cit. on p. 98).

181. Čvančara, Paul et al.: 'Stability of Flexible Thin-Film Metallization Stimulation Electrodes: Analysis of Explants after First-in-Human Study and Improvement of in Vivo Performance'. *Journal of Neural Engineering* (July 10, 2020), vol. 17(4): p. 046006 (cit. on p. 99).

182. Lee, Curtis D. and Ellis Meng: 'Mechanical Properties of Thin-Film Parylene–Metal–Parylene Devices'. *Frontiers in Mechanical Engineering* (Sept. 8, 2015), vol. 1 (cit. on p. 99).

183. Brehélin, Michel, J.A. Hoffmann, G. Matz, and A. Porte: 'Encapsulation of Implanted Foreign Bodies by Hemocytes in Locusta Migratoria and Melolontha Melolontha'. *Cell and Tissue Research* (July 1975), vol. 160(3) (cit. on p. 101).

184. Eastwood, Peter R. et al.: 'Bilateral Hypoglossal Nerve Stimulation for Treatment of Adult Obstructive Sleep Apnoea'. *European Respiratory Journal* (Jan. 2020), vol. 55(1): p. 1901320 (cit. on p. 108).

185. Ando, Daiki, Tetsuhiko F. Teshima, Francisco Zurita, Hu Peng, Kota Ogura, Kenji Kondo, Lennart Weiss, Ayumi Hirano-Iwata, Markus Becherer, Joe Alexander, and Bernhard Wolfrum: 'Filtration-Processed Biomass Nanofiber Electrodes for Flexible Bioelectronics'. *Journal of Nanobiotechnology* (Nov. 19, 2022), vol. 20(1): p. 491 (cit. on p. 108).

186. Chiappalone, Michela, Vinicius R. Cota, Marta Carè, Mattia Di Florio, Romain Beaubois, Stefano Buccelli, Federico Barban, Martina Brofiga, Alberto Averna, Francesco Bonacini, David J. Guggenmos, Yannick Bornat, Paolo Massobrio, Paolo Bonifazi, and Timothée Levi: 'Neuromorphic-Based Neuroprostheses for Brain Rewiring: State-of-the-Art and Perspectives in Neuroengineering'. *Brain Sciences* (Nov. 19, 2022), vol. 12(11): p. 1578 (cit. on p. 111).

187. Gupta, Ankur, Nikolaos Vardalakis, and Fabien B. Wagner: 'Neuroprosthetics: From Sensorimotor to Cognitive Disorders'. *Communications Biology* (Jan. 6, 2023), vol. 6(1): p. 14 (cit. on p. 111).

List of Figures

1.1 Concept art of neural tissue interfacing an electronic circuit. This image was created with the assistance of `craiyon.com`. 1

2.1 A schematic of a typical mammalian neuron depicting its constituent parts. 7

2.2 Typical shape of an action potential. The rising edge is due to the sudden influx of Na^+ into the cell. The repolarization is due to the inactivation of the Na^+ ion channels and the efflux of K^+. 10

2.3 Hodgkin-Huxley electrical model of the cell membrane. 11

2.4 Ion distribution during the propagation of an action potential along an axon. 14

2.5 Conceptual chart relating invasiveness and selectivity of peripheral nerve interfaces. 17

2.6 Electrode-electrolyte interface. A negatively charged electrode is submerged into an electrolyte solution with positive and negative charges. Cations are driven by the electric field towards the interface and adsorb to it, shielding the electric field from the bulk of the solution. Anions are also electrically driven into the bulk of the electrolyte solution. Since the electric field is shielded, the ions in the bulk of the solution do not feel electrostatic force. 21

2.7 Exemplary voltammogram of a redox reaction. E represents the applied potential to the electrode and i the measured current. E_c and E_a are the cathodic and anodic vertex potentials, respectively. i_P is the peak current measured and the potential at which this happens is the E_P. 27

2.8 A sample voltammogram highlighting the $\mathrm{CSC_c}$ and the $\mathrm{CSC_a}$ as the areas enclosed by the cathodic and anodic currents, respectively. The cathodic and anodic currents are further separated into the portions obtained during the forward ($i_{f,c}$, $i_{f,a}$) and backward ($i_{b,c}$, $i_{b,a}$) scans. 29

2.9 An exemplary voltage transient response to a biphasic current pulse. 31

2.10 Simplified Randles circuit. 33

2.11 The locust of the species *Locusta migratoria* was the main experimental subject for this work. 34

2.12 Jumping behavior of a locust captured with a high-speed camera at different timestamps. The tibiofemoral angle of the hind leg is shown, with 0° corresponding to the leg position in which the tibia is perpendicular to the femur. The images were digitally corrected using `enhance.pho.to`. The tibiofemoral angle was estimated using ImageJ [70]. 35

2.13 Diagram of the anatomy of the *Locusta migratoria*. 36

2.14 3D model of the nervous system of the *Locusta migratoria*. The chain of ganglia is displayed in white, with a reference N5 emerging from the metathoracic ganglion and innervating the hind leg. 37

2.15 Cross-sectional view of the N5 of a *Locusta migratoria* at the level of the metathorax. The tissue slice has been stained with hematoxylin-eosin. The pink regions represent the axons. It can be seen that the axon size distribution is not uniform, with some fibers being visibly larger than others. The fuchsia structure that surrounds the nerve is the nerve sheath. This Figure was obtained in collaboration with Dr. Tanja Groll and PD Dr. Katja Steiger, Comparative Experimental Pathology, Technical University of Munich. 39

3.1 Scheme of the implemented control loop. The angle set point is selected and the measured leg angle subtracted from it to conform the error signal, which is sampled by the microcontroller. A proportional control algorithm runs in the microcontroller, varying the period of the stimulus signal applied on the nerve. The leg angle is sensed with a flexible resistor to provide the feedback. 45

3.2 PDMS cuff fabrication steps. **(a)** The mold for the cuff is 3D-printed as two separated parts. After assembly, the two parts form a cavity with the desired dimension of the cuff. **(b)** The molds are tightly screwed together, and a needle is placed inside the mold to form the cuff's lumen. PDMS is cast inside the resulting tube-shaped cavity. **(c)** The excess air in the PDMS is removed by degassing in a vacuum chamber and the PDMS is thermally cured. **(d)** After curing, the tube is detached from the mold and the stimulation electrodes are inserted through the PDMS tube. The cuff is then cut to a length of ~1 mm and opened along the tube to enable nerve insertion. Finally, the exterior of the electrode is coated with parylene-C. 47

3.3 (a) *Locusta migratoria* prior to the surgery in clay bed. (b) Scheme of the metathoracic ganglion and the nerves innervating the hind leg. (c) Microscope image of the surgical incision on the metathorax of the locust, showcasing the N5 immediately before insertion in the cuff electrode. 49

3.4 Electrochemical characterization of the custom-made cuff electrodes in saline solution. The characterization was performed in a bipolar configuration between the two stimulation electrodes in the cuff. **(a)** Chronoamperogram for three different voltage step amplitudes. **(b)** Impedance spectroscopy analysis exhibiting a combined impedance of ~1.4 kΩ @ 1 kHz. 51

3.5 A set point voltage is applied to determine the desired angle of the leg. The error between set point and feedback signals is converted into a stimulation pulse pattern (red), and a corresponding inter-pulse delay. The stimulation pattern triggers a response in the leg angle, which is extracted from video recordings. In **(a)** the black traces show 10 repetitions of the same experiment, whereas in **(b)** they show 5 repetitions of the same experiment. The thicker black traces correspond to the indicated pulse pattern. 54

3.6 Scatter plot of the angle of the leg versus the frequency of stimulation, computed as the inverse of the inter-pulse delay, for the voltage ramp experiment. The upper cluster (red) represents the trajectory of flexion of the leg, whereas the lower cluster (black) represents the trajectory of extension of the leg. The linear fits are computed using the method of least-squares. 56

4.1 Electrode fabrication process of the proposed cuff electrode. **(a)**, **(b)** Printing of the feedline connectors. **(c)**, **(d)** Printing of the 3D microelectrodes via successive deposition of Ag nanoparticle ink droplets on top of each other. **(e)**, **(f)** Deposition of the insulation layer covering the feedlines. **(g)**, **(h)** Fabrication of the 3D nerve cuff via two-photon stereolithography. 61

4.2 Experimental setup used to record the movement of the leg during stimulation. The subject *Locusta migratoria* was placed ventral face up. The N5 was exposed and interfaced with the cuff electrodes using a micromanipulator. The electrode was interfaced to an INTAN headstage, connected to an INTAN controller, which in turn was connected to a PC. A camera, connected to the same PC, was used to record the leg movement, and extract the tibiofemoral angle $\theta(t)$. . 65

4.3 Nerve interfacing with the 3D-printed cuff electrode. **(a)** Concept image of a nerve with three axons, interfaced with our designed cuff electrode. The nerve is only shown along half the length of the cuff electrode for a better view of the axons and 3D microelectrodes. **(b)** Microscopy image of the cuff electrode wrapping around a nerve (N5) of a locust. **(c)**–**(e)** Tilt-corrected scanning electron microscope images of the fabricated cuff electrode. A substrate tilt of 45° **(d)**, **(e)**, and 70° **(c)** were used to image the cuff electrode. The 3D electrodes have been false-colored in yellow for clarity. All 3 images were taken using an accelerating voltage of 15 kV. 68

4.4 Electrochemical impedance spectroscopy characteristics of the electrode. **(a)**,**(c)** Magnitude and **(b)**,**(d)** phase of the impedance of differently configured 3D electrodes in locust saline. Averaged impedance data between 3D electrodes and a Pt mesh in **(a)** and **(b)** (n = 16). Averaged impedance data between two 3D electrodes measured against each other in different configurations in **(c)** and **(d)** (n = 3 – 5). 69

4.5 Tibiofemoral joint angle span elicited through electrical stimulation. Different electrode combinations were used, with a leading cathodic phase (red), a leading anodic phase (light blue), and inactive electrode (black). The red arrow indicates the proximal-to-distal direction of the nerve relative to the electrodes. The stimulation current was a sequence of bipolar pulses in succession starting at t = 0, shown in **(a)** and **(c)**. **(a)**, **(b)** The stimulus is a bipolar current pulse train of 60 µA of amplitude and 500 µs pulse duration between two individual electrodes. The number of delivered pulses ranges from 5 to 20, and each trace shows the mean and standard deviation of 20 stimulation events. **(c)** The stimulus is a bipolar current pulse train of 30 µA of amplitude and 500 µs pulse duration between two pairs of electrodes. For this last scenario, movement was elicited when both phases were on adjacent electrodes. For all other combinations of pairs of electrodes, no movement was elicited. 70

4.6 Finite-element-method simulations of the electric field and activating functions for two electrode configurations. **(a)** Top view of the simulated elements on a plane cutting through the middle of the nerve, perpendicularly to the microelectrodes. E_x component of the electric field for **(b)** CCAA and **(c)** CACA configurations. E_x component and activating function along the center line of the nerve (y = 0) for **(d)** CCAA and **(e)** CACA configurations. 77

4.7 Mean and standard deviation for 50 compound action potential events. **(a)** The phase of the channels leads in proximal (ch1) to distal (ch4) direction, hinting activity from efferent nerve fibers. **(b)** The phase of the channels leads in distal (ch4) to proximal (ch1) direction, hinting activity from afferent nerve fibers. 78

5.1 Electrochemical characterization of the active electrode in PBS. **(a)** Bode plots of the impedance of the electrodes in PBS depicted as the mean and the standard deviation of 16 electrodes. The solid and dashed lines show the EIS before and after delivering 10^6 biphasic current pulses, respectively. **(b)** CV of 16 electrodes scanned at $50\,\mathrm{mV\,s^{-1}}$. We determine the water window to be at $\pm1.3\,\mathrm{V}$. **(c)** Representative voltage transient resulting from a $0.9\,\mathrm{mA}$ biphasic stimulation pulse. Here, we showcase the relevant voltage values to calculate the electrode's charge injection capacity (CIC). This trace corresponds to an injected charge density of $300\,\mathrm{\mu C\,cm^{-2}}$. **(d)** The charge injection density of 16 electrodes, shown in mean and standard deviation. The charge injection capacity is estimated to be $121\,\mathrm{\mu C\,cm^{-2}}$. 90

5.2 Interfacing of the locust N5 with the 4D cuff electrode. **(a)** Metathoracic cavity of a locust, exposing the metathoracic ganglion and nerves. **(b)** Movement of the hindleg elicited by the nerve stimulation. **(c)** Angle of the leg over ten stimulation pulses. 93

5.3 Electrophysiological recordings of spontaneous activity of the N5 with a 6-channel cuff electrode. **(a)** Activity during one minute, the larger spikes correspond to leg movement. Zoomed-in snippets from the main trace at different times show **(b)** a motor signal traveling from the ganglion to the leg (efferent) and **(c)** a sensory signal traveling from the leg to the ganglion (afferent). The direction of propagation of the signal can be determined from the observed phase delay between the different channels, with **(b)** the most proximal channel (ch1) leading during efferent activity and **(c)** lagging during afferent activity. 95

5.4 The pre-folded electrodes are fabricated by **(a)** depositing a substrate of 5 µm parylene-C, sputtering Pt/Ir on top and patterning it to the shape of the electrodes. Then, **(b)** a second layer of parylene-C is deposited on top, followed by a metal coating of Al, which serves as a masking layer for etching the parylene-C. The coating over the electrode sites is laser-etched. Finally, **(c)** the parylene-C over the electrode sites is O_2-etched and the masking layer is removed with KOH. To pre-fold the device, **(d)** its tip is attached to a resistively heated wire of the desired diameter of the target nerve. After attachment, **(e)** the cuff is rolled and later thermoformed to obtain the final cuff shape **(f)**. **(g)** shows a picture of the device at the end of the fabrication process. **(h)** The final device is highly flexible, which is advantageous for implantation in constrained spaces. **(i)** The diameter of the cuff can be easily tuned to the desired nerve. 97

5.5 Electrochemical characterization of the pre-folded devices. **(a)** Voltammograms for unfolded and folded electrodes (n = 12). **(b)** Magnitude and **(c)** phase of the impedance of unfolded, folded and long-term stimulated ("aged") electrodes (n = 12). 99

5.6 **(a)** Schematic of the setup used for in vivo experiments. **(b)** The metathoracic cavity of the locust prior to electrode interfacing, indicating the target nerve. **(c)** Successful nerve interfacing with our cuff electrode. **(d)** Superimposed hind leg image depicting how the angle is measured. **(e)** Angle span for the electrode combinations that elicited leg movement. The inset illustrates the location of the electrode number on the unrolled cuff. 102

5.7 Histological images of the N5 interfaced with the pre-folded cuff electrodes stained with **(a)** hematoxylin-eosin and **(b)** Masson's trichome. A tissue layer is formed around the parylene-C cuff. The gap between the cuff and the nerve is due to the nerve shrinking during the fixation process. **(c)** A non-interfaced nerve does not present the capsule formation around it. 103

B.1 Schematic of the system used to close the control loop. 165

D.1 Tilt-corrected scanning electron microscope images of 3D-printed cuff holders using two-photon stereolithography. 172

E.1 Leg angle span elicited by two electrodes (all combinations) for pulse amplitudes of 30 µA and 60 µA. The different traces represent the number of pulses (5 to 20) per stimulation signal. A cathodic-leading phase for each individual electrode is marked as red, an anodic-leading phase as light blue, and an inactive electrode as black. 174
E.2 Leg angle span elicited by two electrodes (all combinations) for pulse amplitudes of 30 µA and 60 µA. The different traces represent the number of pulses (5 to 20) per stimulation signal. A cathodic-leading phase for each individual electrode is marked as red, an anodic-leading phase as light blue, and an inactive electrode as black. 175
E.3 Leg angle span elicited by different combinations of double pairs of electrodes for stimulation amplitudes between 35 µA and 60 µA. A cathodic-leading phase for each individual electrode is marked as red and an anodic-leading phase as light blue. 176

F.1 Geometry of the cuff electrode used in the COMSOL simulations. **(a)** The cuff electrode without and **(b)** with the nerve model. 178

G.1 Spontaneous activity of the N5 outside of the hemolymph recorded with Ag hook electrodes. 179

List of Tables

6.1 Comparison of the different devices presented in this thesis. 111

A *Locusta migratoria* surgical procedure

The surgical procedure for the *Locusta migratoria* used in this work is captured in an educational video and can be found on `https://www.nature.com/articles/s41598-022-13679-z`. The video covers the topics of surgery preparation, surgical procedure, and nerve handling. The speech in the video was artificially generated through the website `https://ttsmp3.com/`.

A.1 Procedure

The following procedural aspects help to avoid potential caveats during the procedure:

1. The locust should be fixed immediately after chilling, or it will elicit strong movements if warmed up. The experiment can be conducted at a low temperature for easier handling.
2. The locust should not be maintained in a freezer to ensure vitality.
3. During the surgery, the locust may produce a dark liquid from its mouth. This liquid should be quickly absorbed with tissue, as it can damage the nerves if it gets in contact.
4. The locust should be properly fixed in the modeling clay bed. However, a gap in the clay bed to the sides of the locust at the level of the metathorax should be provided to allow breathing.

5. A superficial cut on the metathoracic cuticle should be performed to avoid damage to trachea and ganglion.
6. The cavity should be kept moist with saline solution to avoid drying of the nerve tissue.
7. The locusts should be handled with care. Excessive stimulation of the nerve (frequency or current) should be avoided. Furthermore, locusts should not be grabbed from the leg. In both cases, the animal will tend to autotomize (detach) the compromised limb.
8. For termination, the locust can be placed in a freezer overnight or dipped in liquid nitrogen for ~10 s.

B Control circuit

In the following, I describe the electronic circuit used to implement the control loop of Chapter 3. The components used are a Nordic nRF52840-DK, a flexible resistor, a 100 kΩ potentiometer, a TL094 operational amplifier, and resistors to set amplification gain in the differential (R1-R4) and gain (R5, R6) stages.

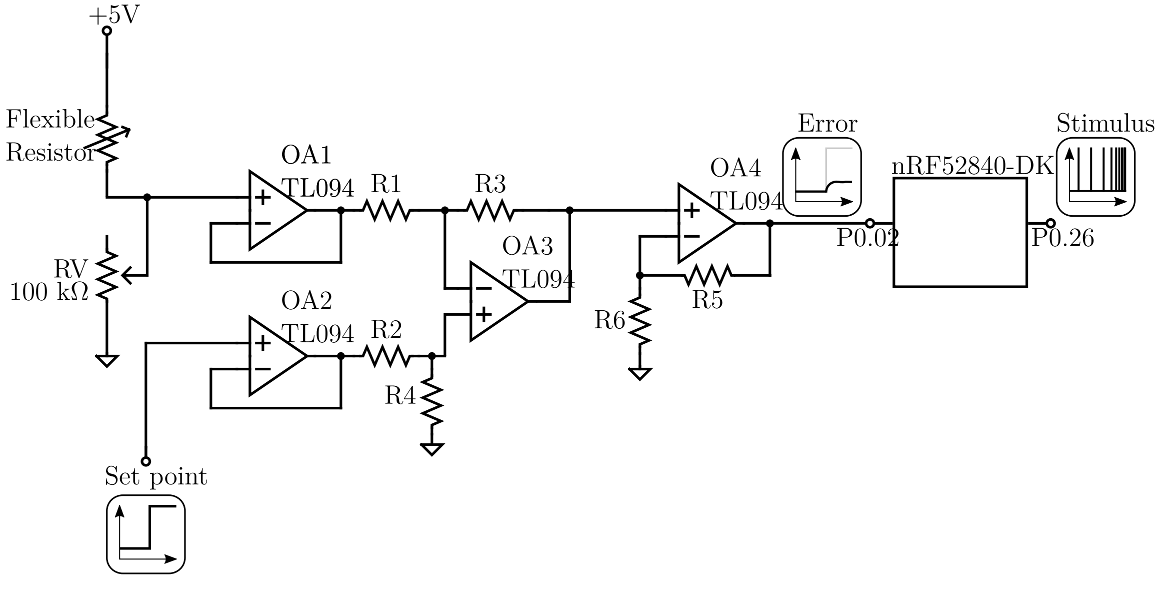
+5V
Flexible Resistor
RV
100 kΩ
OA1
TL094
R1
R3
OA2
TL094
R2
R4
OA3
TL094
OA4
TL094
R5
R6
Error
nRF52840-DK
Stimulus
P0.02
P0.26
Set point

Figure B.1: Schematic of the system used to close the control loop.

The values of R1, R2, R3, and R4 set the preamplification of the Set Point and Feedback signals, so the voltage range of the feedback matches the desired set point. The Error signal is then calculated as:

$$Error = Set\,Point \cdot \left(\frac{R4}{R2 + R4}\right) \cdot \left(\frac{R1 + R3}{R1}\right) - Feedback \cdot \left(\frac{R3}{R1}\right) \tag{B.1}$$

R5 and R6 are used to set the amplification gain before signal acquisition by the microcontroller.

The microcontroller is programmed to receive the error signal from P0.02 and generate the pulse signal from P0.26. The output pulse delays are clipped between 50 ms and 250 ms. The potentiometer and non-inverting gain stage can be used to calibrate the desired error signal, e.g., to produce maximum error when the flexible resistor is fully bent, or within a certain bending range.

C Schematic of the cuff molds

This section shows the schematics of the 3D-printed molds to produce the PDMS silicone cuff presented in Chapter 3.

C.1 Top mold

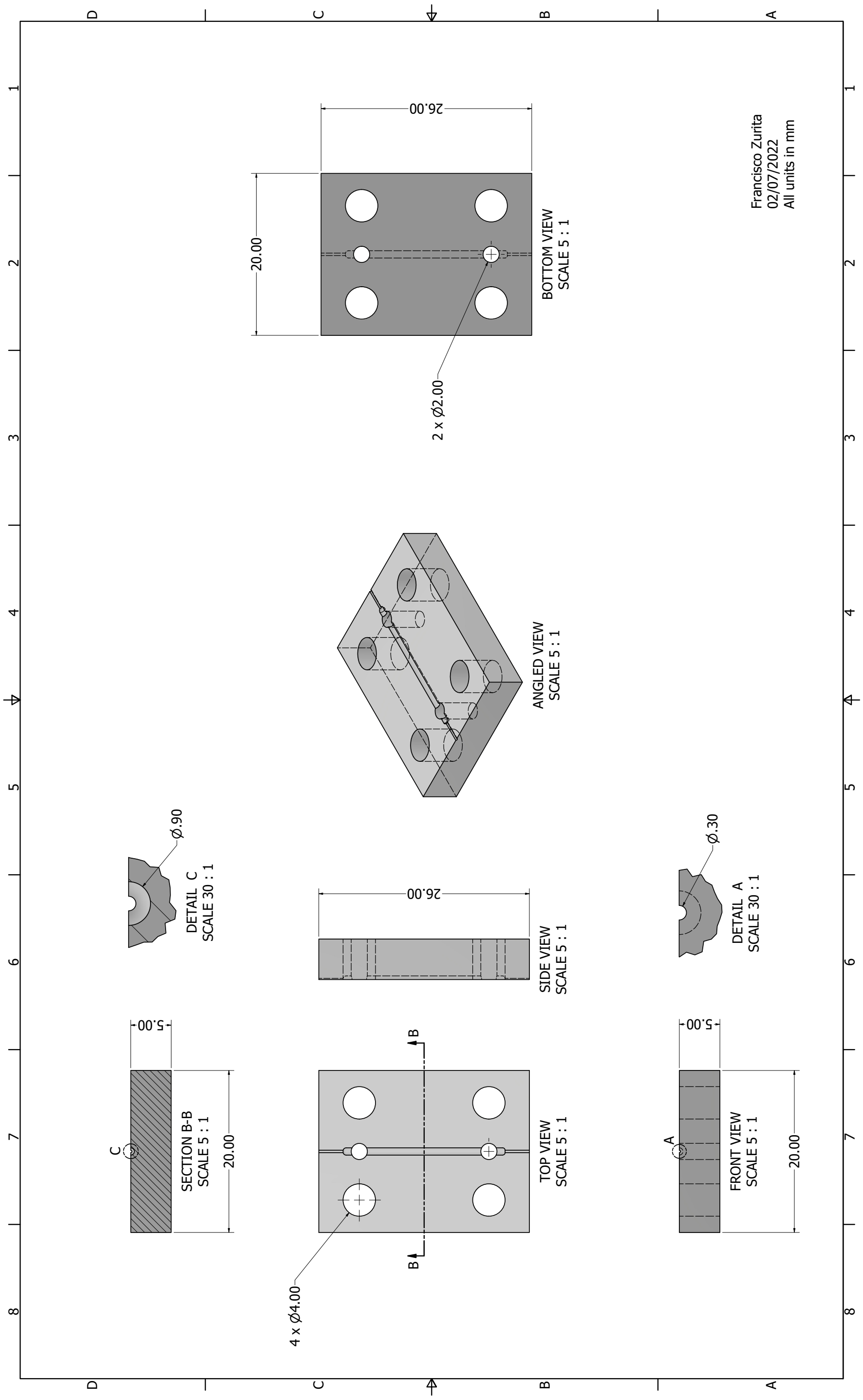
D
C
B
A
1
2
3
4
5
6
7
8
26.00
20.00
BOTTOM VIEW
SCALE 5 : 1
2 x Ø2.00
Francisco Zurita
02/07/2022
All units in mm
ANGLED VIEW
SCALE 5 : 1
Ø.90
DETAIL C
SCALE 30 : 1
26.00
SIDE VIEW
SCALE 5 : 1
Ø.30
DETAIL A
SCALE 30 : 1
5.00
C
SECTION B-B
SCALE 5 : 1
20.00
B
B
TOP VIEW
SCALE 5 : 1
4 x Ø4.00
5.00
A
FRONT VIEW
SCALE 5 : 1
20.00

C.2 Bottom mold

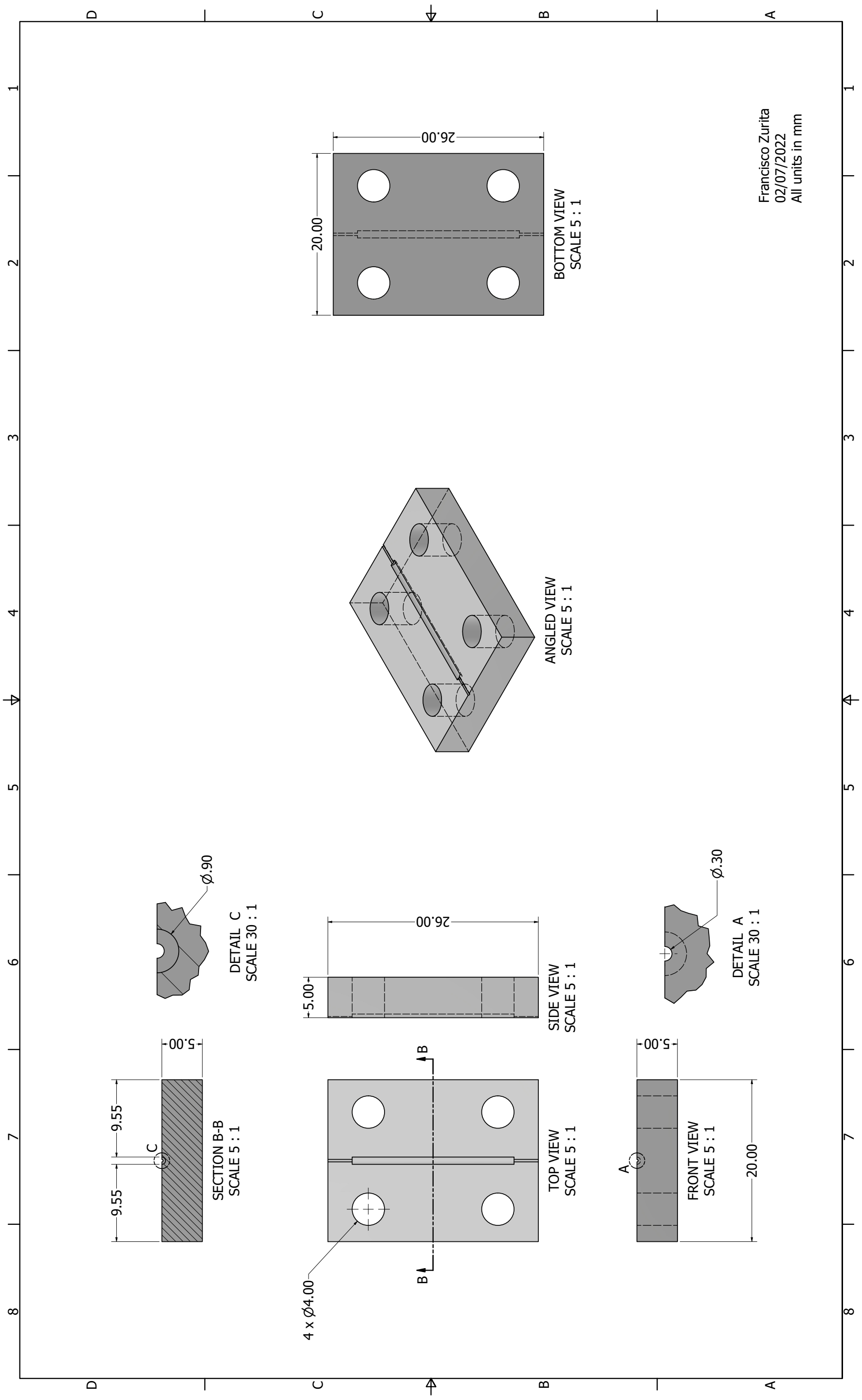
Francisco Zurita
02/07/2022
All units in mm
26.00
20.00
BOTTOM VIEW
SCALE 5 : 1
ANGLED VIEW
SCALE 5 : 1
Ø.90
DETAIL C
SCALE 30 : 1
26.00
5.00
SIDE VIEW
SCALE 5 : 1
Ø.30
DETAIL A
SCALE 30 : 1
5.00
9.55
9.55
C
SECTION B-B
SCALE 5 : 1
B
B
4 x Ø4.00
TOP VIEW
SCALE 5 : 1
5.00
A
FRONT VIEW
SCALE 5 : 1
20.00
A
B
C
D
1
2
3
4
5
6
7
8

D Evolution of the final design of the 3D-printed cuff electrodes

Here I describe the previous stages of development of the fully 3D-printed nerve cuff presented in Chapter 4. After preliminary tests shown in Figure D.1, the designs were directly transferred to sensors with conductive 3D electrodes. During the stereolithographic printing stage, microbubbles were perceived around the 3D electrodes which inhibited the possibility of polymerizing the desired structure. Therefore, special cavities were added to the housing desing to incorporate the 3D electrodes.

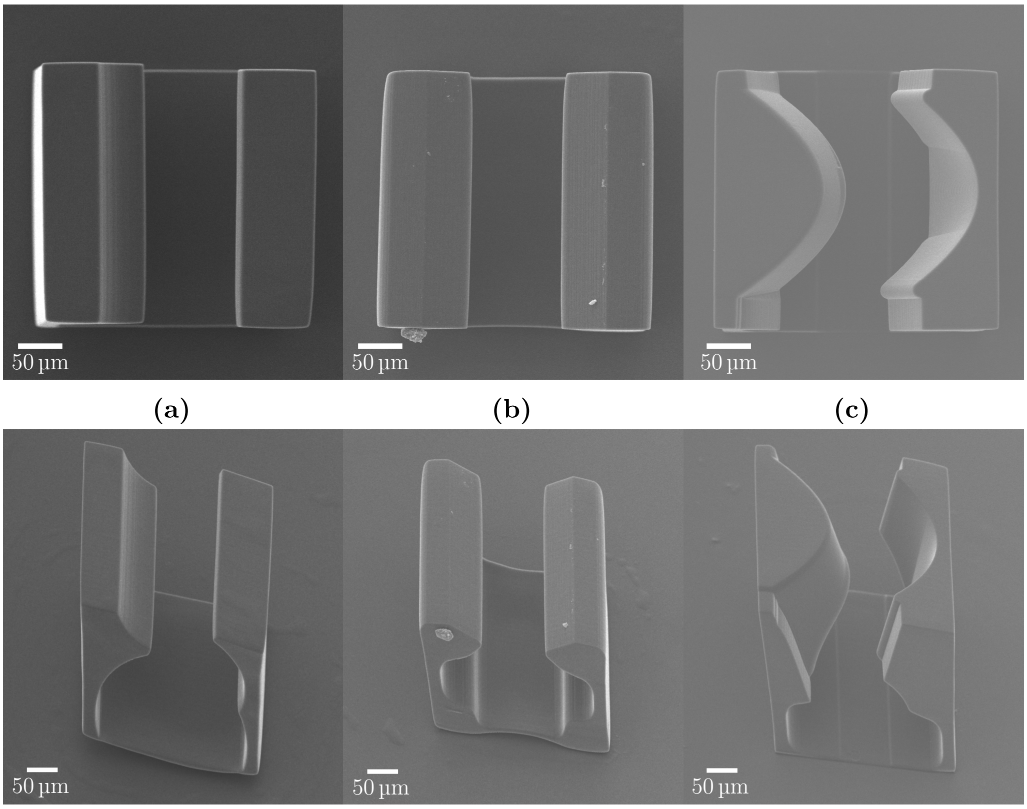
50 µm
50 µm
50 µm
50 µm
50 µm
50 µm

(a) **(b)** **(c)**

(d) **(e)** **(f)**

Figure D.1: Tilt-corrected scanning electron microscope images of 3D-printed cuff holders using two-photon stereolithography.

E Locust leg movement

The movement of the locust leg using the nerve cuff presented in Chapter 4 are presented in this section, for all the measured combinations.

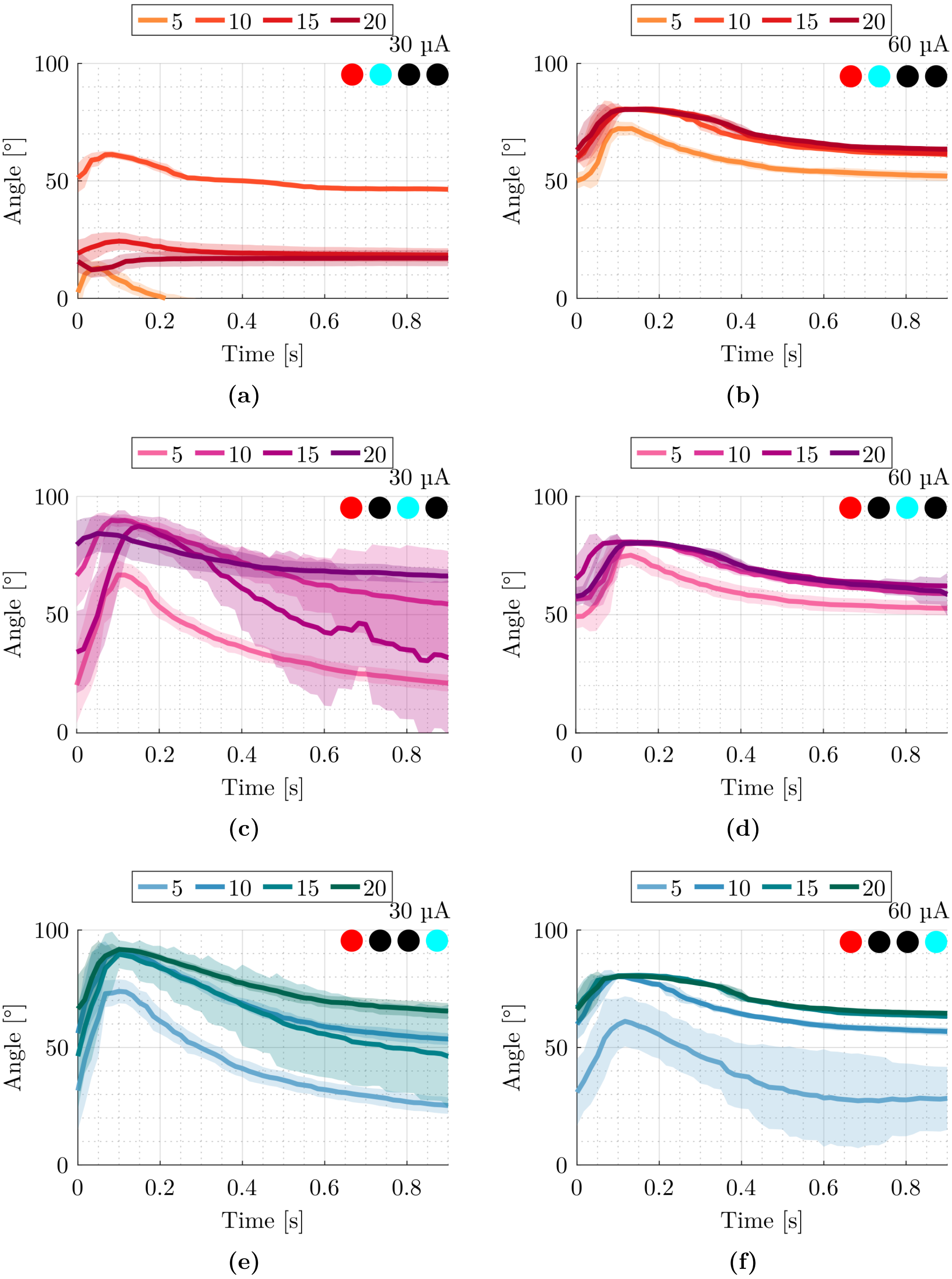

(a) (b)

(c) (d)

(e) (f)

Figure E.1: Leg angle span elicited by two electrodes (all combinations) for pulse amplitudes of 30 µA and 60 µA. The different traces represent the number of pulses (5 to 20) per stimulation signal. A cathodic-leading phase for each individual electrode is marked as red, an anodic-leading phase as light blue, and an inactive electrode as black.

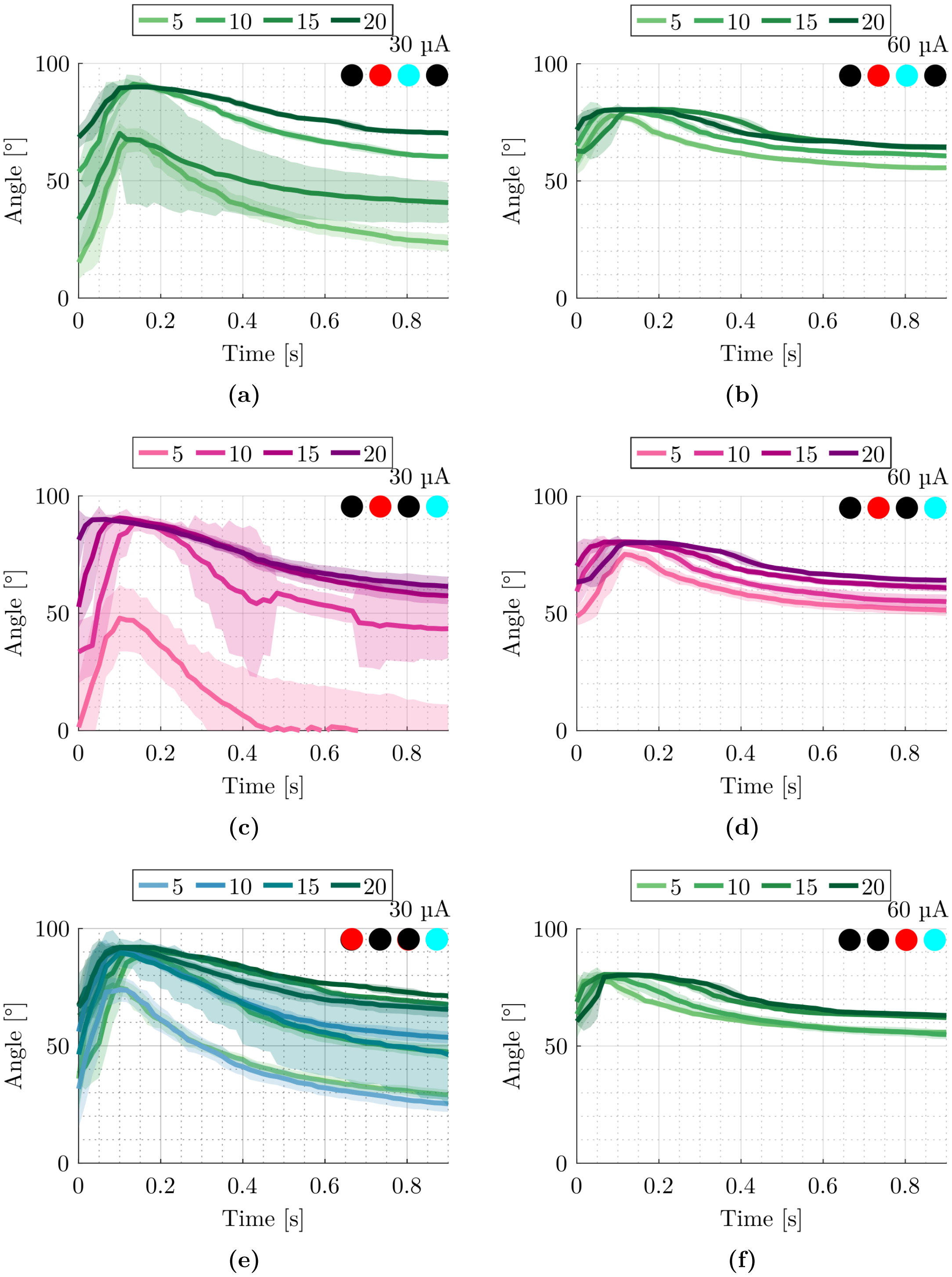

(a) **(b)**

(c) **(d)**

(e) **(f)**

Figure E.2: Leg angle span elicited by two electrodes (all combinations) for pulse amplitudes of 30 µA and 60 µA. The different traces represent the number of pulses (5 to 20) per stimulation signal. A cathodic-leading phase for each individual electrode is marked as red, an anodic-leading phase as light blue, and an inactive electrode as black.

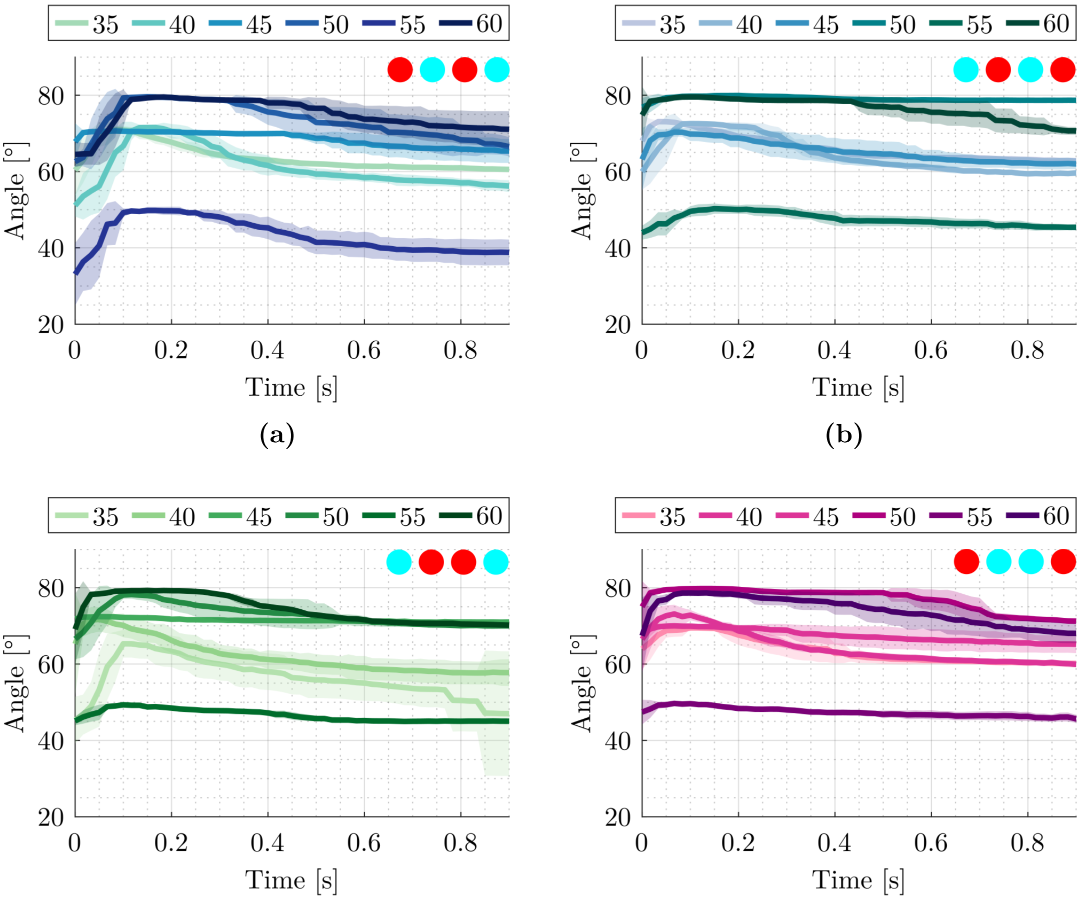

(a) **(b)** **(c)** **(d)**

Figure E.3: Leg angle span elicited by different combinations of double pairs of electrodes for stimulation amplitudes between 35 µA and 60 µA. A cathodic-leading phase for each individual electrode is marked as red and an anodic-leading phase as light blue.

F Finite element method simulations

Finite element method simulations were carried out to estimate the electric field and activating function along the direction of the nerve for different electrode combinations, as presented in Chapter 4. The following elements were used in the simulation:

1. A $3\,\mathrm{mm}^3$ cube was designed to model the environmental electrolytic solution. It was based on PBS and it was assigned a conductivity of $\sigma = 1.52\,\mathrm{S\,m^{-1}}$.
2. The 3D-printed cuff was positioned at the center of the cube. It was assigned the electrical properties of an insulator. A rectangular prism ($1\,\mathrm{mm} \times 1\,\mathrm{mm} \times 0.02\,\mathrm{mm}$) was positioned below the cuff to model the PEN electrode substrate.
3. The 4 individual microelectrodes were modeled as the union of a cylinder ($r_c = 20\,\mathrm{\mu m}$, $h = 150\,\mathrm{\mu m}$) and a half sphere on top ($r_s = 20\,\mathrm{\mu m}$). They were assigned the material properties of Ag ($\sigma = 6.3 \times 10^7\,\mathrm{S\,m^{-1}}$). The bases of the cylinders were assigned current sink/source as boundary conditions, with a density of $47.75 \times 10^3\,\mathrm{A\,m^{-2}}$, calculated as $60\,\mathrm{\mu A}$ over the area of the base of the cylinder.
4. A nerve was modeled as a cylinder ($r_n = 80\,\mathrm{\mu m}$, $l = 2.5\,\mathrm{mm}$) and assigned a conductivity $\sigma = 0.57\,\mathrm{S\,m^{-1}}$ along the axial direction of the axon, and $\sigma = 0.083\,\mathrm{S\,m^{-1}}$ in the other directions. It was surrounded by a nerve sheath

of the same length ($d = 10\,\mu\text{m}$) and assigned a lower conductivity ($\sigma = 2.1 \times 10^{-3}\,\text{S}\,\text{m}^{-1}$).

5. The solving set of equations used corresponds to the *Electric Currents* module. The 3D geometry used in the simulation is displayed in Figure F.1.

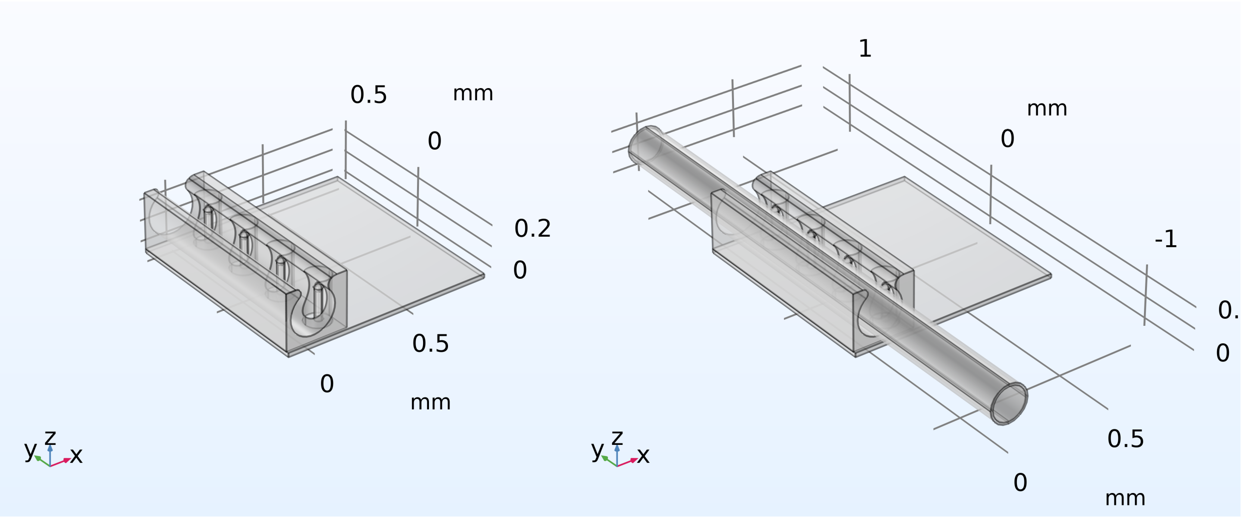

(a) (b)

Figure F.1: Geometry of the cuff electrode used in the COMSOL simulations. **(a)** The cuff electrode without and **(b)** with the nerve model.

G Comparative recordings with Ag hook electrodes

A measurement with Ag hook electrodes was carried out for comparative purposes. Hook electrodes were crafted with Ag wires (Ø = 76.2 µm, Science Products GmbH, Germany) and interfaced with the N5. The nerve was pulled out of the hemolymph using a micromanipulator and spontaneous activity was recorded with the setup described before. A 10-second recording is high-pass filtered as described in Chapter 4 and shown in Figure G.1. It can be seen that the signal amplitude is larger compared to recordings from the cuff electrodes, which is expected because the nerve is isolated without electrolyte to dissipate the current.

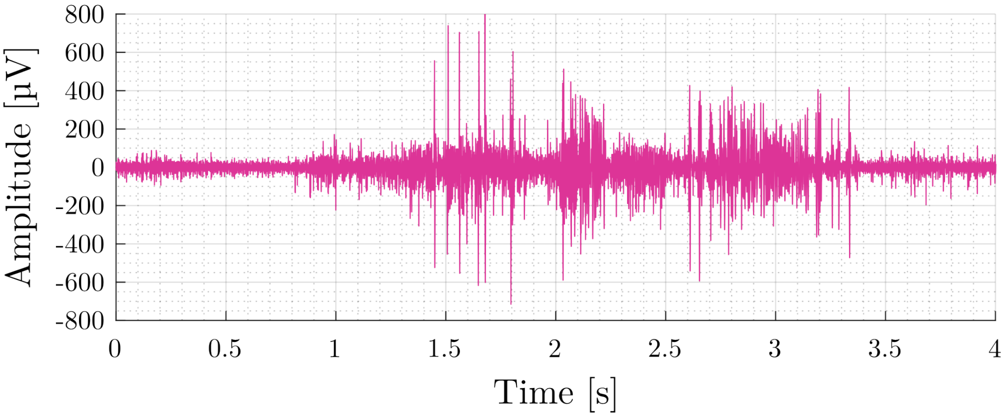

Figure G.1: Spontaneous activity of the N5 outside of the hemolymph recorded with Ag hook electrodes.

The interfaced nerve was then submerged into the hemolymph and the neural activity recorded again. However, in this case no action potential was distinguishable, due to the lack of electrode isolation. In comparison, the 3D electrodes are able to record from the nerve when immersed in the hemolymph due to the 3D-printed insulating nerve cuff.

Publications

Scientific publications

1. Ando, Daiki, Tetsuhiko F. Teshima, **Francisco Zurita**, Hu Peng, Kota Ogura, Kenji Kondo, Lennart Weiss, Ayumi Hirano-Iwata, Markus Becherer, Joe Alexander, and Bernhard Wolfrum: ‘Filtration-Processed Biomass Nanofiber Electrodes for Flexible Bioelectronics’. *Journal of Nanobiotechnology* (Nov. 19, 2022), vol. 20(1): p. 491.
2. Hiendlmeier, Lukas, Tetsuhiko F. Teshima, **Francisco Zurita**, Heike Url, Philipp Rinklin, and Bernhard Wolfrum: ‘A Superabsorbent Sodium Polyacrylate Printing Resin as Actuator Material in 4D Printing’. *Macromolecular Materials and Engineering* (Oct. 2022), vol. 307(10): p. 2200306.
3. Hiendlmeier, Lukas, **Francisco Zurita**, Jonas Vogel, Fulvia Del Duca, George Al Boustani, Hu Peng, Inola Kopic, Marta Nikić, Tetsuhiko F. Teshima, and Bernhard Wolfrum: ‘4D-Printed Soft and Stretchable Self-Folding Cuff Electrodes for Small-Nerve Interfacing’. *Advanced Materials* (Feb. 11, 2023), vol.: p. 2210206.

4. Terkan, Korkut, **Francisco Zurita**, Touba Jamal Khalaf, Philipp Rinklin, Tetsuhiko Teshima, Tobias Kohl, and Bernhard Wolfrum: ‘Soft Peripheral Nerve Interface Made from Carbon Nanotubes Embedded in Silicone’. *APL Materials* (Oct. 1, 2020), vol. 8(10): p. 101111.
5. Teshima, Tetsuhiko F., Lukas Hiendlmeier, Korkut Terkan, Sabine Zips, Leroy Grob, **Francisco Zurita**, Philipp Rinklin, and Bernhard Wolfrum: ‘3D Printing of Implants Composed of Nanjing Tamasudare-Inspired Flexible Shape Transformers’. *Advanced Materials Technologies* (Sept. 2021), vol. 6(9): p. 2100240.
6. **Zurita, Francisco**, Fulvia Del Duca, Tetsuhiko Teshima, Lukas Hiendlmeier, Michael Gebhardt, Harald Luksch, and Bernhard Wolfrum: ‘In Vivo Closed-Loop Control of a Locust’s Leg Using Nerve Stimulation’. *Scientific Reports* (June 27, 2022), vol. 12(1): p. 10864.
7. **Zurita, Francisco**, Leroy Grob, Amelie Erben, Fulvia Del Duca, Hauke Clausen-Schaumann, Stefanie Sudhop, Oliver Hayden, and Bernhard Wolfrum: ‘Fully 3D-Printed Cuff Electrode for Small Nerve Interfacing’. *Advanced Materials Technologies* (Oct. 30, 2022), vol.: p. 2200989.

Acknowledgments

Large projects are rarely shouldered by a single person. I would like to acknowledge the contribution of the following people during these years as a researcher:

- Prof. Dr. Bernhard Wolfrum who granted me the trust and freedom to explore the incredible field of neuroelectronics. More importantly, for creating a friendly atmosphere in the lab for everyone to enjoy their work.
- Dr. Philipp Rinklin who mentored my research, kept the lab running smoothly and cared for everyone. Our detailed conversations on linguistics were a signature of shared meals. 01100100 01100001 01101110 01101011 01100101.
- The *Night Shift.* I feel tremendously lucky to have worked with my friends. Dr. Leroy Grob for being a cheerful ol' chap, always ready to lend an ear and a hand. Lennart Weiß, weil er ein gutmütiger, harter Kerl ist, der immer genau das sagt, was er denkt. Alla mia carissima Fulvia, amica e confidente, per il suo sostegno e la sua collaborazione, per le nostre discussioni e per avermi tollerato come collega d'ufficio. Lukas Hiendlmeier für seine Direktheit, seine Ehrlichkeit und seinen an sich guten Willen und seinen Wunsch, Menschen wirklich zu helfen und Dinge zum Laufen zu bringen. Meine Ehre, mit dir zusammengearbeitet zu haben. Good old George Al Boustani, the prankmaster. Thank you for

those BBQs, coffees and for your permanent good mood. Inola Kopic für ihre Freundlichkeit und Hilfe und besonders für ihre ständige Fröhlichkeit. Marta Nikić za iskrenost, lukavost i realan pogled na život. Beatrice De Chiara per il suo carattere rilassato e la sua affidabilità. Infine, ma non meno importante, Giorgio per il suo buon umore e per aver reso le nostre serate più piacevoli.

- Heike Url for her heartwarming friendliness and will to help others. One could always find a helping hand in her.
- Anja Kenn and Elisabeth Haider for combating the bureaucracy and dealing with all that paperwork for us to be able to do research.
- Dr. Tetsuhiko Teshima for his kind guidance, support and his enthusiasm for our projects.
- The group of Neuroelectronics for a great time together.
- My former supervisors and colleagues, Sabine Zips and Korkut Terkan for all their help and support.
- Dr. Michael Gebhardt and Prof. Dr. Harald Luksch for introducing me to the locust. None of this would have been possible without your kind guidance and support.
- Amelie Erben and Tanja Groll for our kind, diligent and successful collaborations.
- Dr. Madleen Busse for kindly letting me use her lab during my early steps.
- The MIBE people, specially Josef Hintermair and Susanne Schnell-Witteczek.

- The Gleich and Hemmert groups. To Jonathan, Bojan, Albert and Andrej, for the beers, karaoke and companionship, and for having me in the electronics lab.
- The ZEITLab people, especially Prof. Dr. Markus Becherer, Dr. Michael Haider, Rainer Emling and Anika Kwiatkowski, for the nice teamwork at the “new building”.
- All my students for what they taught me.
- Sebastian Freko for designing, building and characterizing the pre-folded electrodes presented in Chapter 5.
- My Argentinian friends: Lucas, Macarena, Fernando, Pablo and Juan.
- Luz for her assistance with histology.
- Philipp, Fernando, Pablo, Lukas, Lennart and Sebastian who provided critical feedback for this manuscript.
- Last but not least, my family, for always supporting me in every possible way. Gracias.